THE UNIVERSITY *of* EDINBURGH

This thesis has been submitted in fulfilment of the requirements for a postgraduate degree (e.g. PhD, MPhil, DClinPsychol) at the University of Edinburgh. Please note the following terms and conditions of use:

This work is protected by copyright and other intellectual property rights, which are retained by the thesis author, unless otherwise stated.
A copy can be downloaded for personal non-commercial research or study, without prior permission or charge.
This thesis cannot be reproduced or quoted extensively from without first obtaining permission in writing from the author.
The content must not be changed in any way or sold commercially in any format or medium without the formal permission of the author.
When referring to this work, full bibliographic details including the author, title, awarding institution and date of the thesis must be given.

Energy-momentum tensor from Wilson flow in lattice ϕ^4-theory

Susanne Ehret

Doctor of Philosophy
The University of Edinburgh
August 2017

Abstract

The energy-momentum tensor (EMT) is the Noether current associated with translations. It is of interest because, first of all, it has physical meaning as it contains the energy density and the momentum density. Moreover, its trace can be related to the beta function so that the scaling behaviour of the theory at hand can be studied. We are particularly interested in the scaling behaviour of strongly coupled theories. To explore the strong coupling regime it is necessary to compute the EMT non-perturbatively, i.e. on the lattice. This complicates matters greatly. On the lattice translation invariance is broken which leads to additional terms in the translation Ward identity from which the EMT is derived. This results in turn in the need to renormalise the EMT on the lattice.

In this thesis we extend recent studies on the renormalisation of the EMT in four-dimensional gauge theory to the case of a three-dimensional scalar theory to investigate its divergence structure and the numerical feasibility of the suggested procedure on a more basic level. Furthermore, scalar ϕ^4-theory in three dimensions exhibits an infrared fixed point and can thus serve as a toy model to examine mechanisms for building theories beyond the standard model.

Our strategy to renormalise the EMT on the lattice is to identify all possible terms that can mix with both sides of the translation Ward identity. The renormalised EMT is a combination of operators of the same or lower dimension obeying the symmetries of the theory. The mixing is determined by requiring that the renormalised EMT satisfies the correct Ward identities. Using different probes in the translation Ward identity one can compute the coefficients of the EMT by solving a linear system of equations. However, contact terms can arise. One solution is the recently introduced Wilson flow. Its renormalisation properties allow for expectation values free of contact terms. That way the Wilson flow

provides for a meaningful theoretical formulation of the EMT on the lattice that can be used in practice.

In this thesis we review the renormalisation properties and the phase diagram of scalar ϕ^4-theory in three dimensions, the translation Ward identity and the EMT in the continuum, as well as the gradient flow for scalar theory. A large part is dedicated to the perturbative renormalisation of the EMT on the lattice. Finally, our strategy to compute the renormalisation constants of the EMT in scalar theory non-perturbatively is discussed in detail, and our results for the renormalisation constants are presented.

Lay summary

Most phenomena we observe in the world we live in are well-described by the standard model, a mathematical theory explaining the microscopic building blocks of our universe and the forces acting between them. The building blocks are quarks and leptons, the forces are the electromagnetic, the weak and the strong interaction transmitted through gauge bosons. The strong interaction acts between the quarks composing e.g. proton and neutron. It is counterintuitive in its effect as the force becomes stronger with increasing distance between the particles. This peculiar behaviour is also manifest in the mathematical description of the strong force requiring new mathematical concepts. The prevalent method used to date are lattice computations: space and time are being viewed as discrete instead of continuous enabling us to use computer power to perform calculations.

There are yet many observations that cannot be explained by the standard model, e.g. gravity. Thus, physicists are looking for extensions of the existing model, or an alternative. We are particularly interested in refining the knowledge of the strong interaction and within this sector a construct called the energy-momentum tensor. The energy-momentum tensor is a measurable quantity in the sense that it contains information about the energy and the momentum of a particle. It is also interesting because it appears in equations describing the behaviour of a theory at different length scales.

In this thesis we are not considering the strong force but a much simpler mathematical model which is called scalar ϕ^4-theory in three dimensions. The reason is twofold. Firstly, scalar ϕ^4-theory is clear in terms of analytic calculations, and the computational cost is very small so that results can be achieved in a short amount of time. Secondly, scalar ϕ^4-theory in three dimensions exhibits one desired property, a so-called infrared fixed point. In this way scalar

ϕ^4-theory serves as a toy model for theories beyond the standard model that possess such a fixed point themselves.

As we are ultimately interested in theories related to the strong force we place our scalar ϕ^4-theory on the lattice. The calculation of the energy-momentum tensor on the lattice needs some special care. Due to the discretisation of space and time the symmetry of translations is broken as infinitesimal shifts of particles become impossible. This leads to infinities that have to be dealt with through a concept called renormalisation. Renormalising the energy-momentum tensor means redefining it such that the infinities disappear. Some of the difficulties can be cured with the so-called Wilson flow acting like a fluid filling the gaps between the lattice sites.

To summarise, we test a numerical method to compute the energy-momentum tensor in a simplified model with the goal to apply it later to strongly coupled theories beyond the standard model.

Declaration

I declare that this thesis was composed by myself, that the work contained herein is my own except where explicitly stated otherwise in the text, and that this work has not been submitted for any other degree or professional qualification except as specified.

Parts of this work have been published in [1, 2].

(*Susanne Ehret, August 2017*)

Acknowledgements

First and foremost I would like to express my sincere gratitude to my supervisor Luigi Del Debbio for his indispensable advice, his patient guidance, and his support in every stage of my PhD, including polishing this thesis.

My thanks go further to all other people in our collaboration, Antonio Rago, Antonin Portelli, Roberto Pellegrini and Francesco Capponi, as well as to Agostino Patella for the great many fruitful discussions.

I am indebted to Oliver Witzel for his ever-open door and for having a seemingly endless amount of time to debate all sorts of problems. Thanks a million!

I am also grateful to James Cockburn, Ava Khamseh, Joscha Reichel, and Andries Waelkens for proofreading this thesis. Thank you!

I would like to thank everyone in the particle physics theory group, especially Einan Gardi for the most useful lecture notes on modern quantum field theory, and Eliana Lambrou, Ava Khamseh, Andries Waelkens and Joscha Reichel for being such wonderful friends during the stressful four years.

Lastly, this thesis would not have been possible without the love and support of my entire family. Thank you for everything!

Contents

List of figures

List of tables

List of acronyms

EMT	Energy-momentum tensor
GFP	Gaussian fixed point
LSE	Linear system of equations
TWI	Translation Ward identity
WFFP	Wilson-Fischer fixed point

1

Introduction

The physical phenomena of the world we live in are well explained by the standard model. It is a well-established, self-consistent theory that gives a reliable description of the nature and interactions of elementary particles. However, it does not incorporate all observations, e.g. it fails to include gravity. This evokes the need to look for extensions of the standard model, or a replacement. The mathematical tool of choice for describing either the standard model, or a theory beyond the standard model is often quantum field theory.

Quantum field theories are a widely studied subject as they provide the toolkit to describe physics on the quantum level [3, 4]. Interacting theories are not solvable analytically. A common tool to extract properties and physically meaningful, measurable quantities is perturbation theory. While Abelian field theories like quantum electrodynamics are well understood and successfully applied, e.g. the theoretical and experimental values of the fine-structure constant agree to eight significant figures, non-Abelian field theories exhibit difficulties in the analytic treatment of the unavoidable non-perturbative regime. Quantum chromodynamics (QCD) is the non-Abelian gauge theory that is associated with the strong force and describes the interaction between quarks and gluons [5]. The coupling between the strongly interacting components is usually not small so that perturbation theory is only applicable for a restricted regime, that is for high energies and short distances. For low energies and large distances the theory cannot be studied by perturbative methods as the value of the coupling

increases with increasing distance. This property is called asymptotic freedom [6–8]. The solution is the formulation of QCD on a four-dimensional space-time lattice introduced by K. G. Wilson [9]. The discretisation provides the possibility to examine non-Abelian field theories for large coupling constants by numerical simulations, see e.g. [10, 11]. Measurements made through lattice calculations allow for precise predictions proving to coincide with experimental results [12].

A new approach to the methods used to date is the gradient flow which is referred to as Wilson flow on the lattice. It was recently proposed in [13–17]. The idea is to introduce an extra dimension, the flow time, along which the original field is evolved according to a flow equation. One can then formulate the theory in $d+1$ dimensions. The renormalisation of the evolved fields is in many cases very simple. They either do not need to be renormalised at all, or they renormalise multiplicatively, depending on the theory at hand. Observables containing fields at positive flow time are non-local in the elementary fields which accommodates many advantages, such as the absence of contact terms in correlation functions. Moreover, quantum fluctuations are damped, and more data can be generated by varying the value of the flow time. Considering the theory on the lattice provides measurements of high precision and a tool to investigate the symmetries of non-Abelian gauge theories at all length scales.

We are interested in studying the energy-momentum tensor (EMT) because first and foremost as an observable it has physical meaning. Its entries are the energy density and the momentum density. Furthermore, the scaling behaviour of a theory can be studied by examining the trace of the EMT as it relates to the beta function, and it enters in the dilatation Ward identity [18]. The EMT in the classical sense is the conserved Noether current associated with translation symmetry. On the quantum level it is the generator of translations. The conservation of the EMT is secured by the translation Ward identity (TWI). The latter ensures that the derivative of the EMT is finite. However, the finiteness of the EMT itself is not guaranteed by the TWI. It can be shown that it is possible to construct a new, finite EMT that is still the generator of translations and satisfies the TWI [19].

We are in particular interested in the scaling behaviour of strongly coupled theories which amounts to placing the theory on the lattice. This complicates matters greatly. The discretisation of space and time breaks translation symmetry

thereby generating additional terms in the TWI. This in turn leads to the need to renormalise the formerly finite EMT. The difficulty lies in finding a renormalisation prescription that allows the recovery of translation symmetry in the continuum limit. We have to construct the EMT on the lattice such that it is conserved and serves as the generator of translations in the continuum limit, so that the continuum TWI is satisfied. In order to renormalise the EMT one needs to find all operators that can mix with the EMT of the same or lower dimension that have the same transformation properties as the bare EMT under the symmetries of the theory. It is then possible to extract the coefficients by imposing the TWI and solving a linear system of equations composed of the TWI for different probes. This programme was suggested in [20, 21]. The drawback is the appearance of contact terms making numerical computations more challenging.

The problem can be overcome by using the aforementioned Wilson flow. Correlation functions including operators at positive flow time do not produce contact terms. Thus, contact terms are absent in the TWI even for a probe sitting at the same position as the EMT and the Wilson flow facilitates a meaningful theoretical formulation of the EMT on the lattice that can be put into practice.

Our programme to determine the coefficients of the terms in the renormalised EMT is the following:

1. Find the renormalised EMT by identifying all terms that can mix with the EMT given the symmetries and dimensions of the theory.

2. Choose different probes at positive flow time to insert into the renormalised TWI on the lattice.

3. Compute the coefficients by solving a linear system of equations.

This programme has been carried out for pure gauge theory in [22]. The goal is to apply it to strongly coupled theories beyond the standard model that have an infrared fixed point, see e.g. [23]. There are two alternatives to the above strategy. The first one is the small flow time expansion suggested in [24–26]. The second one proposes the use of shifted boundary conditions [27]. The effectiveness of each method can only be assessed by empirical studies.

In this thesis scalar ϕ^4-theory in three dimensions is studied in order to understand all aspects of the first method, described above, and to gain results in a comparably short amount of time. The analysis of scalar ϕ^4-theory is complementing recent studies on the renormalisation of the EMT, see [22, 28]. Scalar ϕ^4-theory serves as a toy model to examine general properties of the method combining numerical lattice computations and the Wilson flow, and to solve potential difficulties in a model that is less complex in analytic and cheap in computational terms. E.g. we show that in scalar ϕ^4-theory the fields evolved along the flow time do not need to be renormalised. A similar argument can be applied to composite operators made of fields at positive flow time only which greatly simplifies the renormalisation of the TWI. We choose space-time dimension three as scalar ϕ^4-theory exhibits an infrared fixed point in three dimensions giving us the possibility to transfer the insights we gain during the analysis to theories beyond the standard model that possess such a fixed point. Ultimately, we want to be able to identify and characterise fixed points for four-dimensional theories that can serve as the foundation to build models of physics beyond the standard model. As scalar ϕ^4-theory in three dimensions is asymptotically free its analysis delivers insight into analytic and computational methods applicable to asymptotic free theories in particular.

We begin the second chapter with a brief recapitulation of scalar ϕ^4-theory, focussing on the renormalisation group properties of the theory in three dimensions, including the phase diagram and the infrared fixed point. The TWI and the EMT in the continuum are derived. In chapter three we introduce the gradient flow for scalar ϕ^4-theory and discuss its renormalisation properties as well as the TWI with probes at positive flow time. We then turn towards the lattice. The fourth chapter contains a detailed description of scalar ϕ^4-theory on the lattice. A general Ward identity on the lattice is derived and the renormalisation of the TWI and the energy-momentum tensor are discussed, with and without the Wilson flow. Chapter five is the most extensive one, explaining our simulation setup and our strategy to compute the coefficients numerically in great detail. Finally, we present our results.

2

Scalar field theory in the continuum

2.1 Scalar field in the continuum

We are interested in a three-dimensional scalar theory that is Lorentz invariant and even under the symmetries $\phi \to -\phi$ and $x \to -x$ so that we include only terms with even powers of derivatives and fields in the action. Let us first consider the more general case of a scalar field theory in d-dimensional Euclidean space-time where odd powers of the fields are allowed. We denote the scalar field with ϕ and allow in the action all terms of the form $\partial^m \phi^n$, with $m, n \in \mathbb{N}$. Knowing the kinetic term $\sum_\mu \partial_\mu \phi \partial_\mu \phi$ the dimensions of derivatives and fields are

$$[\partial_\mu] = 1, \qquad [\phi] = \frac{d-2}{2}. \tag{2.1}$$

We use square brackets to indicate the mass dimension. The classical dimension of a selected operator is

$$[\partial^m \phi^n] = m + n\,\frac{d-2}{2}. \tag{2.2}$$

Restricting ourselves to the case $m = 2$ the most general Lagrangian of such a scalar field theory reads

$$\mathcal{L} = \frac{1}{2}\sum_\mu \partial_\mu \phi \partial_\mu \phi + \frac{m^2}{2}\phi^2 + \sum_{n>2} \frac{g_n}{n!}\phi^n. \tag{2.3}$$

A detailed derivation of the Feynman rules following from the Lagrangian above can be found in app. B. There, the Feynman rules are derived on a d-dimensional space-time lattice. The derivation can readily be translated to the case of a scalar theory in the continuum. The momentum space Feynman rules in the continuum are listed in fig. 2.1. Throughout the thesis a tilde indicates a Fourier transform, and we omit the momentum-conserving delta function for better readability. The renormalised field theory will be discussed in great detail in chap. 4 on the lattice, which we forgo here for brevity.

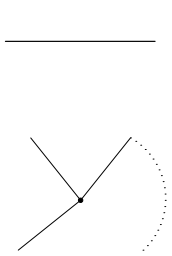

$$\tilde{D}(p^2) = \frac{1}{p^2 + m}$$

$$-g_n$$

Figure 2.1 *Feynman rules for scalar ϕ^n-theory in the continuum.*

Not all terms allowed by symmetry arguments enter the Lagrangian since we require our theory to be renormalisable. In order to decide which terms to keep we analyse the superficial degree of divergence and the renormalisation group flow.

2.2 Superficial degree of divergence

The superficial degree of divergence D of a Feynman diagram in scalar field theory described by the Lagrangian (2.3) is given by

$$D = dL - 2P, \tag{2.4}$$

where L is the number of loops and P the number of internal lines. This is easy to see from the loop integral as the power of loop-momenta in the numerator is d times L and the power of loop-momenta in the denominator is 2 times P. If $D \geq 0$ the diagram is superficially divergent.

A more useful expression can be found by noticing that the dimension of any diagram with a certain number of external legs E has to equal the dimension of the tree diagram with the same number of external legs,

$$[\text{diagram}] = dL - 2P + \sum_{n>2} V_n[g_n] \overset{!}{=} [g_E], \tag{2.5}$$

where V_n is the number of vertices of type ϕ^n. Thus,

$$D = [g_E] - \sum_{n>2} V_n[g_n]. \tag{2.6}$$

It is evident that for $[g_n] < 0$ the superficial degree of divergence increases with every added vertex. This renders the theory non-renormalisable. Requiring a non-negative dimension of all couplings leads to the equation

$$n \overset{!}{\leq} \frac{2d}{d-2}. \tag{2.7}$$

The theory is called renormalisable in the case of an equality and super-renormalisable if the inequality holds. Applied to the theory of interest in three dimensions with even powers of the field we have to demand $n \overset{!}{\leq} 6$ in order to work with a renormalisable theory. This means that we have to consider only two more terms besides the mass term. It is possible to restrict the number of allowed interaction terms even further by examining the renormalisation group flow.

2.3 Renormalisation group flow

This section follows [3] closely, where all arguments and intermediate results can be found in detail. In this reference the authors begin their demonstration with Wilson's approach to the renormalisation group [29]. We will restrict ourselves to a rather brief discussion focusing on the perturbative calculation as an elaborate treatment of the renormalisation group flow exceeds the scope of this thesis. We will however add the ϕ^6-term to the Lagrangian which is not included in [3]. We also impose from now on that the symmetries $\phi \to -\phi$ and $x \to -x$ hold.

We are mainly interested in the theory close to the free field fixed point, or Gaussian fixed point (GFP), that is for small couplings, because we have control over calculations by means of perturbation theory. Consider the generating functional

$$Z(J) = \int D\phi_\Lambda \, \exp\left\{ - \int d^d x \left(\frac{1}{2} \sum_\mu (\partial_\mu \phi)^2 + \frac{m^2}{2}\phi^2 + \frac{\lambda}{4!}\phi^4 + \frac{\eta}{6!}\phi^6 + J\phi \right) \right\}. \tag{2.8}$$

The subscript Λ is the ultraviolet cutoff indicating that $\tilde{\phi}(k) \neq 0$ only for momenta $|k| \leq \Lambda$. The concept of the generating functional is explained in app. B on the lattice. In order to see the influence of the quantum fluctuations at very large momenta, corresponding to very short distances, one can integrate out the high-momentum degrees of freedom. Let $b\Lambda \leq k \leq \Lambda$, where b is smaller but very close to one. We redefine $\phi \to \phi + \hat{\phi}$ so that

$$\tilde{\phi}(k) = \begin{cases} \tilde{\phi}(k) & \text{for } |k| \leq b\Lambda \\ 0 & \text{otherwise} \end{cases}, \qquad \tilde{\hat{\phi}}(k) = \begin{cases} \tilde{\phi}(k) & \text{for } b\Lambda \leq |k| \leq \Lambda \\ 0 & \text{otherwise} \end{cases}. \tag{2.9}$$

Rewriting the generating functional with the new fields yields

$$\begin{aligned} Z(J) = \int D\phi \, e^{-\int (\mathcal{L}(\phi) + J\phi)} \int D\hat{\phi} \, \exp\Bigg\{ - \int d^d x \Bigg(& \frac{1}{2} \sum_\mu (\partial_\mu \hat{\phi})^2 + \frac{m^2}{2}\hat{\phi}^2 \\ & + \lambda \left(\frac{1}{6}\phi^3\hat{\phi} + \frac{1}{4}\phi^2\hat{\phi}^2 + \frac{1}{6}\phi\hat{\phi}^3 + \frac{1}{4!}\hat{\phi}^4 \right) \\ & + \eta \left(\frac{1}{5!}\phi^5\hat{\phi} + \frac{1}{48}\phi^4\hat{\phi}^2 + \frac{1}{36}\phi^3\hat{\phi}^3 + \frac{1}{48}\phi^2\hat{\phi}^4 + \frac{1}{5!}\phi\hat{\phi}^5 + \frac{1}{6!}\hat{\phi}^6 \right) + \hat{J}\hat{\phi} \Bigg) \Bigg\}. \end{aligned} \tag{2.10}$$

Here, we added a hat on the source $\hat{J}$ corresponding to $\hat{\phi}$. Having two different fields we need to distinguish between the sources belonging to low and high-momentum modes since the perturbative treatment of the theory involves derivatives with respect to the sources to represent the fields, see again app. B. Note also that the $\phi\hat{\phi}$-term vanishes due to the definitions (2.9).

The Feynman rules for the generating functional (2.10) that appear additionally to the ones in fig. 2.1 can be found in fig. 2.2. We treat the mass term as perturbation as well because $m \ll b\Lambda$.

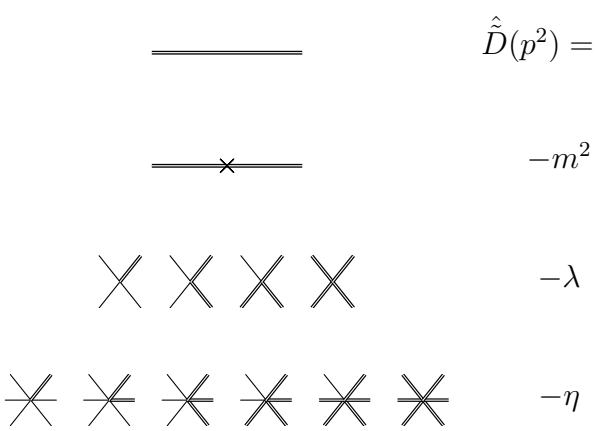

Figure 2.2 *Feynman rules for scalar ϕ^6-theory in the continuum that appear additionally when splitting the field in low and high-momentum modes. The single lines represent the low-momentum modes, the double lines represent the high-momentum modes which are integrated out.*

Integrating out the momentum shell $b\Lambda \leq k \leq \Lambda$ leads to a new generating functional with an effective Lagrangian $\mathcal{L}_{\text{eff}}$

$$Z(J) = \int D\phi_{b\Lambda}\, e^{-\int \mathcal{L}_{\text{eff}}} \tag{2.11}$$

with

$$\begin{aligned}\mathcal{L}_{\text{eff}} = \frac{1}{2}(1+\Delta Z)\sum_{\mu}(\partial_\mu\phi)^2 + \frac{1}{2}(m^2+\Delta m^2)\phi^2 + \frac{1}{4!}(\lambda+\Delta\lambda)\phi^4 \\ + \frac{1}{6!}(\eta+\Delta\eta)\phi^6 + \Delta A(\partial_\mu\phi)^4 + \Delta B\phi^8 + \dots\,,\end{aligned} \tag{2.12}$$

where $\Delta\cdot$ portrays corrections to the field and couplings as well as newly created terms. In general, all possible higher-dimensional operators that obey the chosen symmetries are generated. To compare the original with the effective Lagrangian we rescale momentum and position,

$$k' = {}^{k}/_{b}, \qquad x' = xb. \tag{2.13}$$

The effective Lagrangian expressed with the rescaled parameters reads

$$\mathcal{L}_{\text{eff}} = \frac{1}{2}\sum_{\mu}(\partial'_\mu\phi')^2 + \frac{m'^2}{2}\phi'^2 + \frac{\lambda'}{4!}\phi'^4 + \frac{\eta'}{6!}\phi'^6 + A'(\partial'_\mu\phi')^4 + B'\phi'^8 + \dots\,, \tag{2.14}$$

where

$$\phi' = \left(b^{2-d}(1+\Delta Z)\right)^{1/2}\phi. \tag{2.15}$$

The couplings transform as

$$\begin{aligned} m'^2 &= (m^2+\Delta m^2)(1+\Delta Z)^{-1}\, b^{-2} \\ \lambda' &= (\lambda+\Delta\lambda)(1+\Delta Z)^{-2}\, b^{d-4} \\ \eta' &= (\eta+\Delta\eta)(1+\Delta Z)^{-3}\, b^{2d-6} \\ A' &= (A+\Delta A)(1+\Delta Z)^{-2}\, b^{d} \\ B' &= (B+\Delta B)(1+\Delta Z)^{-4}\, b^{3d-8} \end{aligned} \tag{2.16}$$

In our case $A, B = 0$. However, we could have included these terms in the original Lagrangian so that the above equations apply in general. The set of equations (2.16) describes a transformation of the Lagrangian. Taking b infinitesimally close to one and iterating eqs. (2.16) we can generate a trajectory in the space of Lagrangians by integrating over the high-momentum degrees of freedom iteratively. This is referred to as the renormalisation group flow.

All perturbations of the couplings vanish at the GFP, where $m^2 = \lambda = \eta = A = B = ... = 0$. In its vicinity we can ignore all higher-order terms indicated by Δ which yields

$$\begin{aligned} m'^2 &= m^2\, b^{-2} \\ \lambda' &= \lambda\, b^{d-4} \\ \eta' &= \eta\, b^{2d-6} \\ A' &= A\, b^{d} \\ B' &= B\, b^{3d-8}. \end{aligned} \tag{2.17}$$

Since $b < 1$ those couplings that carry negative powers of b grow along the renormalisation group flow, and those that possess positive powers of b decrease when integrating out high-momentum modes. Increasing couplings carry the Lagrangian away from the GFP. The operators associated to growing and shrinking couplings are called relevant and irrelevant, respectively. Marginal operators are associated to couplings that are proportional to b^0. For these terms higher orders must be included to know if they are relevant or irrelevant.

A general transformation of a coefficient C' with m derivatives and n powers of the field is

$$C'_{m,n} = C\, b^{m+n(d/2-1)-d}, \tag{2.18}$$

where the summands in the exponent m and d derive from the transformation $x' = xb$ for derivatives and integral measure in the action, respectively. The term $n(d/2-1)$ comes from the field transformation (2.15). Note the connection between renormalisability and relevant, marginal and irrelevant operators. On the one hand, for an operator to be relevant or marginal the exponent of b has to be negative or zero,

$$m + n\left(\frac{d}{2} - 1\right) - d \leq 0. \tag{2.19}$$

On the other hand, we required the dimension of the couplings to be greater than or equal to zero in order to maintain a renormalisable theory. The dimension of the coupling is related to the dimension of the corresponding operator (2.2) via $d_{C'} = d - [\partial^m \phi^n]$. Setting this greater or equal zero leads to eq. (2.19). Hence, relevant and marginal operators correspond to super-renormalisable or renormalisable theories, respectively.

From the discussion above follows that relevant and marginal operators at the GFP have a mass dimension smaller than or equal to the space-time dimension of the theory under consideration. Tab. 2.1 classifies operators O which obey our symmetry requirements as relevant, marginal and irrelevant depending on their mass dimension and the dimension of space-time d.

O	$d > 4$	$d = 4$	$d = 3$	$d = 2$
ϕ^2	rel	rel	rel	rel
ϕ^4	irrel	marg	rel	rel
ϕ^6	irrel	irrel	marg	rel
ϕ^{2n}	irrel	irrel	irrel	rel
$\partial^2\phi^2$	marg	marg	marg	marg
$\partial^2\phi^{2n'}$	irrel	irrel	irrel	marg
$\partial^{2m}\phi^2$	irrel	irrel	irrel	irrel

Table 2.1 *Classification of operators O in the action as relevant (rel), marginal (marg) and irrelevant (irrel) according to their classical mass dimension and the dimension of space-time d with $n \geq 4$, $n', m \geq 2$.*

The table suggests that in $d > 2$ close to the GFP we only need to include the kinetic term plus a potential in the action. In particular, in $d = 3$ we need to find out if the ϕ^6-term is marginal relevant or marginal irrelevant. In order to do so we can calculate the first order correction to the ϕ^6-coupling explicitly. We will suppose that η is of order λ^2, and that the external momenta are small compared to the cutoff. The former assumption is justified because in this way the order in the couplings reflects the number of loops in a diagram. Replacing any four-point vertex associated to λ with a four-point vertex associated to η with two of the six legs being connected leads to an additional loop per replaced vertex. η being of one order higher than λ accounts for this increase in the number of loops. The latter assumption reduces the number of diagrams as some would violate momentum conservation, and simplifies the integrals. E.g. one can construct a tree-level diagram with six external legs from two four-point vertices with three single lines and one double line each, the double line connecting the two vertices. Small external momenta cannot produce the large momentum between the two vertices so that the diagram does not contribute to the following analysis. For completeness we will also compute the leading order correction to the mass and λ.

Let us start the discussion with the first order correction to the mass. The diagram contributing to order λ is created by the $\phi^2\hat{\phi}^2$-term in eq. (2.10),

$$
\begin{aligned}
&= -\frac{\lambda}{2}\int_k \frac{1}{k^2} \\
&= -\frac{\lambda}{(4\pi)^{d/2}\Gamma(\frac{d}{2})}\frac{1-b^{d-2}}{d-2}\Lambda^{d-2} \\
&\overset{d=3}{=} -\frac{\lambda}{4\pi^2}(1-b)\Lambda.
\end{aligned}
\tag{2.20}
$$

Here, we abbreviated the momentum integral, see eq. (A.1), and used the fact that the integrand of the volume integral is a function of the radius only, see eq. (A.2). Marking dimensionless parameters with an inverted hat it follows from eqs. (2.16) that

$$
\check{m}'^2 = \check{m}^2 b^{-2} + \frac{\check{\lambda}}{2\pi^2}(1-b)b^{-2} + \mathcal{O}(\check{\lambda}^2). \tag{2.21}
$$

Note that ΔZ is of order λ^2. The correction to the mass is positive since $1-b>0$. As $b^{-2}>1$ the mass grows when integrating out high-momentum degrees of freedom and ϕ^2 is a relevant operator, as expected.

The first order correction to λ has two contributions, one coming from combining two $\phi^2\hat{\phi}^2$-terms, and one from the term $\phi^4\hat{\phi}$ in eq. (2.10):

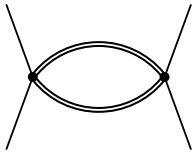

$$\begin{aligned} &= \frac{\lambda^2}{2}\int_k \left(\frac{1}{k^2}\right)^2 \\ &= \frac{\lambda^2}{(4\pi)^{d/2}\Gamma(\frac{d}{2})}\frac{1-b^{d-4}}{d-4}\Lambda^{d-4} \\ &\overset{d=3}{=} -\frac{\lambda^2}{4\pi^2}(1-b^{-1})\Lambda^{-1}, \end{aligned} \tag{2.22}$$

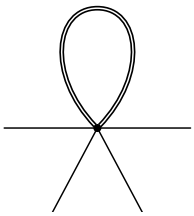

$$\begin{aligned} &= -\frac{\eta}{2}\int_k \frac{1}{k^2} \\ &= -\frac{\eta}{(4\pi)^{d/2}\Gamma(\frac{d}{2})}\frac{1-b^{d-2}}{d-2}\Lambda^{d-2} \\ &\overset{d=3}{=} -\frac{\eta}{4\pi^2}(1-b)\Lambda. \end{aligned} \tag{2.23}$$

Using eqs. (2.16) we find

$$\check{\lambda}' = \check{\lambda}b^{-1} + \frac{6\check{\lambda}^2}{\pi^2}(1-b^{-1})b^{-1} + \frac{6\eta}{\pi^2}(1-b)b^{-1}. \tag{2.24}$$

Note that η is already dimensionless. The first and third term grow. However, the second term is a negative correction since $1-b^{-1}<0$. From eqs. (2.17) we know that λ is relevant in three dimensions. Close to the GFP where λ is small, the leading term outweighs the correction term. When moving away from this fixed point the second order term becomes increasingly important with growing λ until the two terms cancel exactly. At this point exists a second fixed point of the renormalisation group flow: the Wilson-Fischer fixed point (WFFP) [30].

The final correction we have to examine is the one for η. There are again two diagrams emerging from eq. (2.10) that contribute to the first order correction. The first one comes from three $\phi^2\hat{\phi}^2$-terms, the second one from combining the vertices belonging to the terms $\phi^2\hat{\phi}^2$ and $\phi^4\hat{\phi}^2$:

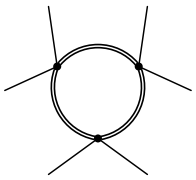

$$\begin{aligned} &= -\lambda^3 \int_k \left(\frac{1}{k^2}\right)^3 \\ &= -\frac{2\lambda^3}{(4\pi)^{d/2}\Gamma(\frac{d}{2})}\frac{1-b^{d-6}}{d-6}\Lambda^{d-6} \\ &\overset{d=3}{=} \frac{\lambda^3}{6\pi^2}(1-b^{-3})\Lambda^{-3}, \end{aligned} \tag{2.25}$$

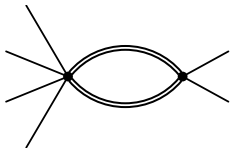

$$\begin{aligned} &= \frac{\lambda\eta}{2} \int_k \left(\frac{1}{k^2}\right)^2 \\ &= \frac{\lambda\eta}{(4\pi)^{d/2}\Gamma(\frac{d}{2})}\frac{1-b^{d-4}}{d-4}\Lambda^{d-4} \\ &\overset{d=3}{=} -\frac{\lambda\eta}{4\pi^2}(1-b^{-1})\Lambda^{-1}. \end{aligned} \tag{2.26}$$

From eqs. (2.16) follows

$$\eta' = \eta - \frac{5!\check{\lambda}^3}{\pi^2}(1-b^{-3}) + \frac{6!\check{\lambda}\eta}{4\pi^2}(1-b^{-1}). \tag{2.27}$$

The first term is constant. The second term is greater than zero but its absolute value is smaller than the absolute value of the negative third term since $5! < {}^{6!}/_{4}$ and $1-b^{-3} < 1-b^{-1} < 0$. Thus, the third term dominates and the operator corresponding to the coupling η is marginal irrelevant.

From the perturbative discussion above follows that the Lagrangian of ϕ^n-theory, with n even and close to the GFP reads in three dimensions

$$\mathcal{L} = \frac{1}{2}\sum_\mu \partial_\mu\phi\partial_\mu\phi + \frac{m^2}{2}\phi^2 + \frac{\lambda}{4!}\phi^4. \tag{2.28}$$

The theory is super-renormalisable. There are only two divergent diagrams, both with two external legs and one and two vertices, respectively, see fig. 2.3. The diagrams are linearly and logarithmically divergent.

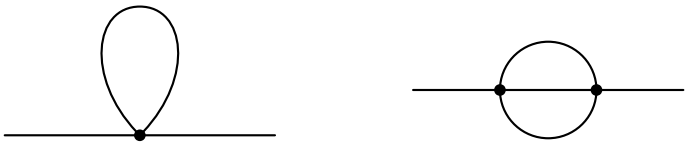

Figure 2.3 *The only two divergent diagrams in scalar ϕ^3-theory in three dimensions.*

The infinite coupling space of ϕ^4-theory in three dimensions is sketched in fig. 2.4. There are two relevant couplings at the GFP, m and λ. The direction κ represents all other, irrelevant, couplings. The GFP and the WFFP lie on the critical surface where the renormalised mass is zero. The red line is the line of constant physics that connects the two fixed points and is also on the critical surface. The direction of the renormalisation group flow is indicated as well. λ is irrelevant close to the WFFP which is the very reason why this fixed point is created in the first place. However, the operator corresponding to the mass is always relevant since the renormalised mass increases from zero to being greater than zero even when moving only infinitesimally away from any fixed point.

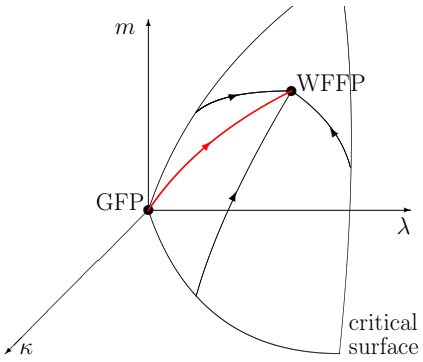

Figure 2.4 *Sketch of the infinite coupling space of ϕ^4-theory in three dimensions showing the critical surface where the renormalised mass is zero, as well as the GFP and WFFP.*

The (m,λ)-plane of the renormalisation group flow diagram corresponds to the phase diagram. ϕ^4-theory has two phases depending on the value of the squared bare mass. If $m^2 > 0$ the potential has one minimum at $\phi = 0$. However, if $m^2 < 0$ the potential has two minima at $\phi_{1,2} = \pm\sqrt{\frac{-6m^2}{\lambda}}$. Both situations are displayed in fig. 2.5.

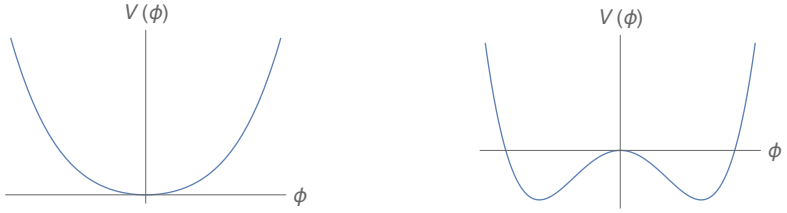

Figure 2.5 *The potential of ϕ^4-theory. On the left the symmetric phase in the bare theory where $m^2 \geq 0$, on the right the broken phase where $m^2 < 0$.*

Studying the mass renormalisation perturbatively we find

$$m_R^2 = m^2 + \frac{\lambda_R}{2a} Z_0. \tag{2.29}$$

The calculation will be presented on the lattice, see chap. 4, eq. (4.14). λ_R is the renormalised coupling, a is the lattice spacing, and Z_0 is specified in eq. (4.13). From eq. (2.29) follows that for a critical line where $m_R = 0$ to exist, m^2 has to be negative. The phase diagram is sketched in fig. 2.6. The critical line lies in the quadrant where $m^2 < 0$, $\lambda > 0$. λ has to be greater than zero so that the potential is bounded from below. The critical line corresponds to the intersection of the critical surface with the (m,λ)-plane in fig. 2.4. It separates the symmetric from the broken phase. The GFP is again located where $m = \lambda = 0$.

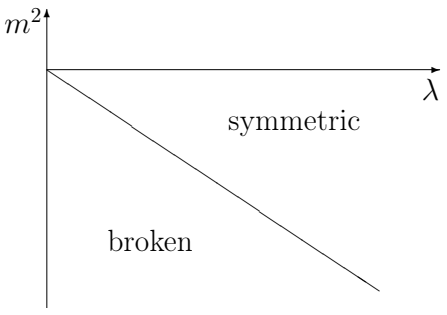

Figure 2.6 *Sketch of the phase diagram of ϕ^4-theory.*

Scalar ϕ^4-theory in three dimensions is a good toy model to study infrared fixed points in other theories, including theories beyond the Standard Model, see e.g. [31]. Wilson and Fischer showed in [30] that scalar ϕ^4-theory in three dimensions exhibits an infrared fixed point, the WFFP. It lies in the infrared as it emerges after having integrated out the high-momentum modes. Scalar theory is easy to study numerically and is computationally very cheap. It has thus the advantage of having a theory at hand where hypotheses and computational methods can be tested to a high level of accuracy in relatively little time.

2.4 Energy-momentum tensor in the continuum

The energy-momentum tensor (EMT) can be defined from the invariance of the theory under global translations. For a local translation in direction $\hat{\rho}$, $x_\mu \to x'_\mu = x_\mu + \delta_{\mu\rho}\alpha(x)$, the variation of the scalar field is

$$\delta_\rho \phi(x) = \alpha(x)\, \partial_\rho \phi. \tag{2.30}$$

The EMT appears in the corresponding variation of the action,

$$\delta_\rho S = \int d^d x \, \sum_\mu T_{\mu\rho}(x) \partial_\mu \alpha(x). \tag{2.31}$$

It is clear from eq. (2.31) that the columns of the EMT, $T_{\mu\rho}$, are the Noether currents J_μ associated to translations,

$$J_\mu^{(\rho)}(x) = T_{\mu\rho}(x). \tag{2.32}$$

For the scalar theory the EMT is given by

$$T_{\mu\rho} = \partial_\mu \phi \partial_\rho \phi - \delta_{\mu\rho} \left(\frac{1}{2} \sum_\sigma \partial_\sigma \phi \partial_\sigma \phi + \frac{m^2}{2} \phi^2 + \frac{\lambda}{4!} \phi^4 \right). \tag{2.33}$$

The corresponding integrated translation Ward identity (TWI) for a generic probe $\mathcal{P}$ that depends on the field and derivatives of the field reads

$$\langle \delta_\rho S \, \mathcal{P} \rangle = \langle \delta_\rho \mathcal{P} \rangle, \tag{2.34}$$

where the variation of the action $\delta_\rho S$ is given in eq. (2.31). $\delta_\rho \mathcal{P}$ is the variation of the probe $\mathcal{P}$ under a translation in direction $\hat{\rho}$ and can be written as

$$\delta_\rho \mathcal{P} = \int d^d x \; \alpha(x) \; \delta_{x,\rho} \mathcal{P}, \tag{2.35}$$

where we defined the local variation

$$\delta_{x,\rho} \mathcal{P} = \frac{\partial \mathcal{P}}{\partial \phi(x)} \partial_\rho \phi(x) + \sum_\tau \frac{\partial \mathcal{P}}{\partial(\partial_\tau \phi(x))} \frac{1}{\alpha(x)} \partial_\tau (\alpha(x) \partial_\rho \phi(x)) + \dots \, . \tag{2.36}$$

Using the notation introduced above the local TWI reads

$$\sum_\mu \partial_\mu \langle T_{\mu\rho}(x) \; \mathcal{P} \rangle = - \langle \delta_{x,\rho} \mathcal{P} \rangle. \tag{2.37}$$

A more familiar form of the TWI is recovered when choosing $\mathcal{P}$ to be a monomial in the field ϕ,

$$\sum_\mu \partial_\mu \langle T_{\mu\rho}(x) \; \phi_1(x_1) \dots \phi_k(x_k) \rangle = - \sum_j \delta(x - x_j) \frac{\partial}{\partial (x_j)_\rho} \langle \phi_1(x_1) \dots \phi_k(x_k) \rangle. \tag{2.38}$$

A detailed derivation of a general Ward identity, the TWI and the EMT can be found in app. A.2.

The Ward identities, eqs. (2.37) and (2.38), show that the insertion of $\partial_\mu T_{\mu\rho}$ into correlation functions does not introduce new divergencies since the right-hand sides of these equations only involve finite correlators once the theory has been renormalised, up to contact terms. As a consequence any divergences in $T_{\mu\rho}$ must be proportional to operators that vanish when acted upon with a total derivative. Given the symmetries of the theory the only such term is proportional to

$$\left(\partial_\mu \partial_\rho - \delta_{\mu\rho} \sum_\sigma \partial_\sigma^2 \right) \phi^2. \tag{2.39}$$

This can be seen by observing that one can always add a total derivative to the EMT as the EMT is not an observable itself but its space integral is. Defining the modified EMT as

$$T'_{\mu\rho} = T_{\mu\rho} + \sum_\rho \partial_\rho O_{\rho\mu\nu} \tag{2.40}$$

and requiring for $O_{\rho\mu\nu}$ to be of dimension two, symmetric under $\phi \to -\phi$, and antisymmetric under $x \to -x$ we find

$$O_{\rho\mu\nu} = c_1\delta_{\rho\mu}\phi\partial_\nu\phi + c_2\delta_{\rho\nu}\phi\partial_\mu\phi + c_3\delta_{\mu\nu}\phi\partial_\rho\phi, \tag{2.41}$$

$$\sum_\rho \partial_\rho O_{\rho\mu\nu} = (c_1+c_2)(\partial_\mu\phi\partial_\nu\phi + \phi\partial_\mu\partial_\nu\phi) + c_3\delta_{\mu\nu}\sum_\rho(\partial_\rho\phi\partial_\rho\phi + \phi\partial_\rho^2\phi). \tag{2.42}$$

The derivative of $T'_{\mu\rho}$ leads to

$$\sum_{\mu,\rho}\partial_\mu\partial_\rho O_{\rho\mu\nu} = (c_1+c_2+c_3)\sum_\mu(\partial_\nu\phi\partial_\mu^2\phi + 2\partial_\mu\phi\partial_\mu\partial_\nu\phi + \phi\partial_\mu^2\partial_\nu\phi) \overset{!}{=} 0, \tag{2.43}$$

demanding that the sum of the coefficients c_i is zero. Using this result in the expression for $\sum_\rho \partial_\rho O_{\rho\mu\nu}$ gives (2.39).

It is easy to see that the term (2.39) is the only divergence one can append to the EMT in any dimension as terms in $O_{\rho\mu\nu}$ can only consist of one derivative and two fields. Adding more derivatives or fields exceeds the allowed dimension of $d-1$. An exception is the case $d = 2$ since the fields are dimensionless so that any number of fields can be added to terms in $O_{\rho\mu\nu}$.

It has been proven in [19] that adding the term (2.39) to the EMT results in correlation functions which include the EMT to be finite in four dimensions. However, $T_{\mu\rho}$ in the form (2.33) is already finite in three dimensions so that adding a term proportional to (2.39) is unnecessary. In fact, it turns out that it is convergent, see app. A.3.

The finiteness of the EMT in three dimensions can be seen by studying the possible divergences of the EMT perturbatively. Divergencies can only appear in the diagrams shown in fig. 2.7. The insertion of an operator $\propto \phi^2$ splits a propagator into two, thus causing two additional powers of the loop momentum in the denominator of a loop integral, making it less divergent. Only operators containing derivatives do not change the degree of divergence as they also add two powers of the loop momentum in the numerator. Inserting the operator $\propto \phi^4$ at a vertex does not change the degree of divergence of a diagram as well. Hence, since the theory is super-renormalisable divergencies can only be generated when inserting the EMT in the diagrams in fig. 2.3.

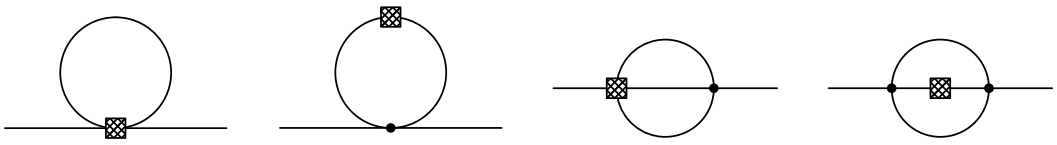

Figure 2.7 *The only possibly divergent diagrams that contain the EMT. The insertion of the appropriate terms in the EMT is marked by a hatched square.*

The perturbative calculation at one-loop order is reported in app. A.3. It is evident that the first diagram in fig. 2.7 corresponding to the insertion of the ϕ^4-term in the EMT is canceled by the mass renormalisation. For the loop integral in the second diagram we find for the insertion of the two terms in the EMT containing derivatives in d dimensions

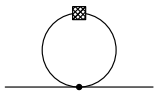

$$
\begin{aligned}
&= -\frac{\lambda}{2}\int_k \frac{k_\mu(k+q)_\rho + k_\rho(k+q)_\mu - \delta_{\mu\rho}\sum_\sigma k_\sigma(k+q)_\sigma}{(k^2+m^2)((k+q)^2+m^2)} \\
&= -\lambda\int_0^1 dx \int_l \left(\frac{\delta_{\mu\rho}(\frac{1}{d}-\frac{1}{2})l^2}{(l^2+M^2)^2} + \frac{x(x-1)(q_\mu q_\rho - \frac{1}{2}\delta_{\mu\rho}q^2)}{(l^2+M^2)^2} \right),
\end{aligned}
\tag{2.44}
$$

where we used Feynman parametrisation (A.3), changed variables, $l = k + xq$, and defined $M^2 = m^2 + x(1-x)q^2$. We see by power counting that the first term is divergent in $d \geq 2$. The second term is only divergent in $d \geq 4$. We conclude that any divergence in three dimensions is proportional to the operator ϕ^2 as external momenta appear only in the finite second term. However, this operator does not vanish when acting on it with a total derivative. Thus, there cannot be a divergence $\propto \phi^2$ and the EMT at one loop has to be finite. In four dimensions it can be shown that the divergencies in both terms combine such that they can be canceled by the term (2.39).

Instead of Feynman parametrisation we can study the Taylor series for small external momenta. This leads to the same conclusion at one loop, and at two-loop order as well, see app. A.4. Any potential divergence in the EMT is proportional to the operator ϕ^2 which cannot be as the derivative of the EMT has to be finite. Hence, the EMT itself is finite in three dimensions.

A similar calculation as the above one can be found in sec. 4.3 on the lattice but with a different outcome. In the case where the symmetry is broken, either explicitly or spontaneously, the variation of the action, eq. (2.31), receives extra contributions. In chap. 4 we study explicit symmetry breaking through lattice regularisation perturbatively which results in the necessity to renormalise the EMT. Chap. 5 will provide a non-perturbative solution to the renormalisation of the EMT on the lattice.

2.4.1 Continuum energy-momentum tensor conservation at one loop

Although the conservation of the derivative of the EMT in the continuum is evident non-perturbatively, it is instructive to understand the perturbative expansion. One TWI for local translations is given by choosing the product of two fields as probe,

$$\begin{aligned}\sum_{\mu} \partial_{\mu,x} \langle T_{\mu\rho}(x)\phi(x_1)\phi(x_2)\rangle = &-\delta(x-x_1)\partial_{\rho,x_1}\langle\phi(x_1)\phi(x_2)\rangle \\ &- \delta(x-x_2)\partial_{\rho,x_2}\langle\phi(x_1)\phi(x_2)\rangle,\end{aligned} \tag{2.45}$$

where the EMT is specified in eq. (2.33). We define the momentum space correlation function

$$\Omega_{\mu\rho}(p,q) = \langle \tilde{T}_{\mu\rho}(q)\tilde{\phi}(p)\tilde{\phi}(-(p+q))\rangle, \tag{2.46}$$

where all momenta are ingoing. The momentum space TWI is given by

$$\sum_{\mu} q_\mu \Omega_{\mu\rho}(p,q) = \tilde{D}(p^2)p_\rho - \tilde{D}((p+q)^2)(p+q)_\rho, \tag{2.47}$$

where $\tilde{D}(p^2)$ is the full, bare scalar propagator. We define the amputated matrix element $M_{\mu\rho}(p,q)$ as

$$M_{\mu\rho}(p,q) = \Omega_{\mu\rho}(p,q)\tilde{D}(p^2)^{-1}\tilde{D}((p+q)^2)^{-1}. \tag{2.48}$$

Using eq. (2.47) one finds

$$\sum_\mu q_\mu M_{\mu\rho}(p,q) = \tilde{D}((p+q)^2)^{-1} p_\rho - \tilde{D}(p^2)^{-1}(p+q)_\rho. \tag{2.49}$$

Let us now check the TWI in eq. (2.47) explicitly in perturbation theory. Starting with the tree level, i.e. the free theory, the EMT in the free theory resembles eq. (2.33) without the λ-term, and we note the free scalar propagator $\tilde{D}^{(0)}(p^2) = (p^2+m^2)^{-1}$, see fig. 2.1. The tree-level amputated matrix element $M^{(0)}_{\mu\rho}(p,q)$ is

$$M^{(0)}_{\mu\rho}(p,q) = p_\mu (p+q)_\rho + (p+q)_\mu p_\rho - \delta_{\mu\rho}\left(\sum_\sigma p_\sigma (p+q)_\sigma + m^2\right), \tag{2.50}$$

see eq. (A.37) for the momentum terms. Contraction with the transfer momentum q_μ yields after some massaging the right-hand side of the tree-level TWI,

$$\sum_\mu q_\mu M^{(0)}_{\mu\rho}(p,q) = \tilde{D}^{(0)}((p+q)^2)^{-1} p_\rho - \tilde{D}^{(0)}(p^2)^{-1}(p+q)_\rho, \tag{2.51}$$

which can be displayed diagrammatically by adding the external legs again,

$\sum_\mu q_\mu$ 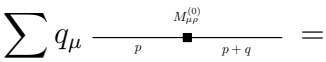

$=$ 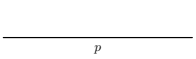

$p_\rho \; -$ 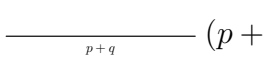

$(p+q)_\rho,$ (2.52)

where we denote the insertion of the tree-level EMT by a filled square with two legs.

In order to obtain the one-loop TWI one could evaluate the TWI term by term. However, it is much clearer to use the tree-level result in eq. (2.50), basically treating it as a two-point vertex. In addition, at this order there is the ϕ^4-term in the EMT, see eq. (2.33), which we call $T^{(1)}_{\mu\rho}$ and denote it by a filled square with four legs. Diagrammatically, the one-loop TWI looks like

$\sum_\mu q_\mu \Bigg($ 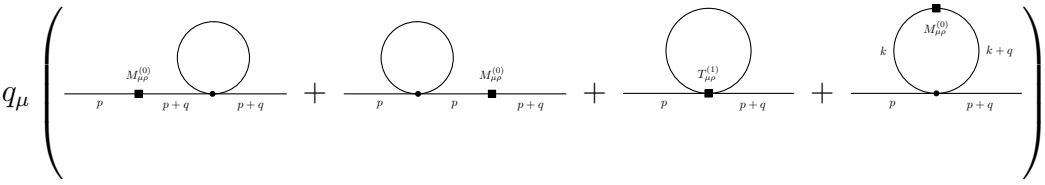

$\Bigg)$

$=$ 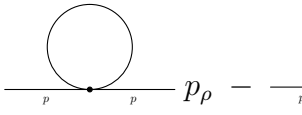

$p_\rho \; -$ 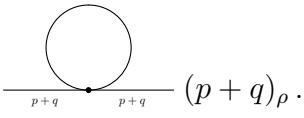

$(p+q)_\rho\,.$ (2.53)

Mimicking the order of the diagrams above, the left-hand side of the one-loop TWI is

$$\begin{aligned}\sum_\mu q_\mu \Omega^{(1)}_{\mu\rho}(p,q) = \sum_\mu q_\mu \Bigg(& \tilde{D}^{(0)}(p^2)\; M^{(0)}_{\mu\rho}(p,q)\; \tilde{D}^{(0)}((p+q)^2)\; T\; \tilde{D}^{(0)}((p+q)^2) \\ & + \tilde{D}^{(0)}(p^2)\; T\; \tilde{D}^{(0)}(p^2)\; M^{(0)}_{\mu\rho}(p,q)\; \tilde{D}^{(0)}((p+q)^2) \\ & + \delta_{\mu\rho}\; \tilde{D}^{(0)}(p^2)\; T\; \tilde{D}^{(0)}((p+q)^2) \\ & - \frac{\lambda}{2}\; \tilde{D}^{(0)}(p^2) \int_k \tilde{D}^{(0)}(k^2)\; M^{(0)}_{\mu\rho}(k,q)\; \tilde{D}^{(0)}((k+q)^2)\; \tilde{D}^{(0)}((p+q)^2) \Bigg),\end{aligned} \tag{2.54}$$

where $T = -\frac{\lambda}{2}\int_k \tilde{D}^{(0)}(k^2)$ is the tadpole loop. For the right-hand side of the TWI we expect

$$\sum_\mu q_\mu \Omega^{(1)}_{\mu\rho}(p,q) = T\; \tilde{D}^{(0)}((p+q)^2)^2 (p+q)_\rho - T\; \tilde{D}^{(0)}(p^2)^2 p_\rho. \tag{2.55}$$

From here, we see that only the first three lines in eq. (2.54) should combine to give the right-hand side of the TWI, and the last line has to be zero. Using the tree-level TWI, eq. (2.51), in eq. (2.54) one can quickly verify that this indeed happens. For the last diagram on the left-hand side in eq. (2.53) to vanish, we have to regularise the integral in a regularisation scheme that preserves translation symmetry. Then, the integral can be split and the momentum shifted such that the two integrals cancel each other.

3

Gradient flow

The gradient flow was recently developed by Lüscher in [13–17]. It is becoming a popular tool as it has remarkable renormalisation properties. In the first section of this chapter we will introduce the gradient flow for scalar field theory. In the second section we will discuss its usefulness for the determination of the EMT from the TWI.

3.1 Gradient flow in scalar field theory

In this section we introduce the gradient flow for ϕ^4-theory and discuss the perturbative renormalisation of the flow field in d dimensions. We will see that the definition of the flow equation is determined to take a simple form when requiring a renormalisable theory.

3.1.1 Flow equation

We define the flow of the scalar field via the flow equation [32]

$$\partial_t \bar{\varphi}_t(x) = \sum_\sigma \partial_\sigma^2 \bar{\varphi}_t(x), \tag{3.1}$$

where the flow time t and the flow field $\bar{\varphi}_t(x)$ were introduced. The flow time is of dimension two. The flow field at zero flow time is bounded to be the scalar field $\phi(x)$,

$$\bar{\varphi}_t(x)|_{t=0} = \phi(x). \tag{3.2}$$

The solution of the flow equation can best be found in momentum space, and from there the solution in position space using the convolution theorem,

$$\tilde{\bar{\varphi}}_t(p) = \tilde{K}_t(p^2)\ \tilde{\phi}(p), \tag{3.3}$$

$$\bar{\varphi}_t(x) = \int d^d y\ K_t(x-y)\ \phi(y), \tag{3.4}$$

where we defined the kernel in momentum and position space,

$$\tilde{K}_t(p^2) = e^{-tp^2}, \tag{3.5}$$

$$K_t(x-y) = \int_p e^{ip(x-y)}\ e^{-tp^2}. \tag{3.6}$$

Evaluating the Gaussian integral in the second equation for the kernel yields

$$K_t(x) = (4\pi t)^{-d/2}\ e^{-\frac{x^2}{4t}}. \tag{3.7}$$

From the momentum space solution we see that the large momenta are exponentially suppressed in correlation functions containing the flow field. The flow damps quantum fluctuations. $K_t(x)$ decays exponentially like a Gaussian function so that the flow has a smoothing effect on the fields at the boundary which are smeared with a root mean square radius of $r = \sqrt{2dt}$. The situation is sketched in fig. 3.1: the scalar field ϕ lies at the boundary, the flow field $\bar{\varphi}_t$ lies in the bulk where $t > 0$. The two fields are connected via the boundary condition (3.2), and the boundary field is smeared out due to the evolution along the flow time t with radius r.

We can formulate the combination of the scalar field theory at the boundary and the flow equation that evolves the flow fields into the bulk as a local field theory in $d+1$ dimensions. The flow field $\varphi(t,x)$ is now an independent field [15]. The boundary condition still holds. The constraint given by the flow equation is implemented using a Lagrange multiplier field $L(t,x)$. The action of the $(d+1)$-dimensional theory is then composed of the Euclidean action of ϕ^4-theory at the

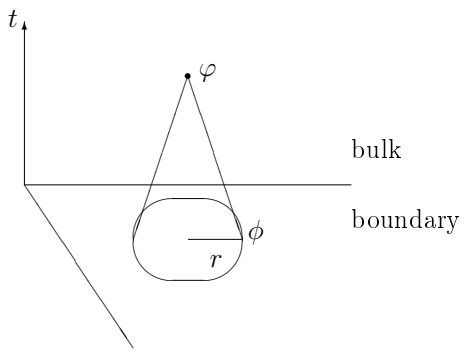

Figure 3.1 *Visualisation of the smearing property of the flow.*

boundary plus the action in the bulk,

$$S = S_{\text{boundary}} + S_{\text{bulk}} \tag{3.8}$$

$$S_{\text{boundary}} = \int d^d x \, \left(\frac{1}{2} \sum_{\mu} (\partial_\mu \phi)^2 + \frac{m^2}{2} \phi^2 + \frac{\lambda}{4!} \phi^4 \right) \tag{3.9}$$

$$S_{\text{bulk}} = \int_0^\infty dt \int d^d x \; L(t,x) \left(\partial_t - \sum_{\sigma} \partial_\sigma^2 \right) \varphi(t,x). \tag{3.10}$$

Performing the path integral over the Lagrange multiplier field yields a delta function which ensures that the flow field solves the flow equation,

$$\prod_{t,x} \delta \left(\varphi(t,x) - \bar{\varphi}_t(x) \right). \tag{3.11}$$

3.1.2 Feynman rules

The flow field enters into two propagators, a φL-propagator coming from the quadratic bulk action and a $\varphi\varphi$-propagator coming from the coupling of the flow field to the boundary field through the boundary condition (3.2). There is also an implicit coupling of the Lagrange multiplier field to the boundary field which can be prevented by decomposing the flow field according to

$$\varphi(t,x) = \int d^d y \; K_t(x-y) \; \phi(y) + \varphi'(t,x). \tag{3.12}$$

The first term in eq. (3.12) is the solution of the flow equation (3.1) thus dropping out in the bulk action. The second term $\varphi'(t,x)$ satisfies homogeneous boundary conditions. Hence, the φL-propagator coincides with the $\varphi' L$-propagator. It is the Green's function of the differential operator in the bulk action,

$$\left(\partial_t - \sum_\sigma \partial_\sigma^2\right) \langle \varphi(t,x) L(s,y)\rangle = \delta(t-s)\ \delta^d(x-y). \tag{3.13}$$

The boundary condition $\langle \varphi(t=0,x) L(s>0,y)\rangle = 0$ holds since $\varphi'(t=0,x)=0$. The solution to eq. (3.13) together with the boundary condition is

$$\langle \varphi(t,x) L(s,y)\rangle = \theta(t-s)\ K_{t-s}(x-y). \tag{3.14}$$

The φL-propagator vanishes for $t \leq s$ so that φ is always further in the bulk than L. It reads in momentum space

$$\langle \tilde{\varphi}(t,p) \tilde{L}(s,q)\rangle = (2\pi)^d\ \delta^d(p+q)\ \theta(t-s)\ \tilde{K}_{t-s}(p^2). \tag{3.15}$$

The $\varphi\varphi$-propagator in position and momentum space can be obtained using eq. (3.12) and Fourier transformation,

$$\langle \varphi(t,x)\varphi(s,y)\rangle = \int d^dz\ d^dz'\ K_t(x-z)\ K_s(y-z')\ D(z-z') \tag{3.16}$$

$$\langle \tilde{\varphi}(t,p)\tilde{\varphi}(s,q)\rangle = (2\pi)^d\ \delta^d(p+q)\ \tilde{D}(p^2)\ \tilde{K}_{t+s}(p^2), \tag{3.17}$$

where we defined the scalar propagator $D(x)$, or $\tilde{D}(p^2)$, as usual, see fig. 2.1. The only surviving correlation function is the one including two boundary fields when expanding $\langle\varphi\varphi\rangle$ using eq. (3.12). The combinations with one or two fields φ' are zero as there are no appropriate quadratic terms in the action (3.8). Contractions involving fields at the boundary are automatically incorporated in eqs. (3.16, 3.17). This includes the mixed propagators with one bulk and one boundary field as well as the free scalar propagator at zero flow time.

Note that in the limit of zero flow time contact terms arise,

$$\lim_{t\to 0}\langle \varphi(t,x) L(0,y)\rangle = \delta(x-y), \tag{3.18}$$

which is evident from eqs. (3.6) and (3.14).

Since the bulk action is only quadratic in the fields there are no additional vertices in the bulk and we are left with the usual four-point vertex from the boundary theory. The momentum space Feynman rules of the $(d+1)$-dimensional theory that appear in addition to the ones in fig. 2.1 are summarised in fig. 3.2. The flow propagator (3.14) is marked with an arrow pointing in the direction of the flow. In order to distinguish the bulk from the boundary theory we add labels for the flow time whenever $t, s > 0$.

Figure 3.2 *Feynman rules in d+1 dimensions for scalar ϕ^4-theory plus gradient flow that appear in addition to the ones in fig. 2.1. The flow field propagator (3.17) differs from the scalar propagator in the flow time labels. The flow propagator (3.15) is marked with an arrow pointing in the direction of the flow.*

The bulk fields do not need to be renormalised. The reason is that there are no interaction terms in the bulk so that no loops exist at $t > 0$. Loop divergencies appear only at the level of the boundary theory which are canceled by the renormalisation of the fields and couplings of ϕ^4-theory as usual.

3.1.3 Jacobian

The flow equation (3.1) allows for moving forward and backward in the flow time. The Jacobian associated to the invertible map $\bar{\varphi}_t(x) \mapsto \bar{\varphi}_s(x)$ is

$$\begin{aligned} J(t,x;s,y) &= \frac{\partial \bar{\varphi}_t(x)}{\partial \bar{\varphi}_s(y)} \\ &= \int_p e^{ip(x-y)} \tilde{K}_{t-s}(p^2). \end{aligned} \tag{3.19}$$

The Jacobian was first discussed in [13]. It can be determined exactly for scalar theory due to the simple form of the flow equation,

$$J(t,x;s,y) = (4\pi(t-s))^{-d/2}\, e^{-\frac{|x-y|^2}{4(t-s)}}. \tag{3.20}$$

3.1.4 Flow as the gradient of the action

If we were to define the flow equation as the gradient of the action as it is done for pure gauge theory [14],

$$\partial_t \varphi = -\left.\frac{\delta S}{\delta \phi}\right|_{\phi=\varphi}, \tag{3.21}$$

the flow equation would read

$$\partial_t \varphi = \sum_\sigma \partial_\sigma^2 \varphi - m^2 \varphi - \frac{\lambda}{3!}\varphi^3, \tag{3.22}$$

and the bulk action would be

$$S_{\text{bulk}} = \int_0^\infty dt \int d^d x \; L \left(\left(\partial_t - \sum_\sigma \partial_\sigma^2 + m^2 \right) \varphi + \frac{\lambda}{3!}\varphi^3 \right). \tag{3.23}$$

Here we omit stating the dependence on t and x explicitly for better readability. The Feynman rules for the $(d+1)$-dimensional theory change accordingly. They are the same as in fig. 2.1 and fig. 3.2 plus a vertex in the bulk which we denote by an open circle, see fig. 3.3. Furthermore, the mass appears in the kernel,

$$\tilde{K}_t(p^2) = e^{-t(p^2+m^2)}. \tag{3.24}$$

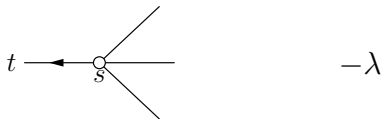

Figure 3.3 *Additional vertex to the Feynman rules of the $(d+1)$-dimensional theory when defining the flow as the gradient of the action. The open circle marks a vertex in the bulk. The lines without arrow represent flow fields at flow time s, the line with arrow represents L, the start of a flow propagator flowing from s to $t > s$.*

We have to expect that divergencies in the bulk can appear in the self-energy diagrams similar to the ones in fig. 2.3 with one or two flow vertices, see fig. 3.4.

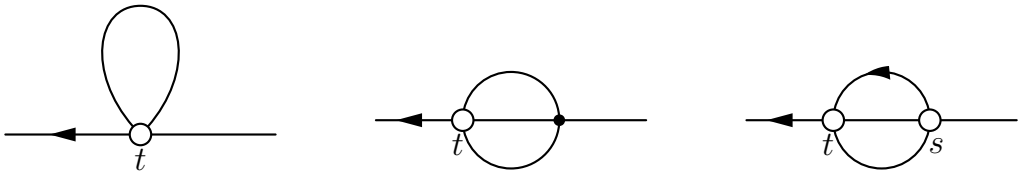

Figure 3.4 *All potential divergent diagrams in the bulk when defining the flow as the gradient of the action.*

The corresponding loop integrals are

$$\Gamma^{(1)}_{L\varphi} = -\frac{\lambda}{2}\int_k \tilde{D}(k^2)\ \tilde{K}_{2t}(k^2) \tag{3.25}$$

$$\Gamma^{(2)}_{L\phi} = \frac{\lambda^2}{3!}\int_k\int_q \tilde{D}(k^2)\ \tilde{D}(q^2)\ \tilde{D}((k+q+p)^2)\ \ \tilde{K}_t(k^2+q^2+(k+q+p)^2) \tag{3.26}$$

$$\Gamma^{(2)}_{L\varphi} = \frac{\lambda^2}{2}\int_k\int_q \tilde{D}(q^2)\ \tilde{D}((k+q+p)^2)\ \ \theta(t-s)\ \tilde{K}_{t-s}(k^2)\ \ \tilde{K}_{t+s}(q^2+(k+q+p)^2), \tag{3.27}$$

where p is the external momentum and the superscript indicates the order in λ.

We will eventually have to integrate over the flow times assigned to each flow vertex from zero to infinity as external propagators will be added to the expressions for Γ in calculations. Consider the following integral

$$I(k,p) = \int_0^\infty dt\ f(t)\ e^{-t(uk^2+v(k+p))}. \tag{3.28}$$

Integrating by parts yields

$$I(k,p) = \frac{f(0)}{uk^2+v(k+p)^2} + \mathcal{O}(k^{-4}), \tag{3.29}$$

which can be also expressed as an integral including a delta function,

$$I(k,p) = \int_0^\infty dt\ \delta(t)\frac{f(t)}{uk^2+v(k+p)^2} + \mathcal{O}(k^{-4}). \tag{3.30}$$

It follows that the exponential function in eq. (3.28) can be replaced by a delta function divided by a function of the loop momentum,

$$e^{-t(uk^2+v(k+p))} \to \frac{\delta(t)}{uk^2+v(k+p)^2}. \tag{3.31}$$

Exchanging a vertex at the boundary with a flow vertex adds factors of $\tilde{K}_t$ into the loop integral which in turn leads to an increase of the power of the loop momentum in the denominator. Applied to the loop integrals in eqs. (3.25-3.27) we find by power counting that the flow renders all of them convergent in three dimensions. Thus, also the modified flow action does not produce divergencies in the bulk, and again the bulk fields do not need to be renormalised. Note that if there were a divergence it would sit at the boundary due to the delta function.

We also have to examine the effect of the couplings in the new bulk action (3.23). Renormalising the couplings at the boundary according to

$$m = Z_m m_R^2, \qquad \lambda = \lambda_R Z_\lambda, \tag{3.32}$$

yields

$$S_{\text{bulk}} = \int_0^\infty dt \int d^d x \, \left(L \left(\partial_t - \sum_\sigma \partial_\sigma^2 + Z_m m_R^2 \right) \varphi + L \, Z_\lambda \frac{\lambda_R}{3!} \, \varphi^3 \right). \tag{3.33}$$

The Z-factors contain divergencies which do not cancel with any divergencies coming from loop integrals as all loop integrals in the bulk are convergent. The Z-factors however introduce divergencies in the bulk. Hence, adding bare couplings to the bulk action leads to non-renormalisable divergencies. In order to have a renormalisable theory we are left with the simple flow equation (3.1) and bulk action (3.10) where the bulk fields do not renormalise.

3.2 Translation Ward identity along the flow

We would like to use the flow to determine the EMT. The programme was first suggested in [28] for pure gauge theory. The reasoning for the suitability of the flow is much easier in the case of scalar field theory due to the simple structure of the flow equation and the consequential simpler Feynman rules and renormalisation properties.

We derived in sec. 2.4 the TWI (2.37) for a generic observable $\mathcal{P}$, a function of fields at the boundary. Let us now consider an observable P_T which depends only

on the flow fields $\bar{\varphi}_T$ at flow time $T > 0$. The corresponding TWI reads

$$\sum_{\mu} \partial_\mu \langle T_{\mu\rho}(x) P_T \rangle = -\langle \delta_{x,\rho} P_T \rangle. \tag{3.34}$$

The local variation of a probe under a translation in direction $\hat{\rho}$ at zero flow time is given in eq. (2.36). For the local variation of a probe at non-zero flow time which is a function of the flow field and derivatives of the flow field $\bar{\varphi}_t$, we have to use the chain rule,

$$\delta_{x,\rho} P_T = \int d^d y \left(\frac{\partial P_T}{\partial \bar{\varphi}_T(y)} + \sum_{\tau} \frac{\partial P_T}{\partial(\partial_\tau \bar{\varphi}_T(y))} \partial_\tau + ... \right) J(T, y; 0, x)\ \partial_\rho \phi(x). \tag{3.35}$$

$\bar{\varphi}_T$ is a solution of the flow equation (3.1) and the Jacobian is defined in eq. (3.19). We are interested in the divergence structure of $\delta_{x,\rho} P_T$. Expressing the Jacobian through eq. (3.20),

$$\delta_{x,\rho} P_T \propto \int d^d y\ \left(\frac{\partial P_T}{\partial \bar{\varphi}_T(y)} + \sum_{\tau} \frac{\partial P_T}{\partial(\partial_\tau \bar{\varphi}_T(y))} \partial_\tau + ... \right) e^{-\frac{|y-x|^2}{4T}} \partial_\rho \phi(x), \tag{3.36}$$

we see that no divergences occur. The operator in parentheses is a function of fields at positive flow time only. Even as a composite operator it does not need to be renormalised as inserting any kind of operator that is defined at positive flow time into correlation functions is finite. Any propagator attached to an operator at $T > 0$ features an exponential function of the momentum so that large momenta are suppressed. It follows automatically that the specific combination of the operator in parentheses and the boundary field in eq. (3.36) is finite as well. The integration over y does not give a divergence either. Therefore, the differential operator $\delta_{x,\rho}$ does not generate any divergencies and thereby requires no renormalisation when applied to an observable at flow time $T > 0$. Hence, it is safe to use probes at positive flow time in the TWI.

4

Scalar energy-momentum tensor on the lattice

Having established a sound understanding of the TWI, the EMT, and the gradient flow in scalar ϕ^4-theory in the continuum we are now in the position to examine these quantities on the lattice. As we will see the challenge is the breaking of translation symmetry when discretising space and time which leads to additional terms in the TWI and which in turn renders the EMT divergent. We will first discuss the properties of lattice scalar ϕ^4-theory in detail. Then, the TWI and the renormalisation of the EMT on the lattice are derived. Finally, the advantage of using the gradient flow will be explained.

4.1 Scalar field on the lattice

We regularise the theory by introducing a cubic space-time lattice Λ,

$$\Lambda = a\mathbb{Z}^3 = \{x \mid x_\mu/a \in \mathbb{Z}\}\,, \tag{4.1}$$

where a is the lattice spacing. The lattice action for the real, bare scalar field ϕ in three dimensions close to the GFP is, compare with the Lagrangian in the

continuum (2.28),

$$S = a^3 \sum_{x\in\Lambda} \left(\frac{1}{2} \sum_{\mu} \hat{\partial}_\mu \phi \hat{\partial}_\mu \phi + \frac{1}{2} m^2 \phi^2 + \frac{\lambda}{4!} \phi^4 \right), \tag{4.2}$$

where $\hat{\partial}_\mu$ is the forward derivative defined as usual, see eq. (B.6). The dimensions of the field and couplings are

$$[\phi] = 1/2, \quad [m] = 1, \quad [\lambda] = 1. \tag{4.3}$$

4.1.1 Renormalisation and Feynman rules

Defining the renormalised field ϕ_R, renormalised mass m_R and renormalised coupling λ_R via

$$\phi = Z^{1/2}\phi_R, \qquad \delta_Z = Z - 1, \qquad \delta_m = m^2 Z - m_R^2, \qquad \delta_\lambda = \lambda Z^2 - \lambda_R, \tag{4.4}$$

yields

$$\begin{aligned} S = a^3 \sum_{x\in\Lambda} \Bigg(& \frac{1}{2} \sum_{\mu} \hat{\partial}_\mu \phi_R \hat{\partial}_\mu \phi_R + \frac{1}{2} m_R^2 \phi_R^2 + \frac{\lambda_R}{4!} \phi_R^4 \\ & + \frac{1}{2} \delta_Z \sum_{\mu} \hat{\partial}_\mu \phi_R \hat{\partial}_\mu \phi_R + \frac{1}{2} \delta_m \phi_R^2 + \frac{1}{4!} \delta_\lambda \phi_R^4 \Bigg). \end{aligned} \tag{4.5}$$

The momentum space Feynman rules for the action with renormalised fields and couplings are presented in fig. 4.1. A detailed derivation can be found in app. B.3.1. $\tilde{D}(\hat{p}^2)$ is the Feynman propagator in momentum space, eq. (B.38), and the lattice momentum $\hat{p}_\mu$ and its square $\hat{p}^2$ are defined as usual, eqs. (B.9, B.10).

We need to impose three independent conditions to determine the renormalisation constants δ_Z, δ_m and δ_λ. Denoting the self-energy, the sum of all one-particle irreducible, amputated diagrams with two external legs except the tree level, by $\Pi(\hat{p}^2)$ we can rewrite the full propagator $\tilde{\Delta}(\hat{p}^2)$ as geometric series,

$$\tilde{\Delta}(\hat{p}^2) = \tilde{D}(\hat{p}^2) \sum_{n=0}^{\infty} \left(\Pi(\hat{p}^2) \tilde{D}(\hat{p}^2) \right)^n = \frac{\tilde{D}(\hat{p}^2)}{1 - \Pi(\hat{p}^2)\tilde{D}(\hat{p}^2)} = \frac{1}{\hat{p}^2 + m^2 - \Pi(\hat{p}^2)}, \tag{4.6}$$

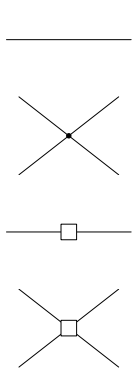

$$\tilde{D}(\hat{p}^2) = \frac{1}{\hat{p}^2 + m_R^2}$$

$$-\lambda_R$$

$$-\delta_Z \hat{p}^2 - \delta_m$$

$$-\delta_\lambda$$

Figure 4.1 *Feynman rules for scalar ϕ^4-theory on the lattice. The dot represents the interaction vertex, the empty square represents a counterterm.*

and define the inverse full propagator as

$$\Gamma^{(2)}(\hat{p}^2) = \hat{p}^2 + m_R^2 - \Pi(\hat{p}^2). \tag{4.7}$$

Let us consider the following renormalisation scheme:

$$\Pi(\hat{p}^2)\big|_{\hat{p}^2=-m_R^2} = 0 \tag{4.8}$$

$$\frac{d}{d\hat{p}^2}\Pi(\hat{p}^2)\bigg|_{\hat{p}^2=-m_R^2} = 0 \tag{4.9}$$

$$\Gamma^{(4)}(\hat{p}^2)\big|_{s=t=u=0} = -\lambda_R. \tag{4.10}$$

The first two conditions imply that the pole of the full propagator occurs at $\hat{p}^2 = -m_R^2$, and has residue one. In the third renormalisation condition $\Gamma^{(4)}(\hat{p}^2)$ represents all one-particle irreducible, amputated diagrams with four external legs. The Mandelstam variables are $s = (p_1 + p_2)^2 = (p_3 + p_4)^2$, $t = (p_1 - p_3)^2 = (p_2 - p_4)^2$, $u = (p_1 - p_4)^2 = (p_2 - p_3)^2$, where p_1, p_2 are the incoming momenta and p_3, p_4 are the outgoing momenta.

Having established the Feynman rules, let us review the choice of lattice derivatives in the action, eqs. (4.2, 4.5). We cannot use the symmetric derivative, eq. (B.8), as it would lead to a doubling problem analogous to the one we encounter in the case of fermionic fields. Symmetric derivatives would cause the propagator to contain $\bar{p}^2$ instead of $\hat{p}^2$, eqs. (B.10, B.9). The crucial difference is the missing factor of $1/2$ in the argument of the sine function in $\bar{p}^2$: without it $\sin(ap_\mu + \pi)$ lies within the Brillouin zone which leads to eight different momenta

that can induce a pole in the propagator. This in turn means that there is not one but eight scalar particles. In general, there are 2^d particles. In the scalar case one can choose forward derivatives giving $\hat{p}^2$ in the propagator which is unambiguous within the Brillouin zone and thus has only one pole.

4.1.2 Renormalisation at one-loop level

The self-energy at one-loop level is given by the tadpole diagram, see sec. B.3.2, plus a counterterm,

$\Pi(\hat{p}^2) =$  $+$

$$
\begin{aligned}
&= -\frac{\lambda_R}{2} \int_k \frac{1}{\hat{k}^2 + m_R^2} - \delta_Z \hat{p}^2 - \delta_m \\
&= -\frac{\lambda_R}{2a} \int_{-\pi}^{\pi} \frac{d^3k}{(2\pi)^3} \frac{1}{4\sum_\mu \sin^2 \frac{k_\mu}{2} + a^2 m_R^2} - \delta_Z \hat{p}^2 - \delta_m,
\end{aligned}
\tag{4.11}
$$

where we used the lattice integral abbreviation (B.5) in the second line and rescaled the momentum in the third line so that the integral is dimensionless. Since the tadpole does not depend on the external momentum p we get $\delta_Z = 0$ so that $Z = 1 + \mathcal{O}(\lambda_R^2)$. Taking the continuum limit of the integral gives

$$
\delta_m = -\frac{\lambda_R}{2a} Z_0, \tag{4.12}
$$

where we defined the lattice integral

$$
\begin{aligned}
Z_0 &= \int_{-\pi}^{\pi} \frac{d^3k}{(2\pi)^3} \frac{1}{4\sum_\mu \sin^2 \frac{k_\mu}{2}} \\
&= 0.252731... \, .
\end{aligned}
\tag{4.13}
$$

The above integral can be evaluated using numerical integration as we did with Mathematica. Therefore, at one-loop level the renormalised mass is related to the bare one by a linearly divergent additive renormalisation,

$$
m_R^2 = m^2 + \frac{\lambda_R}{2a} Z_0. \tag{4.14}
$$

Let us now turn to the renormalisation of the coupling. Since the theory is super-renormalisable and the only two divergent diagrams have two external legs, see fig. 2.3, we do not need a counterterm for λ. Nonetheless, an explicit calculation at one-loop level shall be included for completeness. The vertex function at one-loop level is

$\Gamma^{(4)}(\hat{p}^2) =$ 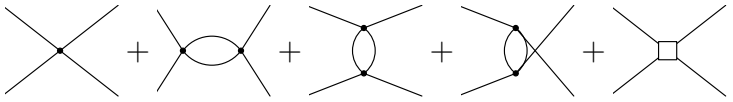 (4.15)

$$= -\lambda_R + \lambda_R^2 \left(V(s) + V(t) + V(u)\right) - \delta_\lambda. \tag{4.16}$$

The function $V(s)$ is defined by the loop integral

$$V(s) = \frac{1}{2} \int_k \frac{1}{\hat{k}^2 + m_R^2} \frac{1}{\hat{q}^2 + m_R^2}, \tag{4.17}$$

where $q_\mu = p_{1\mu} + p_{2\mu} + k_\mu$. Power counting reveals that the loop integral has a finite continuum limit: there are three powers of k in the numerator from the integration measure, and four powers of k in the denominator due to the two propagators as integrand. Hence, the degree of divergence is -1. Therefore we can take $a \to 0$ so that up to cutoff effects

$$V(s) = \frac{1}{2} \int \frac{d^3k}{(2\pi)^3} \frac{1}{k^2 + m_R^2} \frac{1}{q^2 + m_R^2}. \tag{4.18}$$

Further evaluation involving Feynman parametrisation (A.3) and the integral (A.7) yields

$$V(s) = \frac{1}{16\pi} \int_0^1 \frac{dx}{\sqrt{m^2 + x(1-x)s}} \tag{4.19}$$

which can be reduced to

$$V(s) = \frac{1}{8\pi} \frac{1}{\sqrt{s}} \operatorname{arccot}\left(\frac{2m_R}{\sqrt{s}}\right). \tag{4.20}$$

The complete calculation of $V(s)$ can be found in app. B.3.3. The expressions for $V(t)$ and $V(u)$ are obtained in a similar way and are in fact the above one with s replaced by t or u respectively. Taking the limit $s, t, u \to 0$ and applying the

renormalisation condition (4.10) gives

$$\delta_\lambda = \frac{3}{16\pi}\frac{\lambda_R^2}{m_R}. \tag{4.21}$$

So, the renormalised coupling is related to the bare one through a finite multiplicative renormalisation,

$$\lambda = \lambda_R \left(1 + \frac{3}{16\pi}\frac{\lambda_R}{m_R}\right). \tag{4.22}$$

4.1.3 Continuum limit

Converging towards the GFP three-dimensional scalar ϕ^4-theory has got two relevant operators, see sec. 2.3. Therefore the theory is determined by specifying the values of two dimensionful parameters. The continuum limit of the lattice theory is approached when the dimensionful parameters are small in units of the ultraviolet cutoff a^{-1}, e.g. $a^{-1} \gg m_R, \lambda_R$, or equivalently $\check{m}_R, \check{\lambda}_R \ll 1$. The inverted hat indicates again dimensionless quantities which are used in lattice calculations, see chap. 5. Eq. (4.22) shows that λ undergoes only a finite multiplicative renormalisation. Hence, the continuum limit can be obtained by taking the limit $\check{\lambda} \to 0$ instead of $\check{\lambda}_R \to 0$. For the same reason λ can be used to set the value of the lattice spacing. So, the feature of our theory of being super-renormalisable leaves us with the following two dimensionful parameters that have to be fixed externally:

$$a^{-1} \gg m_R, \lambda \quad \Rightarrow \quad \check{m}_R \ll 1, \quad \check{\lambda} \ll 1. \tag{4.23}$$

In practice one approaches the continuum by evaluating an observable following lines of constant physics towards a fixed point, which is the GFP in our case. It is then possible to extract the continuum value from a plateau that forms within error bars, or by extrapolation.

In order to find lines of constant physics numerically we need the dimensionless

equivalents to eqs. (4.14, 4.22),

$$\breve{m}_R^2 = \breve{m}^2 + \frac{\breve{\lambda}_R}{2} Z_0 \tag{4.24}$$

$$\breve{\lambda} = \breve{\lambda}_R \left(1 + c\frac{\breve{\lambda}_R}{\breve{m}_R}\right), \tag{4.25}$$

where we called the constant factor $c = \frac{3}{16\pi}$. We introduce the dimensionless constant ρ which distinguishes lines of constant physics and hence different theories,

$$\rho = \frac{\breve{\lambda}}{\breve{m}_R}. \tag{4.26}$$

Using eqs. (4.25-4.26), one can solve for $\breve{\lambda}$ and $\breve{m}$ for small values of $c\rho$,

$$\breve{\lambda} = \breve{\lambda}_R \left(1 + c\rho - c^2\rho^2 + 2c^3\rho^3 - 5c^4\rho^4 + \mathcal{O}((c\rho)^5)\right) \tag{4.27}$$

$$\breve{m}^2 = -\breve{\lambda}_R \frac{Z_0}{2} + \frac{\breve{\lambda}_R^2}{\rho^2}\left(1 + 2c\rho - c^2\rho^2 + 2c^3\rho^3 - 5c^4\rho^4 + \mathcal{O}((c\rho)^5)\right). \tag{4.28}$$

Fig. 4.2 shows lines of constant physics for $\rho = 1.5, 3, 5, 10$ in the $(\breve{\lambda}_R, \breve{m}^2)$-plane. These values for ρ are also the ones we used for the numerical simulations, chap. 5. In fig. 4.3 we plotted $\breve{\lambda}$ as a function of $\breve{\lambda}_R$.

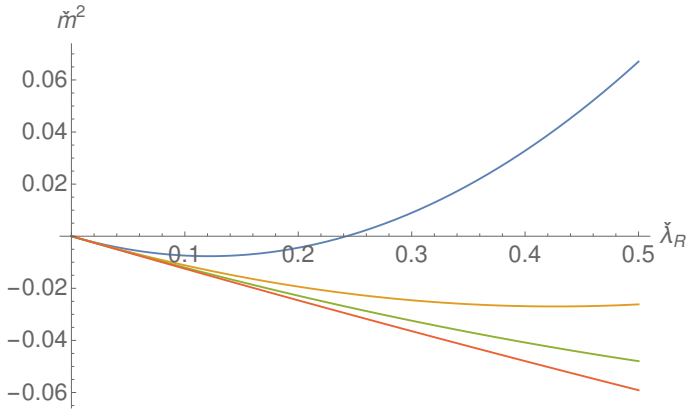

Figure 4.2 *Lines of constant physics in the $(\breve{\lambda}_R, \breve{m}^2)$-plane for ρ=1.5 blue, ρ=3 orange, ρ=5 green, ρ=10 red.*

Finite volume effects can be estimated as it is done in quantum chromodynamics where they are exponential in LM_π. L is the extent of a lattice side in spatial direction and M_π is the mass of the pion. The empirically found rule of thumb

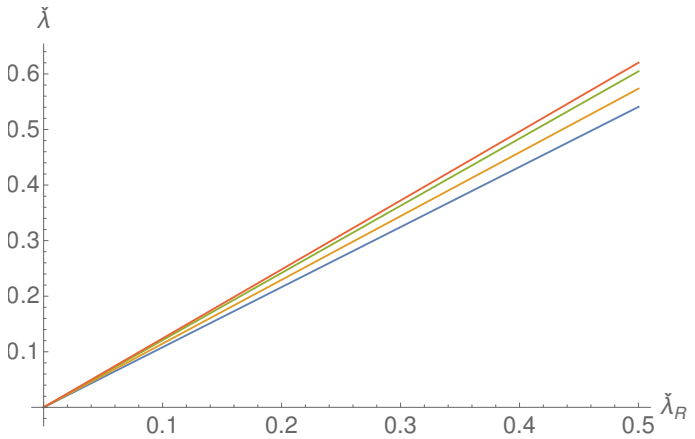

Figure 4.3 *Plot of $\breve{\lambda}$ as a function of $\breve{\lambda}_R$ for ρ=1.5 blue, ρ=3 orange, ρ=5 green, ρ=10 red.*

is that finite size effects are negligible for $LM_\pi > 4$. Replacing M_π with m_R we can estimate finite volume effects by plotting $\exp(-\breve{L}\breve{m}_R)$ which should be smaller than 0.01 for negligible finite size effects of 1% or less. In fig. 4.4 we plotted $\exp(-\breve{L}\breve{m}_R)$ as a function of $\breve{\lambda}_R$, as well as the upper bound 0.01. The renormalised mass for small values of $c\rho$ is

$$\breve{m}_R = \frac{\breve{\lambda}_R}{\rho}\left(1 + c\rho - c^2\rho^2 + 2c^3\rho^3 + \mathcal{O}((c\rho)^4)\right). \tag{4.29}$$

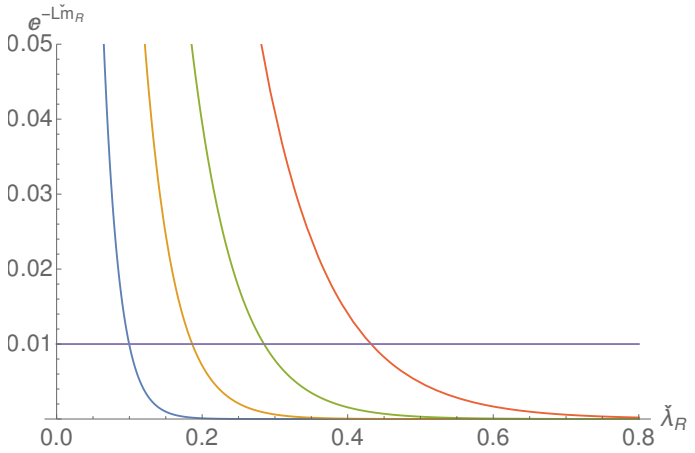

Figure 4.4 *Plot of $exp(-\breve{L}\breve{m}_R)$ as a function of $\breve{\lambda}_R$ for ρ=1.5 blue, ρ=3 orange, ρ=5 green, ρ=10 red. The purple horizontal line at 0.01 marks the upper bound where finite volumes effects become significant.*

In all three figures, 4.2, 4.3 and 4.4, we expanded eqs. (4.27, 4.28, 4.29) up to order ρ^2. Note that the plots for $\rho = 10$ are imprecise since $10c \simeq 0.6$ is not a small enough number to expand in.

We can now use the perturbative results to find reasonable starting values for the simulation. First we choose the lattice size, and a value for the renormalised mass according to the requirement $4/\check{L} \ll \check{m}_R \ll 1$. Next, we decide on a value for ρ which fixes $\check{\lambda}$. $\check{\lambda}$ will be used to set the lattice spacing keeping the physical volume constant as $\check{L} = \alpha/\check{\lambda}$ where α is the proportionality factor by which the lattice is made finer or coarser. Now, depending on which $\check{m}_R$ we pick, we can use fig. 4.4 to determine a sensible value for $\check{\lambda}_R$. Fig. 4.3 can serve as a check if $\check{\lambda}$ and $\check{\lambda}_R$ are compatible. Finally, using fig. 4.2 we can determine the value of $\check{m}$ which gives an approximate region to simulate in to find the desired $\check{m}_R$ in numerical calculations. Explicit numerical examples will be discussed in sec. 5.3. For now, fig. 4.5 displays the lines of constant physics corresponding to different values of ρ in the $(\check{\lambda}, \check{m}^2)$-plane.

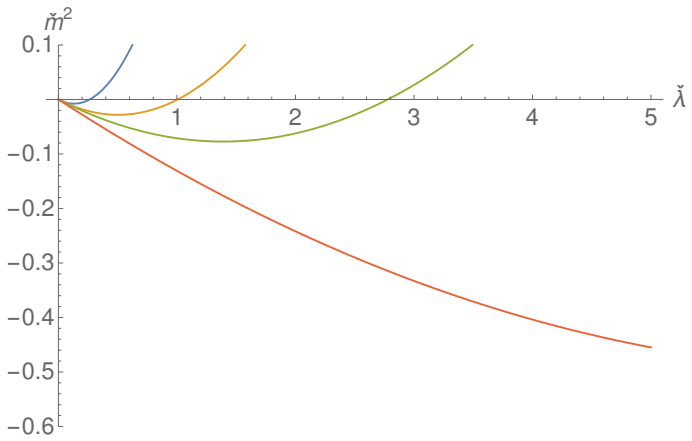

Figure 4.5 *Lines of constant physics in the $(\check{\lambda}, \check{m}^2)$-plane for ρ=1.5 blue, ρ=3 orange, ρ=5 green, ρ=10 red.*

4.1.4 Critical line

We can estimate the critical line where $\check{m}_R = 0$ from the perturbative calculation, in particular from eq. (4.14). The critical bare mass $\check{m}_c$ is

$$\check{m}_c^2 = -\frac{Z_0}{2}\check{\lambda}_R. \tag{4.30}$$

Assuming $\check{\lambda}_R \simeq \check{\lambda}$, we add the critical line to fig. 4.5 in fig. 4.6.

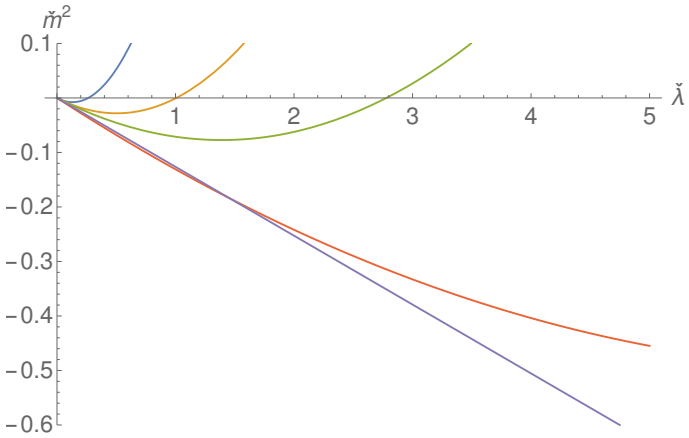

Figure 4.6 *Lines of constant physics and critical line in the $(\check{\lambda}, \check{m}^2)$-plane. Lines of constant physics for ρ=1.5 blue, ρ=3 orange, ρ=5 green, ρ=10 red. Critical line in purple.*

4.1.5 Comparison with numerical data

Fig. 4.6 is the perturbative equivalent of fig. 5.7 produced in sec. 5.3. To compare the perturbative with the numerical results we plot fig. 4.6 again and anticipate the data obtained from numerical simulations for the lines of constant physics in tabs. 5.6 and 5.7, and for the critical line close to the GFP in tab. 5.8 in fig. 4.7. Lines and points in the same colour belong to the same value of ρ or to the critical line. We see a close agreement between the perturbative and the numerical calculation for lines of constant physics with $\rho < 10$ and the critical line close to the GFP. We zoom in on the region around the GFP even more in fig. 4.8 where we don't include the results for $\rho = 10$.

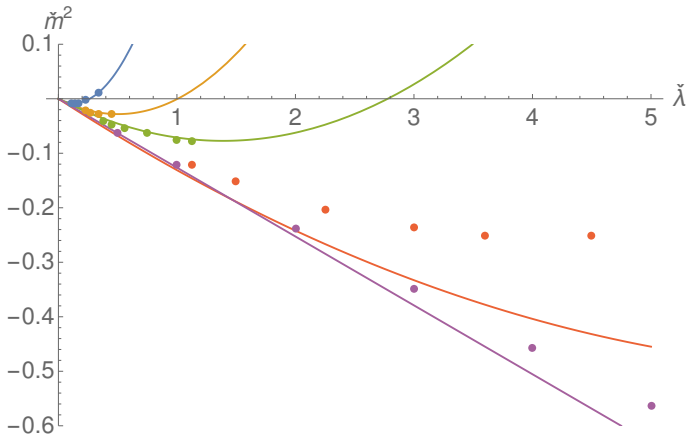

Figure 4.7 *Lines of constant physics and critical line obtained perturbatively (lines) and numerically (points). Lines and points in the same colour belong to the same value of ρ or to the critical line. Lines of constant physics for ρ=1.5 blue, ρ=3 orange, ρ=5 green, ρ=10 red, critical line in purple.*

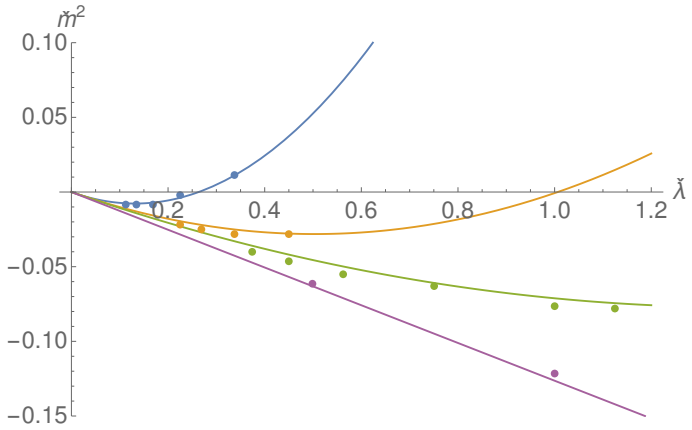

Figure 4.8 *Magnified region around the GFP in fig. 4.7 without data for ρ=10.*

4.2 Energy-momentum tensor on the lattice

In this section it will be shown that the EMT requires renormalisation in a regularisation scheme that breaks translation symmetry like lattice regularisation. The reasons are additional terms appearing compared to the continuum when applying the Leibniz rule for lattice derivatives, see eqs. (C.4) [20]. We will see that the divergences that appear upon inserting the EMT into n-point functions contribute only to the coefficient of the ϕ^2-term in the EMT. We begin the discussion with the derivation of a general Ward identity on the lattice.

4.2.1 General Ward identity on the lattice

The expectation value of a generic probe $\mathcal{P}$ is given by the path integral

$$\langle \mathcal{P} \rangle = \frac{1}{\mathcal{Z}} \int D\phi \, \mathcal{P}(\phi) \, e^{-S(\phi)}, \tag{4.31}$$

where $\mathcal{Z}$ is the normalisation (B.13), and $\mathcal{P}$ and S are functions of the scalar field ϕ. Changing the field variables using a unitary local transformation $\phi \to \phi + \delta\phi$ yields

$$\langle \mathcal{P} \rangle = \frac{1}{\mathcal{Z}} \int D\phi \, \mathcal{P}(\phi + \delta\phi) e^{-S(\phi+\delta\phi)}. \tag{4.32}$$

The Jacobian is trivially 1 because of the unitarity of the transformation. The Taylor expansion of a function of the field under a small variation is

$$F(\phi + \delta\phi) = F(\phi) + \sum_x \frac{\partial F}{\partial \phi} \, \delta\phi + \mathcal{O}(\delta\phi^2). \tag{4.33}$$

Note that we do not have to include derivatives with respect to derivatives of the field as it has to be done in the continuum, compare with eq. (2.36). The reason is that one way of looking at derivatives of fields on the lattice is to treat them as finite differences so that any operator is a function of the fields only. Using the above expansion in eq. (4.32) and cancelling the zeroth order terms on the left-hand and right-hand side we find the general form of the integrated Ward identity,

$$\langle \mathcal{P} \, \hat{\delta} S \rangle = \langle \hat{\delta} \mathcal{P} \rangle, \tag{4.34}$$

where we defined

$$\hat{\delta}F = \sum_x \frac{\partial F}{\partial \phi}\, \delta\phi. \tag{4.35}$$

Defining

$$\hat{\delta}F = \sum_x \hat{\delta}_x F, \tag{4.36}$$

we can write down the local Ward identity,

$$\langle \mathcal{P}\ \hat{\delta}_x S\rangle = \langle \hat{\delta}_x \mathcal{P}\rangle. \tag{4.37}$$

4.2.2 Lattice translation Ward identity

Lattice regularisation breaks translation symmetry explicitly, which implies that the EMT needs to be properly renormalised in order to satisfy the correct TWI as the regulator is removed. But how to determine the EMT from a purely discrete context? In the continuum, a local translation of a field ϕ in direction $\hat{\rho}$ is formally given by the exponential of the derivative operator,

$$\phi(x + \alpha(x)\hat{\rho}) = \sum_n \frac{\alpha(x)^n}{n!}\partial_\rho^n \phi(x) = \exp(\alpha\partial_\rho)\phi(x). \tag{4.38}$$

Since ∂_ρ is an anti-hermitian operator, $\exp(\alpha\partial_\rho)$ is a unitary transformation. For a local quantum field theory, the TWI associated to this transformation gives the quantum version of the EMT conservation as discussed in sec. 2.4. On the lattice one can mimic eq. (4.38) by using the transformation $\exp(\alpha\bar{\partial}_\rho)$,

$$\exp(\alpha\bar{\partial}_\rho)\phi(x) = \phi(x) + \alpha(x)\bar{\partial}_\rho\phi(x) + \mathcal{O}(\alpha^2). \tag{4.39}$$

The choice of the central derivative $\bar{\partial}_\rho$, eq. (B.8), is important because it is anti-hermitian, see eq. (C.7), and thus conserves the unitarity of the transformation. Hence, the variation of the scalar field is

$$\delta\phi(x) = \hat{\delta}_\rho\phi(x) = \alpha(x)\,\bar{\partial}_\rho\phi(x). \tag{4.40}$$

The integrated TWI then reads

$$\langle \mathcal{P}\ \hat{\delta}_\rho S\rangle = \langle \hat{\delta}_\rho \mathcal{P}\rangle, \tag{4.41}$$

where we indicated the direction $\hat{\rho}$ of the transformation as a subscript. We define further

$$\hat{\delta}_\rho F = \sum_x \alpha(x)\ \hat{\delta}_{x,\rho} F, \tag{4.42}$$

where

$$\hat{\delta}_{x,\rho} F = \frac{\partial F}{\partial \phi}\ \bar{\partial}_\rho \phi(x). \tag{4.43}$$

The local TWI then reads

$$\langle \mathcal{P}\ \hat{\delta}_{x,\rho} S \rangle = \langle \hat{\delta}_{x,\rho} \mathcal{P} \rangle. \tag{4.44}$$

Note the difference in the definitions of $\hat{\delta}_x$ and $\hat{\delta}_{x,\rho}$ in eqs. (4.36, 4.43),

$$\hat{\delta}_x = \alpha(x) \hat{\delta}_{x,\rho}. \tag{4.45}$$

Note also the difference in the definitions of $\hat{\delta}_{x,\rho}$ on the lattice and $\delta_{x,\rho}$ in the continuum, eq. (2.36).

The scalar action on the lattice is defined in eq. (4.2),

$$S = a^3 \sum_x \left(\frac{1}{2} \sum_\mu \hat{\partial}_\mu \phi \hat{\partial}_\mu \phi + \frac{1}{2} m^2 \phi^2 + \frac{\lambda}{4!} \phi^4 \right). \tag{4.46}$$

We now compute the local variation of the action in the local TWI (4.44) relative to the transformation (4.39). The local variations of a field and forward derivative are

$$\hat{\delta}_{x,\rho} \phi(y) = \delta_{y,x} \bar{\partial}_{\rho,x} \phi(x) \tag{4.47}$$

$$\hat{\delta}_{x,\rho} \hat{\partial}_\mu \phi(y) = (\hat{\partial}_{\mu,y} \delta_{y,x})(\bar{\partial}_{\rho,x} \phi(x)), \tag{4.48}$$

where the additional indices x, y on the derivatives explicitly state on which variable the derivatives act.

Starting with the kinetic term we find

$$\hat{\delta}_{x,\rho} S_{kin} = a^3 \sum_{y,\mu} (\hat{\partial}_{\mu,y} \phi(y))(\hat{\partial}_{\mu,y} \delta_{y,x})(\bar{\partial}_{\rho,x} \phi(x)) \tag{4.49}$$

$$= -a^3 \sum_\mu (\hat{\partial}_{\mu,x} \hat{\partial}^*_{\mu,x} \phi(x))(\bar{\partial}_{\rho,x} \phi(x)). \tag{4.50}$$

In order to formulate the EMT, we need to write the local variation of the action as a total derivative. To do so, we know that forward, backward and symmetric derivative are equal up to order a,

$$\hat{\partial}_\mu \phi = \bar{\partial}_\mu \phi + a D_\mu \tag{4.51}$$

$$\hat{\partial}^*_\mu \phi = \bar{\partial}_\mu \phi - a D_\mu, \tag{4.52}$$

so that we can rewrite eq. (4.50) using the symmetric derivative,

$$\hat{\delta}_{x,\rho} S_{kin} = -a^3 \sum_\mu (\bar{\partial}_\mu \bar{\partial}_\mu \phi(x))(\bar{\partial}_\rho \phi(x)) + a^5 D'_\rho, \tag{4.53}$$

where aD_μ is of order a and $a^2 D'_\rho$ is of order a^2. The two operators are defined in eqs. (C.18, C.21). The Leibniz rule (C.5) gives

$$-\sum_\mu (\bar{\partial}_\mu \bar{\partial}_\mu \phi)(\bar{\partial}_\rho \phi) = -\sum_\mu \bar{\partial}_\mu \left((\bar{\partial}_\mu \phi)(\bar{\partial}_\rho \phi) \right) + \sum_\mu (\bar{\partial}_\mu \phi)(\bar{\partial}_\mu \bar{\partial}_\rho \phi) + a^2 K^{(1)}_\rho. \tag{4.54}$$

Using it again, the second term on the right-hand side is

$$\sum_\mu (\bar{\partial}_\mu \phi)(\bar{\partial}_\mu \bar{\partial}_\rho \phi) = \frac{1}{2} \sum_\mu \bar{\partial}_\rho (\bar{\partial}_\mu \phi)^2 + a^2 K^{(2)}_\rho. \tag{4.55}$$

$a^2 K^{(1)}_\rho$ and $a^2 K^{(2)}_\rho$ are of order a^2, see eqs. (C.25, C.26). Defining the kinetic part of the lattice EMT as

$$T_{\mu\rho,kin} = \bar{\partial}_\mu \phi \bar{\partial}_\rho \phi - \frac{1}{2} \delta_{\mu\rho} \sum_\sigma (\bar{\partial}_\sigma \phi)^2, \tag{4.56}$$

the local variation of the kinetic part of the action reads

$$\hat{\delta}_{x,\rho} S_{kin} = -a^3 \sum_\mu \bar{\partial}_\mu T_{\mu\rho,kin}(x) + a^5 D'_\rho(x) + a^5 K^{(1)}_\rho(x) + a^5 K^{(2)}_\rho(x). \tag{4.57}$$

Similarly, we find for the mass and interaction terms

$$\hat{\delta}_{x,\rho} S_m = -a^3 \sum_\mu \bar{\partial}_\mu T_{\mu\rho,m}(x) + a^5 M_\rho(x)\,, \qquad T_{\mu\rho,m} = -\frac{1}{2} m^2 \delta_{\mu\rho} \phi^2 \tag{4.58}$$

$$\hat{\delta}_{x,\rho} S_\lambda = -a^3 \sum_\mu \bar{\partial}_\mu T_{\mu\rho,\lambda}(x) + a^5 \Lambda_\rho(x)\,, \qquad T_{\mu\rho,\lambda} = -\frac{\lambda}{4!} \delta_{\mu\rho} \phi^4, \tag{4.59}$$

where $a^2 M_\rho$ and $a^2 \Lambda_\rho$ are of order a^2, defined in eqs. (C.32, C.36).

So finally, the local TWI (4.44) expressed with the EMT reads

$$a^3 \sum_\mu \bar{\partial}_\mu \langle T_{\mu\rho}(x) \mathcal{P} \rangle = - \left\langle \hat{\delta}_{x,\rho} \mathcal{P} \right\rangle + a^5 \langle X_\rho \mathcal{P} \rangle, \tag{4.60}$$

where

$$T_{\mu\rho} = \bar{\partial}_\mu \phi \bar{\partial}_\rho \phi - \delta_{\mu\rho} \left(\frac{1}{2} \sum_\sigma (\bar{\partial}_\sigma \phi)^2 + \frac{1}{2} m^2 \phi^2 + \frac{\lambda}{4!} \phi^4 \right), \tag{4.61}$$

$$X_\rho = D'_\rho + K^{(1)}_\rho + K^{(2)}_\rho + M_\rho + \Lambda_\rho. \tag{4.62}$$

The above derivation of the lattice TWI for scalar ϕ^4-theory is explained in detail in app. C where D'_ρ, $K^{(1)}_\rho$, $K^{(2)}_\rho$, M_ρ and Λ_ρ are given explicitly.

X_ρ is a higher-dimensional operator describing the explicit breaking of the symmetry induced by the regulator. Note that its exact form depends on the choice of discretising the derivatives in the action and in eq. (4.39). For example if we were to choose symmetric derivatives in the action (4.46) from the beginning, the term $a^2 D'_\rho$ in eq. (4.53) would not be necessary and thus absent in X_ρ.

X_ρ is classically suppressed by powers of the lattice spacing a. However, the insertion of X_ρ in quantum correlators can lead to contributions that do not vanish when $a \to 0$ as subleading coefficients can combine with divergencies generated in expectation values so that the continuum TWI (2.37) would be violated. Thus, X_ρ and therefore the EMT have to be renormalised. Renormalisation has to be realised in such a way that the correct TWI in the continuum limit is ensured [33].

Let us define the operator

$$Y_\rho = a^2 X_\rho - \sum_\mu \bar{\partial}_\mu T_{\mu\rho}. \tag{4.63}$$

Its renormalised expression is given by the sum of all operators that mix with Y_ρ. These are of equal or lower dimension than Y_ρ and have the same transformation properties as $\bar{\partial}_\mu T_{\mu\rho}$ under the symmetries of the lattice theory. Y_ρ is of mass dimension four but combined with factors of the lattice spacing the dimension of some operators in Y_ρ can be greater than four. We imposed for the Lagrangian

Lorentz symmetry as well as symmetry under $\phi \to -\phi$. Hence, we need at least one derivative to carry the Lorentz index ρ, the number of fields must be greater than zero and even, and the number of derivatives has to be odd. Tab. 4.1 sketches the possible combinations of fields and derivatives up to dimension six ranked according to their dimension d_O.

d_O	mixing operators
6	$\partial^1\phi^{10}$, $\partial^3\phi^6$, $\partial^5\phi^2$
5	$\partial^1\phi^8$, $\partial^3\phi^4$
4	$\partial^1\phi^6$, $\partial^3\phi^2$
3	$\partial^1\phi^4$
2	$\partial^1\phi^2$

Table 4.1 *Possible combinations of fields and derivatives that can mix with Y_ρ ranked according to their dimension d_O.*

The first two lines in tab. 4.1, $d_O = 5$ and 6, are higher-dimensional operators multiplied by powers of the lattice spacing. There are two combinations for $d_O = 4$. The first one is just $\bar{\partial}_\rho\phi^6$. The second one involving three derivatives and two fields gives five different operators:

$$\phi\bar{\partial}_\rho^3\phi, \quad \bar{\partial}_\rho\phi\bar{\partial}_\rho^2\phi, \quad \sum_\mu \phi\bar{\partial}_\rho\bar{\partial}_\mu^2\phi, \quad \sum_\mu \bar{\partial}_\rho\phi\bar{\partial}_\mu^2\phi, \quad \sum_\mu \bar{\partial}_\mu\phi\bar{\partial}_\rho\bar{\partial}_\mu\phi. \tag{4.64}$$

Ultimately, we want to express the TWI with the renormalised EMT. Thus, we need to rewrite all operators that mix with Y_ρ such that they have the same structure as $\sum_\mu \bar{\partial}_\mu T_{\mu\rho}$. This is easily done for the first operator of $d_O = 4$ and the three of lower dimension:

$$\bar{\partial}_\rho\phi^{2n} = \sum_\mu \bar{\partial}_\mu\delta_{\mu\rho}\phi^{2n}. \tag{4.65}$$

The operators in eq. (4.64) can be extracted from the following equations:

$$\sum_\mu \bar\partial_\mu \delta_{\mu\rho}(\phi\bar\partial_\mu\bar\partial_\mu\phi) = \bar\partial_\rho\phi\bar\partial_\rho^2\phi + \underline{\phi\bar\partial_\rho^3\phi} \tag{4.66}$$

$$\sum_\mu \bar\partial_\mu \delta_{\mu\rho}(\bar\partial_\mu\phi\bar\partial_\mu\phi) = 2\underline{\bar\partial_\rho\phi\bar\partial_\rho^2\phi} \tag{4.67}$$

$$\sum_\mu \bar\partial_\mu \delta_{\mu\rho}\left(\sum_\sigma \phi\bar\partial_\sigma^2\phi\right) = \sum_\mu \bar\partial_\rho\phi\bar\partial_\mu^2\phi + \sum_\mu \phi\bar\partial_\rho\bar\partial_\mu^2\phi \tag{4.68}$$

$$\sum_\mu \bar\partial_\mu(\phi\bar\partial_\mu\bar\partial_\rho\phi) = \sum_\mu \bar\partial_\mu\phi\bar\partial_\rho\bar\partial_\mu\phi + \underline{\sum_\mu \phi\bar\partial_\rho\bar\partial_\mu^2\phi} \tag{4.69}$$

$$\sum_\mu \bar\partial_\mu(\bar\partial_\mu\phi\bar\partial_\rho\phi) = \underline{\sum \bar\partial_\rho\phi\bar\partial_\mu^2\phi} + \sum_\mu \bar\partial_\mu\phi\bar\partial_\rho\bar\partial_\mu\phi \tag{4.70}$$

$$\sum_\mu \bar\partial_\mu \delta_{\mu\rho}\left(\sum_\sigma \bar\partial_\sigma\phi\bar\partial_\sigma\phi\right) = 2\underline{\sum_\mu \bar\partial_\mu\phi\bar\partial_\rho\bar\partial_\mu\phi}, \tag{4.71}$$

where we underlined the different operators that mix with Y_ρ in eq. (4.64) which we want to express through the left-hand sides. This can be done for example by combining eqs. (4.66, 4.67), and eqs. (4.69-4.71).

Defining the sum of all operators of higher dimension than four to be Q_ρ the renormalised operator $[Y_\rho]$ can be written as

$$[Y_\rho] = Q_\rho - \sum_\mu \bar\partial_\mu[T_{\mu\rho}], \tag{4.72}$$

where the square brackets indicate a renormalised operator. The renormalised EMT is

$$\begin{aligned}[T_{\mu\rho}] = {} & c\,\bar\partial_\mu\phi\bar\partial_\rho\phi \;+\; c_1\phi\bar\partial_\mu\bar\partial_\rho\phi \\ & +\; \delta_{\mu\rho}\left(c'\sum_\sigma(\bar\partial_\sigma\phi)^2 + c_2\phi^2 + c_3(\bar\partial_\mu\phi)^2 + c_4\phi^4 + c_6\phi^6 + c_7\phi\bar\partial_\mu^2\phi\right),\end{aligned} \tag{4.73}$$

where we collected all the terms with one derivative from tab. 4.1 of dimension $d_O \leq 4$ plus the operators in eq. (4.64) expressed through the left-hand sides in eqs. (4.66-4.71). In principle, the complete mixing of the renormalised EMT

includes even more terms. In addition to the ones above we have to add

$$\sum_{\sigma} \phi \bar{\partial}_{\sigma}^{2} \phi \quad \text{and} \quad \mathbb{1}. \tag{4.74}$$

But inside the TWI the derivative acting on the EMT erases the identity. Furthermore, we are also interested in the integrated version of the TWI since only the integral of the EMT is a physical quantity. Therefore operators that can be expressed as total derivates become redundant. We choose to eliminate

$$\phi \bar{\partial}_{\mu} \bar{\partial}_{\rho} \phi \quad \text{and} \quad \phi \bar{\partial}_{\mu} \bar{\partial}_{\mu} \phi. \tag{4.75}$$

The renormalised EMT we are interested in takes a reduced form:

$$[T_{\mu\rho}]_r = c\, \bar{\partial}_{\mu} \phi \bar{\partial}_{\rho} \phi + \delta_{\mu\rho} \left(c' \sum_{\sigma} (\bar{\partial}_{\sigma} \phi)^2 + c_2 \phi^2 + c_3 (\bar{\partial}_{\mu} \phi)^2 + c_4 \phi^4 + c_6 \phi^6 \right). \tag{4.76}$$

Apart from the EMT we also have to examine the renormalisation of the operator $\hat{\delta}_{x,\rho}$ defined in (4.43) on the right-hand side in the TWI on the lattice (4.60). It does not require renormalisation in scalar ϕ^4-theory since the derivative of a renormalised probe $\mathcal{P}$ with respect to a field ϕ cannot produce any more divergencies, and $\bar{\partial}_{\rho}\phi$ cannot do so either. However, in less simple theories the operator $\hat{\delta}_{x,\rho}$ possesses a more evolved structure and has to be renormalised. E.g. in pure Yang-Mills theory it induces a multiplicative renormalisation [28].

Finally, the renormalised TWI reads

$$a^3 \sum_{\mu} \bar{\partial}_{\mu} \langle [T_{\mu\rho}]_r(x) \mathcal{P} \rangle = -\langle \hat{\delta}_{x,\rho} \mathcal{P} \rangle + a^3 \langle Q_{\rho} \mathcal{P} \rangle, \tag{4.77}$$

where the Q_{ρ}-term vanishes in the continuum limit.

4.3 Perturbative renormalisation of the energy-momentum tensor on the lattice

As we have seen in the previous section, the EMT requires renormalisation in a regularisation scheme that breaks translation symmetry like lattice regularisation. The insertion of an operator that consists of renormalised fields and couplings into renormalised correlators can generate still new divergencies if it concerns a composite operator. To renormalise a composite operator perturbatively it is inserted into n-point functions, and any divergence that appears is subtracted. This programme was already carried out for the continuum EMT in the second half of sec. 2.4.

The bare EMT written with renormalised fields and couplings is

$$\begin{aligned} T_{\mu\rho} = {} & \bar{\partial}_\mu \phi_R \bar{\partial}_\rho \phi_R + \delta_Z \bar{\partial}_\mu \phi_R \bar{\partial}_\rho \phi_R \\ & - \delta_{\mu\rho} \left(\frac{1}{2} \sum_\sigma \bar{\partial}_\sigma \phi_R \bar{\partial}_\sigma \phi_R + \frac{1}{2} m_R^2 \phi_R^2 + \frac{\lambda_R}{4!} \phi_R^4 \right. \\ & \left. + \frac{1}{2} \delta_Z \sum_\sigma \bar{\partial}_\sigma \phi_R \bar{\partial}_\sigma \phi_R + \frac{1}{2} \delta_m \phi_R^2 + \frac{\delta_\lambda}{4!} \phi_R^4 \right), \end{aligned} \tag{4.78}$$

where we rewrote the bare EMT in eq. (4.61) using the field, mass and coupling renormalisation defined in eq. (4.4). In order to formulate the renormalised EMT in eq. (4.76), the renormalisation constants c, c', c_2, c_3, c_4 and c_6 have to be fixed such that the insertion of the renormalised EMT into n-point functions, and in particular the TWI, is finite. The renormalisation constants contain the divergencies that appear when inserting the bare EMT into n-point functions which need to be subtracted.

Because our theory is super-renormalisable, there is only a finite number of divergent diagrams, see fig. 2.3. Specifically, there is only a finite number of divergent diagrams that include the EMT. The insertion of terms in the EMT into n-point functions can be twofold: Either the term has two fields or four fields. The terms with four fields can be inserted in any diagram instead of the interaction vertex and cannot cause a change in the superficial degree of divergence D, unless they come with a divergent factor. However, δ_λ does not carry a divergence due to

the super-renormalisability of the theory, see eq. (4.21). The terms with two fields can be inserted into any propagator so that it is split into two. Thus, they reduce D by two by adding an extra squared lattice momentum in the denominator of a loop diagram. Exceptions are the terms with derivatives as well as the term proportional to δ_m. The former add two powers to the numerator in addition to the two powers added to the denominator, so that the original degree of divergence remains unchanged. So, inserting them into the two divergent diagrams in fig. 2.3 gives again a divergence. The latter carries a divergence itself, thus causing any diagram to be divergent. Assuming that δ_Z is divergent at order λ_R^2 this is also the case for insertions of terms proportional to δ_Z. However, δ_Z, δ_m and δ_λ are defined such that they cancel potential divergencies in the full propagator or the full four-point function, respectively. Thus, they do not contribute a net divergence to the composite operator $T_{\mu\rho}$.

Fig. 4.9 depicts the diagrams that can contribute to an overall divergence of the EMT which is denoted by a hatched square. A square with two legs represents the three terms in the EMT in eq. (4.78) with two fields that can cause a net divergence, a square with four legs represents the λ_R-term. The individual diagrams will be discussed in subsequent sections. We will see that only diagrams b, c and d contribute to an overall divergence of the bare EMT.

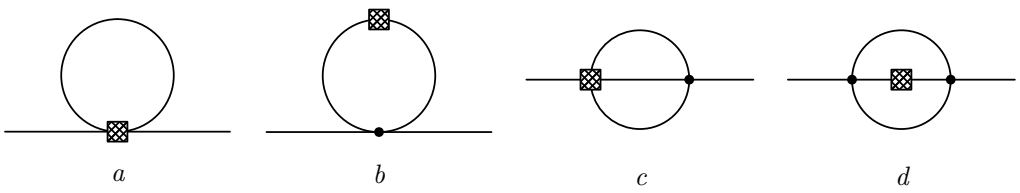

Figure 4.9 *All insertions of the EMT in n-point functions that can result in overall divergences. The insertion of the appropriate terms in the EMT is marked by a hatched square.*

4.3.1 Lattice energy-momentum tensor renormalisation at one loop

It is interesting to perform the one-loop perturbative calculation explicitly to understand the divergencies in the EMT that need to be subtracted. At order

λ_R the bare EMT written with renormalised fields and couplings is

$$T_{\mu\rho} = \bar{\partial}_\mu \phi_R \bar{\partial}_\rho \phi_R - \delta_{\mu\rho} \left(\frac{1}{2} \sum_\sigma \bar{\partial}_\sigma \phi_R \bar{\partial}_\sigma \phi_R + \frac{1}{2} m_R^2 \phi_R^2 + \frac{\lambda_R}{4!} \phi_R^4 + \frac{1}{2} \delta_m \phi_R^2 \right). \quad (4.79)$$

At this order we need to consider diagrams a and b as divergence-producing candidates. Diagram a includes only the interaction term in the EMT. Following from the general discussion, terms with two derivatives do not change the degree of divergence of a loop diagram so that both terms with derivatives in eq. (4.79) contribute a divergence and make up the hatched square in diagram b. The mass term however reduces D by two rendering diagram b convergent.

Up to order λ_R only diagram b contains a significant divergent contribution as the divergence in diagram a cancels with the mass counterterm. The expression for diagram a is precisely the one of the tadpole diagram in eq. (4.11), which in turn is used to define the mass counterterm in the same equation.

Diagram b includes the terms with two fields and two derivatives in the EMT. In order to find the explicit expression, we first need the insertion of the derivative terms at order λ_R^0,

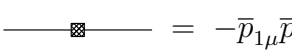

$$= -\overline{p}_{1\mu}\overline{p}_{2\rho} - \overline{p}_{2\mu}\overline{p}_{1\rho} + \delta_{\mu\rho} \sum_\sigma \overline{p}_{1\sigma}\overline{p}_{2\sigma}, \quad (4.80)$$

where p_1, p_2 are the ingoing external momenta. Using the above result, we find for the insertion of the derivative terms in the EMT into the one-loop diagram,

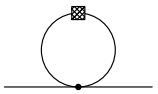

$$= -\lambda_R \int_k \frac{\overline{k}_\mu (\overline{k+q})_\rho - \frac{1}{2}\delta_{\mu\rho} \sum_\sigma \overline{k}_\sigma (\overline{k+q})_\sigma}{(\hat{k}^2 + m^2)(\widehat{(k+q)}^2 + m^2)} \quad (4.81)$$

$$= -\frac{\lambda_R}{a} \int_{-\pi}^{\pi} \frac{d^3k}{(2\pi)^3} \frac{\overline{k}_\mu (\overline{k+aq})_\rho - \frac{1}{2}\delta_{\mu\rho} \sum_\sigma \overline{k}_\sigma (\overline{k+aq})_\sigma}{(\hat{k}^2 + a^2m^2)(\widehat{(k+aq)}^2 + a^2m^2)}, \quad (4.82)$$

where k is the loop momentum and q is the momentum of the EMT. In the second line we send $k \to ka$ so that it becomes clear that the loop integral is linearly divergent. Eqs. (4.80, 4.81) are derived in app. D.

We are now able to send $a \to 0$ in the integrand in eq. (4.82). The integral multiplying the divergence in eq. (4.82) is ultraviolet-finite since the range of integration $[-\pi, \pi]$ is finite. It is also infrared finite which can be seen by power counting. We can now Taylor expand in the external momentum q. Every derivative with respect to q pulls out a factor a which increases the overall degree of divergence of the integral. The first order term in the Taylor expansion is odd, the second order is finite. Hence, the divergence is only in the zeroth order term in the Taylor expansion. Evaluating the integral yields

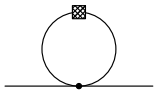

$$= -\frac{\lambda_R}{a} \int_{-\pi}^{\pi} \frac{d^3k}{(2\pi)^3} \frac{\overline{k}_\mu \overline{k}_\rho - \frac{1}{2}\delta_{\mu\rho}\overline{k}^2}{(\hat{k}^2)^2} \tag{4.83}$$

$$= -\frac{\lambda_R}{a} \left(\frac{1}{3} - \frac{1}{2}\right) \delta_{\mu\rho} \int_{-\pi}^{\pi} \frac{d^3k}{(2\pi)^3} \frac{\overline{k}^2}{(\hat{k}^2)^2} \tag{4.84}$$

$$= \frac{1}{a}\frac{\lambda_R}{6}\delta_{\mu\rho} Z_1, \tag{4.85}$$

where we used in the second line $\int k_\mu k_\rho = \frac{1}{d}\delta_{\mu\rho} \int k^2$ and Z_1 is

$$Z_1 = \int_{-\pi}^{\pi} \frac{d^3k}{(2\pi)^3} \frac{\bar{k}^2}{(\hat{k}^2)^2} \tag{4.86}$$

$$= 0.129096... \, . \tag{4.87}$$

Clearly this divergence is proportional to the operator ϕ^2 as there are no external momenta present.

Hence, the divergencies in the EMT at one-loop order are canceled by defining the renormalised EMT as

$$[T_{\mu\rho}] = \bar{\partial}_\mu \phi_R \bar{\partial}_\rho \phi_R - \delta_{\mu\rho} \left(\frac{1}{2} \sum_\sigma \bar{\partial}_\sigma \phi_R \bar{\partial}_\sigma \phi_R + \left(\frac{m_R^2}{2} + \frac{\delta_m}{2} + \frac{\lambda_R}{a}\frac{Z_1}{12} \right) \phi_R^2 + \frac{\lambda_R}{4!}\phi_R^4 \right). \tag{4.88}$$

Writing eq. (4.76) in terms of renormalised fields and couplings and absorbing all factors into the renormalisation constants,

$$[T_{\mu\rho}]_r = c\,\bar{\partial}_\mu\phi_R\bar{\partial}_\rho\phi_R + \delta_{\mu\rho}\left(c'\sum_\sigma(\bar{\partial}_\sigma\phi_R)^2 + c_2\phi_R^2 + c_3(\bar{\partial}_\mu\phi_R)^2 + c_4\phi_R^4 + c_6\phi_R^6\right), \tag{4.89}$$

we find the renormalisation constants up to order λ_R by comparing eqs. (4.88) and (4.89),

$$\begin{aligned} c &= 1 \\ c' &= -\frac{1}{2} \\ c_2 &= -\frac{m_R^2}{2} - \frac{\delta_m}{2} - \frac{\lambda_R}{a}\frac{Z_1}{12} \\ c_3 &= 0 \\ c_4 &= -\frac{\lambda_R}{4!} \\ c_6 &= 0. \end{aligned} \tag{4.90}$$

4.3.2 Lattice energy-momentum tensor renormalisation to all orders

The divergencies in diagrams c and d occur at order λ_R^2. They are all logarithmic and proportional to ϕ^2 as well, as one can see by Taylor expanding. The Taylor series approach was mentioned in the second half of sec. 2.4 and is discussed in detail in app. A.4 in the continuum. We can transfer the argument directly to the lattice as the divergent structure of the diagrams does not depend on the chosen cutoff. Thus, the insertion of the EMT into n-point functions produces only divergencies that are proportional to ϕ^2, in the continuum as well as on the lattice. Due to the super-renormalisability of the theory divergencies are only created up to order λ_R^2. Hence, we expect that the coefficients c, c', c_3, c_4, c_6 assume the values in eqs. (4.90), and c_2 will receive one more correction of order λ_R^2, to all orders in perturbation theory.

4.4 Lattice translation Ward identity along the flow

As discussed in sec. 3.2 we would like to use the gradient flow to compute the EMT, in particular on the lattice. The gradient flow on the lattice goes by the name Wilson flow. The aforementioned paper on pure gauge theory [28] inlcudes the renormalisation of the EMT with the help of the Wilson flow. The idea is to use probes at positive flow time instead of probes at the boundary.

The naive discretisation of the flow equation (3.1) yields

$$\partial_t \bar{\varphi}(t,x) = \Delta \bar{\varphi}(t,x), \qquad \bar{\varphi}(t,x)|_{t=0} = \phi(x), \tag{4.91}$$

where we choose the lattice Laplacian $\Delta = \sum_\sigma \hat{\partial}_\sigma \hat{\partial}^*_\sigma$, eq. (B.11). The solution of the lattice flow equation can be computed directly, compare with eq. (3.4),

$$\bar{\varphi}_t(x) = \sum_y \int_p e^{ip(x-y)} \tilde{K}_t(p^2) \phi(y). \tag{4.92}$$

The lattice EMT can be determined from the lattice equivalent of the local TWI in the continuum with probes at positive flow time, eq. (3.34),

$$\langle \sum_\mu \partial_\mu T_{\mu\rho}(x) P_T \rangle = -\langle \hat{\delta}_{x,\rho} P_T \rangle. \tag{4.93}$$

The local variation of a probe under a translation in direction $\hat{\rho}$ at positive flow time was derived in eq. (3.35) in the continuum. We also know the local variation of a probe at the boundary on the lattice, eq. (4.44). As explained before, any operator on the lattice is a function of the fields only, and not of its derivatives as derivatives turn into finite differences. A probe at positive flow time on the lattice is a function of the flow field only. Hence, the local variation of such a probe is

$$\hat{\delta}_{x,\rho} P_T = \int d^d y \frac{\partial P_T}{\partial \bar{\varphi}_T(y)} J(T,y;0,x)\ \partial_\rho \phi(x), \tag{4.94}$$

where the Jacobian is defined in eq. (3.19). We are now in the position to use the above result in the lattice TWI (4.93) and compute the coefficients in eqs. (4.90)

numerically. The procedure will be described in the following chapter in great detail.

5

Numerical computation of the energy-momentum tensor

In order to study the scalar model non-perturbatively we perform a set of Monte Carlo simulations. The field $\phi(x)$ of the lattice action (4.2) is assigned to the sites $x = (x_0, x_1, x_2)$ of a periodic cubic lattice, where $x_i \in \{0, 1, 2, \ldots, \check{L} - 1\}$. From the numerical point of view it is necessary to rescale all dimensionful quantities to their dimensionless equivalents:

$$\check{\phi} = \sqrt{a}\phi, \quad \check{m} = am, \quad \check{\lambda} = a\lambda, \quad \check{\partial}_\mu = a\partial_\mu, \tag{5.1}$$

where the inverted hat indicates dimensionless quantities and ∂_μ represents all lattice derivatives. After rescaling the action (4.2) reads

$$S(\phi) = \sum_x \left(-\sum_\mu \phi(x)\phi(x + a\hat{\mu}) + \left(3 + \frac{1}{2}m^2\right)\phi^2 + \frac{\lambda}{4!}\phi^4 \right), \tag{5.2}$$

where we omitted the inverted hat for readability. In this chapter all fields and couplings without an index are the bare, dimensionless ones. Furthermore, we applied the definition of the forward derivative and evaluated the sum over μ for the μ-independent terms.

5.1 Simulation algorithm

We simulate the scalar model using the algorithm suggested in [34], which alternates a local heat-bath algorithm and Swendsen-Wang cluster updates of the embedded Ising model. We choose local Metropolis updates instead of local heat-bath updates. Before discussing the two components of our algorithm in detail, let us first review some basic concepts of Monte Carlo simulations.

5.1.1 Monte Carlo simulation

Monte Carlo methods are based on repeated random sampling. A common application is Monte Carlo integration which approximates the integral of a function $f(x)$ in a volume V by averaging over a large sample $f(x_n)$ where the x_n are chosen randomly and according to a uniform distribution so that

$$\int dV\ f(x) \simeq \frac{V}{N} \sum_{n=1}^{N} f(x_n). \tag{5.3}$$

We can apply this method to the path integral

$$\langle A(\phi) \rangle = \frac{1}{\mathcal{Z}} \int D\phi\ A(\phi)\ e^{-S(\phi)}, \tag{5.4}$$

which can only be evaluated analytically for very small lattices. The idea is to estimate the path integral by averaging over a finite number of randomly chosen configurations. However, one has to take the Boltzmann factor e^{-S} into account which gives different weights to different configurations. The so-called importance sampling Monte Carlo method estimates the path integral by a small subset of configurations sampled according to the weight factor:

$$\langle A(\phi) \rangle \simeq \frac{1}{N} \sum_{n=1}^{N} A(\phi_n), \tag{5.5}$$

where the configurations ϕ_n are selected with a probability proportional to e^{-S}.

In practice the configurations ϕ_n are generated as a stochastic sequence that eventually leads to, and stays in, equilibrium where the probability distribution of

the configurations is given by the Boltzmann factor e^{-S}. Starting from a random configuration ϕ_0 the system is updated with transition probability $T(\phi_1|\phi_0)$ to a new configuration ϕ_1 which is then the starting point for the next update to ϕ_2 and so forth. The sequence $\phi_0 \to \phi_1 \to \phi_2 \to ...$ is called a Markov chain generated by a Markov process if $T(\phi'|\phi)$ is independent of its position within the Markov chain and only depends on the configuration ϕ preceding ϕ'. We also require that the Markov chain is irreducible, aperiodic, and has positive states. Irreducibility ensures that all configurations can be reached during the same Markov process. Aperiodicity adds that the probability of the same configuration to appear again is nonzero. A positive state possesses a finite mean recurrence time. Under these circumstances the system always attains the unique equilibrium distribution independent of the starting configuration and stays in equilibrium [11]. The continuance in equilibrium is expressed by the balance equation

$$\sum_{\phi} T(\phi'|\phi)P(\phi) = \sum_{\phi} T(\phi|\phi')P(\phi'), \tag{5.6}$$

where $P(\phi) \propto e^{-S(\phi)}$ is the probability that the system is in configuration ϕ. The balance equation states that the probability of entering a configuration ϕ' is the same as leaving ϕ'. Before taking any measurements there has to be a sufficiently large number of updates until the equilibrium is reached.

When computing an observable one uses a finite number of measurements N. The sample average of an observable A of uncorrelated measurements is

$$\bar{A} = \frac{1}{N}\sum_{n=1}^{N} A(\phi_n). \tag{5.7}$$

The fluctuations of the sample average are described by the variance

$$\sigma_{\bar{A}}^2 = \frac{1}{N-1}\left(\overline{A^2} - \bar{A}^2\right), \tag{5.8}$$

so that the expectation value $\langle A \rangle$ lies in the range $\bar{A} \pm \sigma_{\bar{A}}$ with a probability of approximately 68%. However, configurations generated in a sequence are not independent but correlated. This is captured by the autocorrelation function

$$C_A(A_n, A_{n+t}) = \langle A_n A_{n+t} \rangle - \langle A_n \rangle \langle A_{n+t} \rangle, \tag{5.9}$$

where t is the computer time separation between two measurements. $C_A(A_n, A_{n+t})$ equals $C_A(t)$ for a Markov chain in equilibrium since correlations only depend on the separation t but not on the location in the Markov chain. The variance of the correlated configurations is

$$\sigma_{\bar{A}}^2 = \left\langle \left(\frac{1}{N} \sum_{n=1}^{N} (A_n - \langle A \rangle) \right)^2 \right\rangle \tag{5.10}$$

$$\simeq \frac{C_A(0)}{N} \, 2\, \tau_{\mathrm{int},A}, \tag{5.11}$$

where the second line holds for large N. $\tau_{\mathrm{int},A}$ is the integrated autocorrelation time of observable A [35],

$$\tau_{\mathrm{int},A} = \frac{1}{2} + \sum_{t=1}^{N} \frac{C_A(t)}{C_A(0)}. \tag{5.12}$$

Eqs. (5.9, 5.10) are formally defined; they have to be approximated according to eq. (5.5) in Monte Carlo simulations. If the measurements are uncorrelated the autocorrelation time becomes 1/2. For correlated configurations, the number of independent configurations is $N/2\tau_{\mathrm{int},A}$ which can be seen by comparing eqs. (5.8, 5.11). This means that one has to skip about $2\tau_{\mathrm{int},A}$ configurations between measurements.

As discussed in sec. 4.1.3 when taking the continuum limit one approaches a fixed point where the correlation length diverges, which is the ultraviolet GFP in our case. Because

$$\tau_{\mathrm{int},A} \propto \xi^z \tag{5.13}$$

the autocorrelation time diverges as well. Usually the dynamical critical exponent is $z \simeq 2$ for local updating algorithms. For finite lattices $\xi \leq L$ so that near the ultraviolet fixed point $\tau_{\mathrm{int},A} \propto L^z$. The accelerated increase in the autocorrelation time is called critical slowing down as one has to skip more and more configurations in order to reach equilibrium and to have independent measurements when nearing the fixed point. A review of critical slowing down and some methods to soften or eliminate it can be found in [36].

In the following sections the two components of our simulation, Metropolis algorithm and Swendsen-Wang cluster algorithm, will be described in detail.

5.1.2 Metropolis algorithm

A sufficient condition for the balance equation (5.6) to hold is to hold term-wise. The detailed balance condition,

$$T(\phi'|\phi)P(\phi) = T(\phi|\phi')P(\phi'), \tag{5.14}$$

is used by the Metropolis algorithm [37] and most other algorithms. The Metropolis algorithm obeys the following procedure: Firstly, select a probability distribution $T_0(\phi'|\phi)$ for changing the system from configuration ϕ to ϕ'. Secondly, accept the new configuration according to the acceptance probability

$$T_A(\phi'|\phi) = \min\left(1, \frac{T_0(\phi|\phi')e^{-S(\phi')}}{T_0(\phi'|\phi)e^{-S(\phi)}}\right). \tag{5.15}$$

The total transition probability $T = T_0 T_A$ fulfils detailed balance (5.14). If the selection probability is symmetric, $T_0(\phi|\phi') = T_0(\phi'|\phi)$,

$$T_A(\phi'|\phi) = \min\left(1, e^{-\Delta S}\right), \qquad \Delta S = S(\phi') - S(\phi). \tag{5.16}$$

The suggested new configuration is definitely accepted if $\Delta S < 0$, i.e. if the action decreases. If $\Delta S > 0$ the action increases and the new configuration is only accepted with probability $e^{-\Delta S}$. If the suggested change is not accepted the old configuration is added again to the Markov chain.

In our Metropolis algorithm the lattice sites are visited successively where the field at each site is updated with uniform T_0 in the process:

$$\phi' = \phi + (1 - 2r)\delta. \tag{5.17}$$

r is a pseudo-random number uniformly distributed in the interval $[0, 1)$. We use Lüscher's RANLUX [38] to generate random numbers. The new field lies in the interval $\phi' \in (\phi - \delta, \phi + \delta]$. We choose $\delta = 0.25$ so that the acceptance rate is just above 80%. A larger or smaller value of δ would lead to a smaller or larger acceptance rate, respectively. On the one hand, a large width of the interval for ϕ' allows for bigger changes of the system so that the autocorrelation time is decreased. But a smaller acceptance rate means that the system does not change for more steps in the Markov chain which can in turn lead to an increase in the

autocorrelation time. On the other hand, a small δ changes the system to a lesser extent and the acceptance rate is higher, but also the autocorrelation time is increased. It is thus a fine balance between making changes to the system large enough to move between sufficiently different configurations but not too large so that the suggested change is never accepted. In practice, we run the simulation several times for different values of δ keeping track of the acceptance rate until the desired rate is reached. An acceptance rate of about 80% is an empirical value that works well in most cases. Note that the acceptance rate is independent of the lattice size because only single fields are being updated.

As the change in the action is local it is sufficient to calculate the difference in the Lagrangian $\Delta\mathcal{L} = \mathcal{L}(\phi') - \mathcal{L}(\phi)$ at each step. The sum over μ in the action has to be replaced with a sum over all nearest neighbours now that the sum over x is absent in the Lagrangian. If $e^{-\Delta\mathcal{L}}$ is greater than one, i.e. the action decreases, the new value for the field is accepted. If $e^{-\Delta\mathcal{L}}$ is smaller than one, it is tested against a random variable r uniformly distributed between zero and one. If $e^{-\Delta\mathcal{L}} > r$, the new value for the field is again accepted. But if $e^{-\Delta\mathcal{L}} < r$ the original value is kept. Using the random variable in this way mimics quantum fluctuations as configurations with increased action are accepted at times. To summarise, the procedure is the following:

1. Update one field according to eq. (5.17)
2. Compute $\Delta\mathcal{L}$
   If $e^{-\Delta\mathcal{L}} > 1$, accept the change
   If $e^{-\Delta\mathcal{L}} < 1$ and $e^{-\Delta\mathcal{L}} > r$, accept the change
   If $e^{-\Delta\mathcal{L}} < 1$ and $e^{-\Delta\mathcal{L}} < r$, revert the change
3. Move on to the next lattice site and return to 1.

5.1.3 Swendsen-Wang cluster algorithm

Swendsen's and Wang's cluster algorithm was the first non-local algorithm for Monte Carlo simulations, introduced for the Potts model [39]. It is based on Fortuin's and Kasteleyn's observation that it is possible to map the Potts model onto a percolation model [40, 41]. The idea is to avoid critical slowing down of local algorithms near a phase transition by defining non-local variables that

create changes in the system on a large scale. This is implemented by replacing each pair of interacting spins σ_i, σ_j by a bond with bond creation probability

$$p_{i,j} = 1 - e^{-K\delta_{\sigma_i\sigma_j}}, \tag{5.18}$$

where K is the coupling between the spins. If the spins have the same value a bond is created with the above probability which grows with increasing K. No bond is created if the values of the spins are different. In this way clusters develop. The concrete form of eq. (5.18) guarantees that equilibrium is reached and sustained [39]. All spins in each of the clusters have the same value. The clusters can be of varying size ranging from single-site clusters to clusters covering the entire width of the lattice. Note that former geometrical clusters of like spins are split into smaller ones. Once all clusters are formed the spins in each cluster are flipped with a certain probability. The new spin configuration can differ much from the preceding one as numerous spins can be changed in a single step. Then the bond creation begins afresh. A more efficient algorithm is the variation proposed by Wolff in [42] where only a single cluster is built starting from a random lattice site.

According to [34] we can define an embedded Ising model in our continuous field theory by introducing discrete variables $s(x)$ via

$$\phi(x) = s(x)|\phi(x)|. \tag{5.19}$$

The action (5.2) written in terms of these new variables defines at fixed values $|\phi(x)|$ an embedded Ising model with nearest-neighbour coupling

$$\beta_{x,x'} = |\phi(x)||\phi(x')|, \tag{5.20}$$

where $x' = x + a\hat{\mu}$. The embedded Ising model can now be updated using the Swendsen-Wang cluster algorithm. As described before one needs to identify the bonds between all lattice sites. The probability to create a bond is

$$p_{x,x'} = 1 - e^{-\beta_{x,x'}(1+s(x)s(x'))} = 1 - e^{-(|\phi(x)||\phi(x')|+\phi(x)\phi(x'))}. \tag{5.21}$$

Creating the bonds and identifying the growing clusters is realised simultaneously. The lattice sites are visited consecutively and bonds are placed with $p_{x,x'}$ between

nearest neighbours for positive $\hat{\mu}$. Then the same cluster number is assigned to sites that form a bond. If a bond is created between two sites with different cluster numbers the cluster number of the cluster with more sites is given to the combined cluster. After all clusters are formed and identified they are flipped with 50% probability, apart from single-site clusters. To summarise,

1. Choose two neighbouring lattice sites
2. Create bond with probability (5.21) and assign cluster number if applicable
3. Choose the next nearest neighbour pair and return to 2.
4. Flip clusters with 50% probability once every pair was considered

5.1.4 Simulation

The simulation is structured as follows:

1. Initialisation
2. Equilibration: loop over
    1. Swendsen-Wang cluster sweeps
    2. Metropolis sweeps
3. Measurement: loop over
    1. Swendsen-Wang cluster sweeps
    2. Metropolis sweeps
    3. Measurement

We use periodic boundary conditions. The initial field configuration ϕ_0 is chosen as either cold or hot,

$$\text{cold start} \qquad \phi_0 = 0.5 \tag{5.22}$$

$$\text{hot start} \qquad \phi_0 = 100r, \tag{5.23}$$

where r is again a pseudo-random number uniformly distributed in the interval $[0, 1)$.

We alternate Metropolis sweeps and cluster sweeps with a ratio between two and twenty, depending on how close to the phase transition we simulate. One update step consists of C cluster sweeps and M Metropolis sweeps, where there are M/C Metropolis sweeps per cluster sweep. The simulation time is e.g. about 8 hours for 33000 measurements on an 8^3 lattice run on one core of an Intel Xeon E5620 at 2.4 GHz. Tab. 5.1 collects as an example the average generation time of a configuration, the acceptance rates and the total simulation time for a simulation on an 16^3 lattice with $\lambda = 2$ for 40 cluster sweeps, 200 Metropolis sweeps, 1000 equilibration steps, and 1000 measurements. The acceptance rates are defined as the ratio of accepted field updates or created bonds to the total number of lattice sites or links. The masses are selected close to and on both sides of the line of constant physics $\rho = 5$, see tab. 5.7.

m	0.26	0.27	0.28	0.29	0.30
$\bar{t}/s$	0.23434(7)	0.233921(8)	0.234009(8)	0.23441(3)	0.302(2)
MAR	0.877380(8)	0.877422(8)	0.877467(8)	0.877518(8)	0.877557(8)
CAR	0.16076(3)	0.16140(4)	0.16267(4)	0.16370(4)	0.16497(4)
T/s	469	469	469	469	578

Table 5.1 *Average simulation time $\bar{t}$, Metropolis acceptance rate (MAR), cluster acceptance rate (CAR), and total simulation time T for simulating at $L = 16$, $\lambda = 2$, 40 cluster sweeps, 200 Metropolis sweeps, 1000 equilibration steps, and 1000 measurements for different values of the mass.*

As discussed earlier, this two-part algorithm is very effective in reducing the dynamical critical exponent z near the phase transition where the correlation length ξ diverges. The authors in [34] found $z = 0.07 \pm 0.07$ in one, $z = 0.29 \pm 0.09$ in two, and $z = 0.87 \pm 0.20$ in three dimensions, respectively. We monitored the integrated autocorrelation time (5.12) for every set of simulations and found it to be indeed negligible. In our simulations $\tau_{\mathrm{int},A} = \tau_{\mathrm{int}}(A)$ does not depend on any of our local observables A, and is independent of the lattice size and the value of the flow time. Tab. 5.2 lists the integrated autocorrelation times of the correlation functions in the TWI (5.38), see also eq. (5.40), for probe $j = 9$, see tab. 5.9, distance $|x - y| = 0$, and two different lattice sizes and flow times. τ_{int} is always one half which characterises independent measurements, compare with eq. (5.12).

L	$c(t)$	$\tau_{\text{int}}(V^{(9)})$	$\tau_{\text{int}}(M^{(9,1)})$	$\tau_{\text{int}}(M^{(9,2)})$	$\tau_{\text{int}}(M^{(9,3)})$	$\tau_{\text{int}}(M^{(9,4)})$
16	0.416	0.5(1)	0.5(1)	0.5(1)	0.5(1)	0.5(1)
	0.589	0.5(1)	0.5(1)	0.5(1)	0.5(1)	0.5(1)
32	0.416	0.6(2)	0.5(2)	0.5(2)	0.5(2)	0.5(2)
	0.589	0.5(1)	0.5(2)	0.5(2)	0.5(2)	0.5(2)

Table 5.2 *Integrated autocorrelation times τ_{int} for $L = 16, 32$ and two different flow times for the correlation functions in the TWI (5.38), see also eq. (5.40), for probe $j = 9$ and $|x - y| = 0$, see tab. (5.9).*

5.2 Phase diagram

As discussed in sec. 2.3 in $2 \leq d < 4$ there are two fixed points of the renormalisation group flow, the ultraviolet GFP and the infrared Wilson-Fisher fixed point. In the plane of relevant parameters there is a line of second order phase transitions connecting the two fixed points. We locate the phase transition in parameter space by studying the peak of the susceptibility χ, defined as

$$\chi = L^{-3} \left(\left\langle \left(\sum_x \phi(x) \right)^2 \right\rangle - \left\langle \left| \sum_x \phi(x) \right| \right\rangle^2 \right). \tag{5.24}$$

The position of the peak is found by performing many simulations at fixed λ and different values of m. The data around the peak of χ were reweighted to further values of m using the multi-histogram method first proposed in [43]. The multi-histogram method is based on finding the best estimate of the density of states. It incorporates several measurements of the same quantity at different couplings, thus being valid over a wide range of the couplings. It is then possible to interpolate the quantity in question for a coupling that lies in between the ones used in the measurements by combining the estimates of the observable from the measurements at different couplings. The expectation value of an observable A at coupling β can be estimated by

$$\langle A \rangle_\beta = \frac{1}{\mathcal{Z}(\beta)} \sum_{i,s} \frac{A_{is}}{\sum_j n_j \mathcal{Z}_j^{-1} e^{(\beta - \beta_j) E_{is}}}. \tag{5.25}$$

The sum over i is over all simulations performed at different couplings β_i. The sum over s includes all configurations sampled during the i^{th} simulation. A_{is}

and E_{is} are the observable and the total energy of such a configuration s with coupling β_i, and n_j is the total number of measurements taken at coupling β_j. The partition function at any coupling can be calculated from

$$\mathcal{Z}(\beta) = \sum_{i,s} \frac{1}{\sum_j n_j \mathcal{Z}_j^{-1} e^{(\beta-\beta_j)E_{is}}}, \tag{5.26}$$

where the $\mathcal{Z}_j$ have to be determined iteratively beforehand from the same equation. In practice one often uses the logarithm of the partition function to avoid exceeding the numerical range of the computer since $\mathcal{Z}$ can become very large or very small. A derivation of the above equations can be found in [44]. As we are interested in the peak of the susceptibility, we need to make the replacement $A = \chi$ in eq. (5.25) and choose the values of $\beta = m$ with small increment around the area of where the peak is indicated by the susceptibilities directly determined from the measurements.

The errors of the susceptibility calculated from the measurements and on the interpolated results are computed using the bootstrap method [45]: From N measurements N are selected at random with replacement, allowing the same measurement to be chosen more than once. This is done s times so that we have s samples of N measurements. The quantity of interest A is computed for each of the s samples. Then, the best estimate of $\langle A \rangle$ and the variance are given by

$$\bar{A} = \frac{1}{s} \sum_{i=1}^{s} A_i \tag{5.27}$$

$$\sigma_{\bar{A}}^2 = \overline{A^2} - \bar{A}^2, \tag{5.28}$$

see e.g. [44, 46, 47]. Schematically,

1. Create N measurements
2. Pick N measurements from the original sample at random with replacement
3. Repeat 1. and 2. s times
4. Calculate A for each of the s resampled samples
5. Calculate $\bar{A}$ and $\sigma_{\bar{A}}^2$ according to eqs. (5.27, 5.28)

One advantage of the bootstrap method compared to e.g. the jackknife is that the measured data from which the samples are drawn do not have to be uncorrelated. Note also that σ^2 is independent of the values of N and s, however, s has to be sufficiently large, at least of order 100. Applied to calculating the susceptibility we proceed as follows. First, we measure $\sum_x \phi(x)$. Then, we randomly pick N values s times from this list of measurements and compute the susceptibility for each of the s samples. Finally, using eqs. (5.27, 5.28) we compute χ and $\sigma_{\bar{\chi}}$. We go about the reweighted data similarly. The histogram method is repeated many times with the resampled bootstrap samples. Then eqs. (5.27, 5.28) are applied to estimate the susceptibility and its error for the interpolated data.

In order to find the exact location of the peak of the susceptibility, m_{max}, the data are reweighted a second time varying m in the following fashion. First, the range of the mass is chosen such that the peak of the susceptibility lies definitely within. Then the susceptibility is calculated at five values of m at equal distances within this interval. Next, a new interval half as big as the previous one is chosen according to the location of the largest χ. This is repeated until the length of the interval is smaller than or equal to 10^{-11} so that the maximum value of the susceptibility lies within the range $m_{max} \pm 10^{-11}$. For both reweighting procedures we choose 100 samples of 100 measurements.

We define the pseudo-critical coupling $m_c(L) = m_{max}(L)$ for each value of λ as the coupling where the peak of the susceptibility for a fixed volume is located. The finite size scaling of the pseudo-critical coupling is given by, see e.g. [48, 49],

$$m_c^2(L) = m_c^2 + m_1 L^{-1/\nu} + \ldots, \tag{5.29}$$

where m_c is the critical mass in the infinite volume limit, m_1 is a coefficient that has to be determined, ν is a critical exponent of the theory, and the dots denote subleading corrections to scaling. The results for m_c^2 are collected in tab. 5.3, and the phase diagram in the (λ, m^2)-plane is shown in fig. 5.1, where the dashed line connects the data points merely to guide the eye.

λ	m_c^2	χ_r^2
2.0	-0.2361(3)	3.63
26.5	-2.4887(5)	6.00
51.0	-4.3210(3)	1.01
75.5	-5.96747(5)	0.02
100.0	-7.4955(2)	0.16
125.0	-8.9697(2)	0.12
150.0	-10.3764(3)	0.29
175.0	-11.7297(3)	0.40
200.0	-13.0398(3)	0.26
225.0	-14.315(1)	5.10

Table 5.3 *Estimate of m_c^2 as a function of the coupling λ extrapolated to the infinite volume limit using eq. (5.29) where subleading terms were omitted. The reduced chi-square for the fits is given in the third column.*

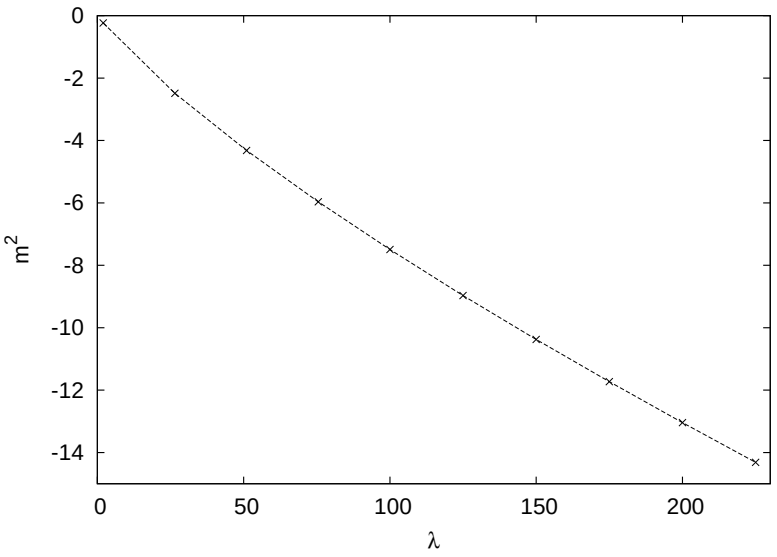

Figure 5.1 *Phase diagram of scalar ϕ^4-theory. The line of second order phase transition separates the symmetric phase (upper region) from the broken phase (lower region). The data are collected in tab. 5.3. The dashed line is drawn merely to guide the eye.*

Our estimate of the critical mass is obtained using the finite size scaling in eq. (5.29) and performing a two-parameter fit. The critical exponent was set to the best estimate $\nu = 0.6298(5)$ computed in [50]. The data were fitted with gnuplot [51] which uses the Marquardt-Levenberg algorithm [52, 53]. The algorithm relies on a weighted least-squares fit minimising the function

$$\chi^2 = \sum_{i=1}^{N} \left(\frac{f(x_i) - y_i}{\sigma_i} \right)^2 \tag{5.30}$$

iteratively with respect to parameters b_j. $f(x) = f(x, b_j)$ is a user-defined, hypothesised function of these parameters, and the y_i are the observed, normally distributed data defining N data sets $\{x_i, y_i, \sigma_i\}$, where σ_i is the standard deviation of y_i. The goal is to find the values of the parameters for which the function $f(x)$ describes the data best. A measure of the goodness of the final fit is the reduced chi-square χ^2_r defined as χ^2 divided by the number of degrees of freedom. If $f(x)$ is a good fit of the data $f(x_i)$ will coincide with the mean μ_i so that $\chi^2 \simeq N$ and thus $\chi^2_r \simeq 1$. If χ^2_r is much larger than one the model function is not a good choice. The allowed distance from one is estimated by the so-called p-value,

$$p = \int_{\chi^2}^{\infty} f(\chi^2)\, d\chi^2, \tag{5.31}$$

where the probability distribution of χ^2 is

$$f(\chi^2) = e^{-\chi^2/2}\, \frac{(\chi^2)^{n/2-1}}{2^{n/2}\Gamma\left(\frac{n}{2}\right)}. \tag{5.32}$$

$f(\chi^2)$, and hence p depend on the number of degrees of freedom n. The p-value advises about the probability of observing another sample of data as extreme as the test data. A $\chi^2_r > 1$ with a corresponding p-value falling below a chosen significance level is a sign that the fitting function is describing the data inaccurately. For an overview of statistical methods see e.g. [54].

We can assume that our measurements of $m_c^2(L)$ are normally distributed so that we can use the chi-square test for goodness of fit. The fits to the infinite volume limit of m_c^2 are mediocre as χ^2_r moves within the range $[0.02, 6.00]$, see tab. 5.3. The data were generated using three or four different lattice sizes depending on the value of χ^2_r. As there are two parameters being set, $n = 1, 2$ for $L = 8, 10, 20$

and $L = 8, 10, 20, 28$ respectively. Fig. 5.2 shows the p-value for $n = 1, 2, 3$ and our chosen significance level of 0.05, revealing that χ^2_r should be smaller than 3.8 or 3 respectively. Hence, eq. (5.29) should in principle not be used to describe the data of $\lambda = 26.5, 225$. In addition, some of the χ^2_r are very small compared to 1. These deviations from the desired values of χ^2_r of order one are very likely to come from the small lattice sizes. There is no visible correlation between the lattice sizes and χ^2_r or the values of the coupling and χ^2_r indicating that a more thorough investigation is needed. However, the critical values of the mass given in tab. 5.3 are good enough estimates for our purpose of testing the method and to display the line of phase transition. Better fits are obtained for the critical line closer to the GFP, see tab. 5.8 in the next section. Note that $m_c^2(L)$ is linear in the parameters m_c^2 and m_1 so that the confidence limits of m_c^2 calculated by the algorithm are valid.

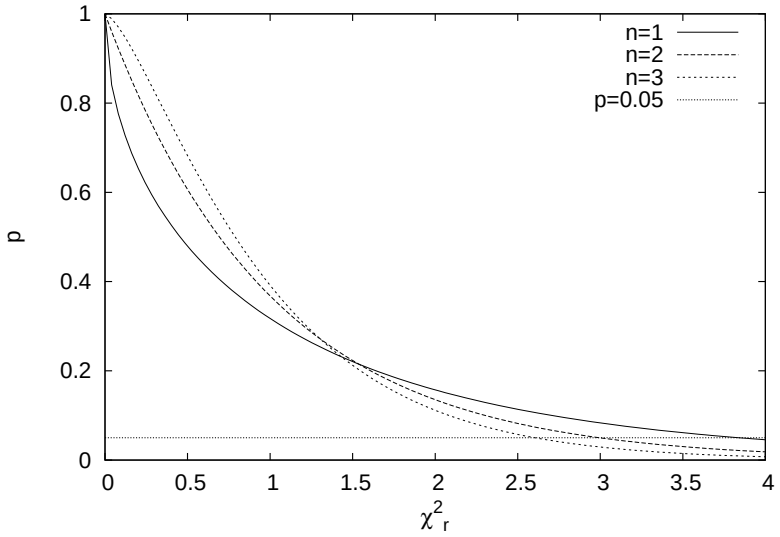

Figure 5.2 *The p-value of the χ^2 distribution defined in eq. (5.31) for $n = 1, 2, 3$.*

As an illustration of the entire procedure and of the typical features of the reweighting method and the fits, let us discuss one instance step by step. Fig. 5.3 summarises the measured values of the susceptibility for $\lambda = 150$ and $L = 8, 10, 20, 28$, as well as the reweighted data near the peak of the susceptibility. A close-up of the vicinity of the peak, the reweighted data and the peak of the susceptibility for the $L = 8$ volume is shown in fig. 5.4.

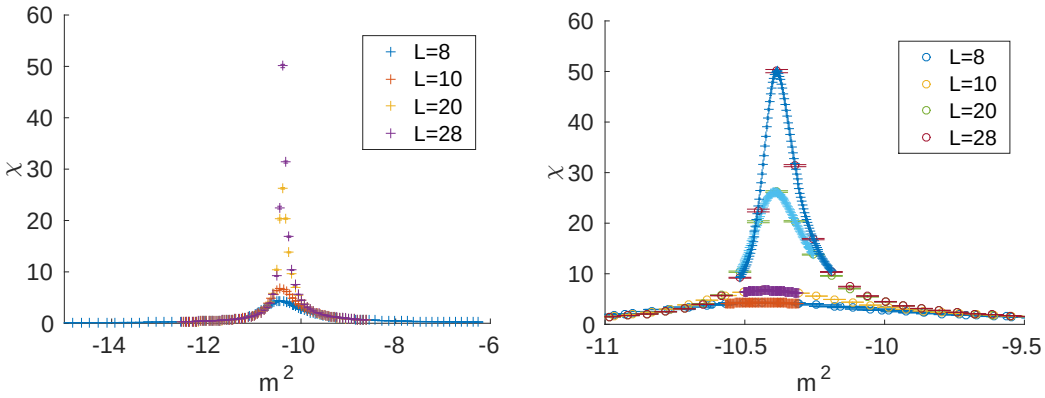

Figure 5.3 *Susceptibility for $\lambda = 150$ and $L = 8, 10, 20, 28$ around the phase transition (left) including reweighted data near the peak of the susceptibility (right).*

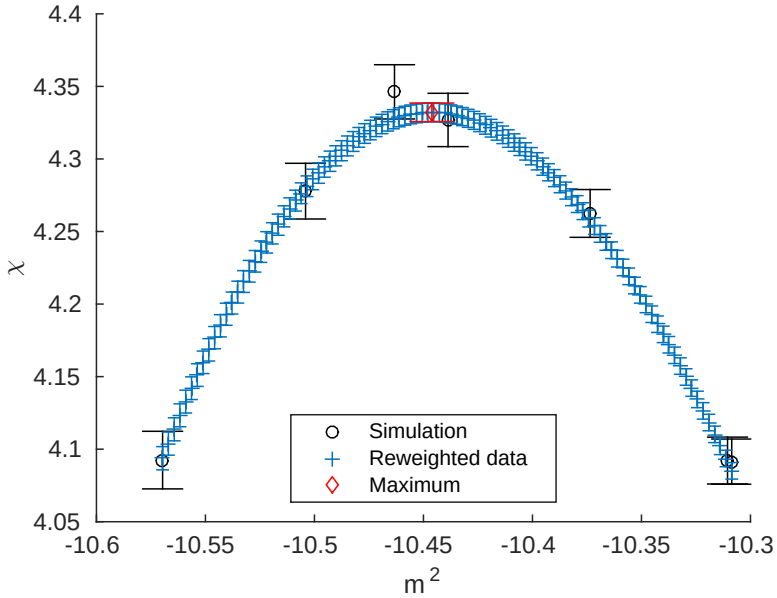

Figure 5.4 *Determination of the peak of the susceptibility for $\lambda = 150$ and $L = 8$ using reweighting.*

The peak of the susceptibility is predicted to scale with the volume as $L^{2-\eta}$ up to subleading corrections [49], where $\eta = 0.0366(8)$ is the anomalous dimension computed in [50]. The rescaled susceptibilities for two values of the volume, $L = 8$ and $L = 28$, are shown in fig. 5.5. The maximum of the rescaled peak region is independent of L while the position of the maximum is shifted according to eq. (5.29). Tab. 5.4 collects the values and locations of the peaks for $L = 8$ and $L = 28$, as well as the rescaled values of the peaks. The plots and maximum values are consistent with the expected scaling, suggesting that a finite-size fit does indeed yield a robust estimate of the critical coupling.

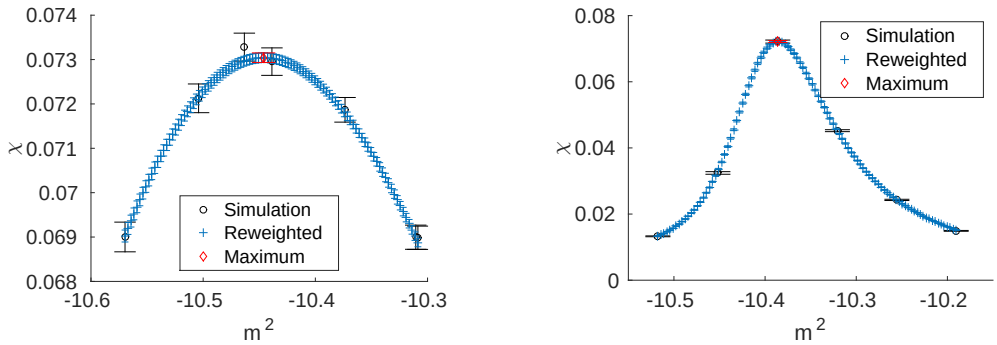

Figure 5.5 *Rescaled values of the susceptibility at $\lambda = 150$ for $L = 8$ (left) and $L = 28$ (right).*

L	$m_c(L)^2$	$\chi_{max}(L)$	$\chi_{max}(L) * L^{\eta-2}$
8	-10.446(1)	4.332(6)	0.0730(1)
28	-10.3860(5)	50.1(2)	0.0722(3)

Table 5.4 *Location and peak of the susceptibility, and rescaled values of the peaks at $\lambda = 150$ for $L = 8$ and $L = 28$.*

So finally, the value of m_c^2 is extrapolated to the infinite volume limit using eq. (5.29), where subleading terms are omitted. As a result we have a two-parameter fit shown in fig. 5.6 for $\lambda = 150$. The values for the parameters are $m_1 = -1.88(2)$, and the critical mass in the infinite volume limit is $m_c^2 = -10.3764(3)$.

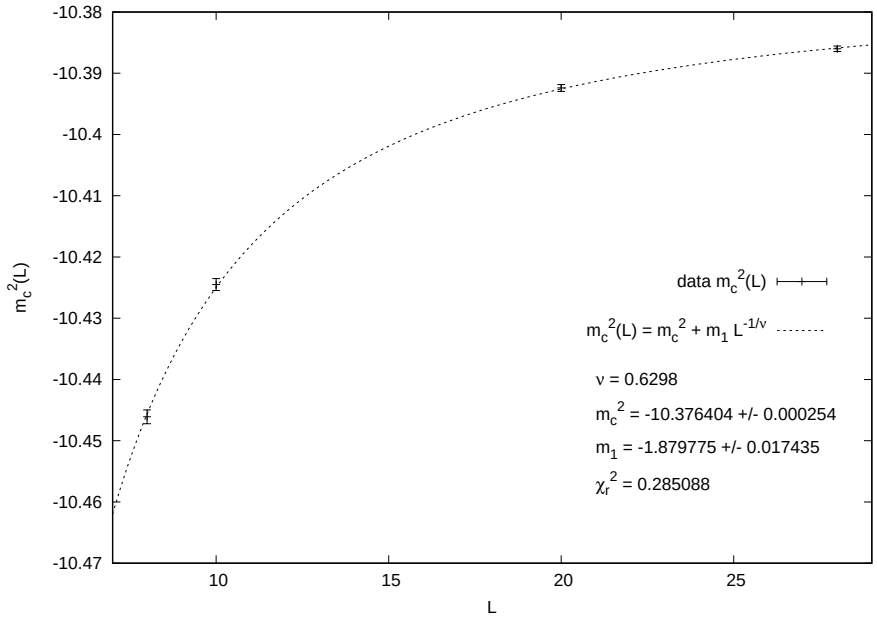

Figure 5.6 *Finite-size extrapolation of the critical mass for $\lambda = 150$ using a two-parameter fit. The functional form is fixed by neglecting all subleading corrections in eq. (5.29).*

5.3 Lines of constant physics

As described in sec. 4.1.3 the continuum limit is approached by following lines of constant physics towards the ultraviolet fixed point. We need to specify two dimensionful parameters to determine our theory since there are two relevant operators close to the GFP. The continuum limit is approached when these parameters are small compared to the ultraviolet cutoff. We choose m_R and λ. The latter can be used instead of the renormalised quartic coupling as λ undergoes only a finite multiplicative renormalisation, see eq. (4.22). We define the ratio (4.26),

$$\rho = \frac{\lambda}{m_R}, \tag{5.33}$$

to label lines of constant physics and hence to distinguish different theories.

The renormalised mass is defined by the renormalisation condition (4.8) and can be computed non-perturbatively as

$$m_R^2 = \frac{p^2 \langle |\tilde{\phi}(p)|^2 \rangle}{\langle |\tilde{\phi}(0)|^2 \rangle - \langle |\tilde{\phi}(p)|^2 \rangle}, \tag{5.34}$$

where $p = (2\pi, 0, 0)$ is the smallest non-zero momentum, and $\tilde{\phi}$ is the Fourier transform of the fundamental field variables. It is easy to see that the right-hand side equals m_R^2 to leading order when inserting the free propagator.

In order to find lines of constant physics we proceed as follows. The lattice spacing is set using the bare coupling λ. In addition, we keep the physical volume constant leading to the relation $L = \alpha/\lambda$, where α is a proportionality factor. We then select a value for m_R and one for ρ. The renormalised mass is chosen so that $2/L \ll m_R \ll 1$ to avoid finite volume effects as well as effects from lattice artefacts, see also sec. 4.1.3. Lines of constant physics along which the lattice spacing varies are then defined by changing λ while keeping the physical volume constant, and the value of the bare mass is adjusted such that ρ remains unaffected.

Schematically,

1. Choose $2/L \ll m_R \ll 1$, ρ, and calculate λ
2. Choose a value for $L\lambda$ that stays constant
3. Scan the parameter space along direction m until m_R is found
4. Change L which implies an indirect proportional change in λ
5. Return to 3.

We identify four trajectories in the symmetric phase corresponding to $\rho = 1.5, 3, 5, 10$. We set the renormalised mass for $\rho = 10$, $L = 8$ to $m_R = 0.45$ keeping it fixed at this value for $L = 8$ for all other ρ. Combined with the condition $L = \alpha/\lambda$ this defines both m_R and λ for all values of ρ and all volumes. A selection of these numbers is displayed in tab. 5.5.

L	m_R	$\lambda(\rho = 10)$	$\lambda(\rho = 5)$	$\lambda(\rho = 3)$	$\lambda(\rho = 1.5)$
8	0.45	4.5	2.25	1.35	0.675
16	0.225	2.25	1.125	0.675	0.3375
32	0.1125	1.125	0.5625	0.3375	0.16875

Table 5.5 *Selection of values of m_R and λ for different ρ and L for $m_R(\rho = 10, L = 8)$ fixed to 0.45.*

The values of the renormalised mass are the ones we are looking for. They are determined by simulating over a range of m and calculating m_R for all these m. The range of m is then narrowed several times until the desired precision for m_R is reached.

The lines of constant physics are plotted in fig. 5.7, and the values of λ, m^2 and L are reported in tabs. 5.6 and 5.7. Some of the data are from early runs that do not exist anymore so that we cannot report the error.

The only source of statistical error in this strategy is the determination of the renormalised mass m_R which can be computed with high precision. In our simulation the relative error of m_R is smaller than 1%. The error on the bare mass depends on the step size of the scan which in turn depends on the error on the renormalised mass.

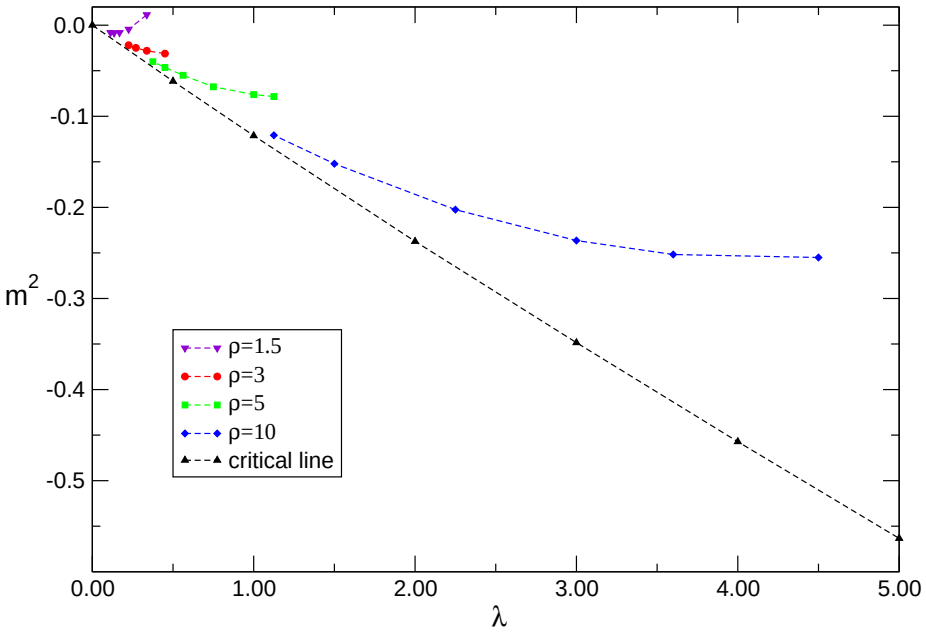

Figure 5.7 *Lines of constant physics for $\rho = 1.5, 3, 5, 10$, and the critical line. The dashed lines are merely there to guide the eye.*

$\rho = 1.5$			$\rho = 3$		
λ	m^2	L	λ	m^2	L
0.3375	$+0.011(1)$	16	0.45	$-0.0282(3)$	24
0.225	$-0.0019(3)$	24	0.3375	$-0.0281(2)$	32
0.16875	$-0.0081(2)$	32	0.27	$-0.0248(2)$	40
0.135	$-0.00837(9)$	40	0.225	$-0.0219(1)$	48
0.1125	$-0.0081(2)$	48			

Table 5.6 *Values of the couplings λ and m^2 for $\rho = 1.5, 3$.*

$\rho = 5$			$\rho = 10$		
λ	m^2	L	λ	m^2	L
1.125	$-0.0784(6)$	16	4.5	$-0.251(8)$	8
1.0	-0.076176	18	3.6	-0.2517	10
0.75	$-0.063(5)$	24	3.0	-0.2364	12
0.5625	$-0.0550(1)$	32	2.25	$-0.2025(9)$	16
0.45	$-0.04640(9)$	40	1.5	-0.1521	24
0.375	$-0.04(4)$	48	1.125	-0.120843	32

Table 5.7 *Values of the couplings λ and m^2 for $\rho = 5, 10$.*

Fig. 5.7 also presents the critical line. Our estimate of the critical mass is again obtained using the finite size scaling in eq. (5.29). Tab. 5.8 stores the concrete values of m_c^2 as well as the reduced chi-square. All fits to the infinite volume limit of m_c^2 are of good quality. They are performed using five, four or three different lattice sizes corresponding to three, two or one number of degrees of freedom n for a two-parameter fit, respectively. The lattice sizes are selected from $L = 5, 10, 20, 25, 30$ such that fewer lattices means discarding the smallest lattice sizes. Consulting the p-value in fig. 5.2, the reduced chi-square should be smaller than 3.9,3,2.6 for $n = 1, 2, 3$ respectively. This condition is fulfilled by all χ_r^2 in tab. 5.8.

λ	m_c^2	χ_r^2
0.5	-0.06151(9)	1.76
1	-0.1213(2)	2.02
2	-0.2373(5)	2.73
3	-0.3485(3)	1.27
4	-0.4572(3)	1.78
5	-0.5633(5)	2.74

Table 5.8 *Estimate of m_c^2 as a function of the coupling λ close to the GFP. The reduced chi-square for the fits is given in the third column. The data are extrapolated to the infinite volume limit using eq. (5.29) where subleading terms were omitted.*

The numerical data presented in fig. 5.7 and tabs. 5.6-5.8 were already compared to the perturbatively found lines of constant physics and the critical line in sec. 4.1.5.

5.4 Renormalisation constants of the lattice energy-momentum tensor

Having understood the perturbative renormalisation of the EMT to all orders, see sec. 4.3, as well as how to use the Wilson flow, see chap. 3, and having built an operational simulation algorithm for scalar ϕ^4-theory, we can finally turn to the numerical determination of the renormalisation constants of the EMT. In the following two sections we discuss the general strategy for computing the renormalisation constants in detail and present our results.

5.4.1 General strategy and preparation

Using all-order perturbative arguments in sec. 4.3 and in particular eqs. (4.89, 4.90) we are able to write the most general form the renormalised EMT expressed with bare fields and couplings can have,

$$[T_{\mu\rho}] = \frac{c}{2}\,\bar{\partial}_\mu\phi\bar{\partial}_\rho\phi + \delta_{\mu\rho}\left(\frac{c_3}{2}\sum_\sigma(\bar{\partial}_\sigma\phi)^2 + \frac{c_2}{2}\,\phi^2 + \frac{c_4}{4!}\,\phi^4\right). \tag{5.35}$$

Here, we rescaled the coefficients with factors of 2 and 4! compared to eq. (4.89). The fields, couplings and derivatives are dimensionless, as well as the renormalisation constants and the EMT itself. The right-hand side of the above equation can be abbreviated by

$$[T_{\mu\rho}] = \sum_i c_i T^{(i)}_{\mu\rho}, \tag{5.36}$$

The dimensionless TWI derived from eq. (4.77) reads up to order-a terms

$$\sum_\mu \bar{\partial}_\mu\langle[T_{\mu\rho}](x)\mathcal{P}\rangle = -\langle\hat{\delta}_{x,\rho}\mathcal{P}\rangle, \tag{5.37}$$

where $\mathcal{P}$ and $\hat{\delta}_{y,\rho}$ are again the dimensionless equivalents of the quantities defined in sec. 4.2.1. Using eq. (5.36) and p probes at positive flow time $P_T^{(j)}$ with $j = 1,\ldots,p$ the TWI reads

$$\sum_{\mu,i} c_i\bar{\partial}_\mu\langle T^{(i)}_{\mu\rho}(x)P_T^{(j)}\rangle = -\langle\hat{\delta}_{x,\rho}P_T^{(j)}\rangle. \tag{5.38}$$

Our strategy to compute the coefficients c_i is to select a suitable set of probes $\mathcal{P}$, insert these into the TWI, and solve for the unknown coefficients c_i. The expectation values in eq. (5.38) can be computed by means of Monte Carlo simulations. The left-hand side is a two-point correlation function of a flowed operator and an operator sitting at the boundary. The right-hand side is the variation of the probe due to a local translation at the boundary. The action of the operator $\hat{\delta}_{x,\rho}$ on a generic probe is defined in eq. (4.43). As derived in sec. 4.4 it becomes in our scalar theory for probes made of fields at positive flow time, see eq. (4.94),

$$\hat{\delta}_{x,\rho} P_T^{(j)} = \int d^d y \frac{\partial P_T^{(j)}}{\partial \bar{\varphi}_T(y)} J(T, y; 0, x)\, \partial_\rho \phi(x), \tag{5.39}$$

The Jacobian $J(T, y; 0, x)$ is defined in eq. (3.19) where the integral is replaced by a finite sum on the lattice.

The Wilson flow needed to evaluate the flow fields appearing in eq. (5.38) can be solved exactly, see sec. 4.4. However, this is not efficient as the sums in eq. (4.92) are very expensive to evaluate. Instead, we implement as a numerical integration routine the fourth-order Runge-Kutta method. For the fourth-order method the total accumulated error is of order $\mathcal{O}(dt^4)$, where dt is the flow time step size. Hence, the systematic error due to this approximation is very small, e.g. of order 10^{-14} for $dt = 0.0005$, and in particular orders of magnitude smaller than the statistical error we quote for the values of the renormalisation constants, see tabs. 5.13–5.16.

We are now in the position to compute the expectation values in eq. (5.38). The problem of finding the renormalisation constants can be reformulated as a linear system of equations (LSE),

$$\sum_i c_i M^{(j,i)} = -V^{(j)}, \tag{5.40}$$

where M is a matrix with i columns determined by the terms $T_{\mu\rho}^{(i)}$ in the EMT, and j rows determined by the probes $P_T^{(j)}$. $V^{(j)}$ is a vector with entries $\hat{\delta}_{x,\rho} P_T^{(j)}$. The most apparent approach to solve eq. (5.40) is to choose a square LSE with the same number of equations and unknowns, in our case four, and invert the matrix $M^{(j,i)}$. Besides selecting different probes we can also change the flow

time T and the distance between the insertion of the probes and the EMT. This seeming freedom implies a huge constraint on the LSE as eq. (5.40) has to hold in the continuum limit for any probe observable, any flow time, and any distance between the probe and the EMT. Another important point to note is that the LSE is incomplete at any finite lattice spacing since eq. (5.38) is only valid up to cutoff effects.

Probes

As discussed in sec. 4.4 the probes have non-zero flow time $T > 0$. Further, we choose probes that transform like vectors with regard to the cubic lattice symmetry. This allows us to also study the case where the EMT and the probe sit at the same point in space-time. If we use a probe without Lorentz index the expectation value will go to zero: $\langle P_T(0)T_\rho(x)\rangle = Ax_\rho \to 0$ as $x \to 0$, whereas $\langle P_{T\nu}(0)T_\rho(x)\rangle = Ax_\nu x_\rho + B\delta_{\nu\rho} \to B\delta_{\nu\rho}$ as $x \to 0$, where A and B are constants. In addition, the number of fields inside each probe has to be even to ensure non-vanishing expectation values.

The probes are chosen according to their mass dimension d_O. We use a subset of all local vectorial operators up to dimension five which are shown in tab. 5.9. All vectorial probes up to $d_O = 5$ are collected in tab. 5.10. There, they are sorted not only by their dimension but also by their derivative and field content.

d_O	Operator	Label
2	$\phi\partial_\rho\phi$	1
3	$\phi^3\partial_\rho\phi$	2
4	$\phi^5\partial_\rho\phi$	3
	$\sum_\sigma \phi\partial_\rho\partial_\sigma^2\phi$	4
	$\sum_\sigma \partial_\rho\phi\partial_\sigma^2\phi$	5
	$\sum_\sigma \partial_\sigma\phi\partial_\rho\partial_\sigma\phi$	6
5	$\phi^7\partial_\rho\phi$	7
	$\sum_\sigma \phi^3\partial_\rho\partial_\sigma^2\phi$	8
	$\sum_\sigma \phi^2\partial_\rho\phi\partial_\sigma^2\phi$	9
	$\sum_\sigma \phi^2\partial_\sigma\phi\partial_\rho\partial_\sigma\phi$	10
	$\sum_\sigma \phi\partial_\rho\phi\partial_\sigma\phi\partial_\sigma\phi$	11

Table 5.9 *Subset of all vectorial probes up to dimension $d_O = 5$ that is used in the analysis.*

d_O	Content	Operator
2	$\partial^1\phi^2$	$\phi\partial_\rho\phi$
3	$\partial^1\phi^4$	$\phi^3\partial_\rho\phi$
	$\partial^2\phi^2$	$\phi\partial_\rho^2\phi$, $\partial_\rho\phi\partial_\rho\phi$
4	$\partial^1\phi^6$	$\phi^5\partial_\rho\phi$
	$\partial^2\phi^4$	$\phi^3\partial_\rho^2\phi$, $\phi\partial_\rho\phi\partial_\rho\phi$
	$\partial^3\phi^2$	$\phi\partial_\rho^3\phi$, $\partial_\rho\phi\partial_\rho^2\phi$
		$\phi\partial_\rho\partial_\sigma^2\phi$, $\partial_\rho\phi\partial_\sigma^2\phi$, $\partial_\sigma\phi\partial_\rho\partial_\sigma\phi$
5	$\partial^1\phi^8$	$\phi^7\partial_\rho\phi$
	$\partial^2\phi^6$	$\phi^5\partial_\rho^2\phi$, $\phi^4\partial_\rho\phi\partial_\rho\phi$
	$\partial^3\phi^4$	$\phi^3\partial_\rho^3\phi$, $\phi^2\partial_\rho\phi\partial_\rho^2\phi$, $\phi\partial_\rho\phi\partial_\rho\phi\partial_\rho\phi$
		$\phi^3\partial_\rho\partial_\sigma^2\phi$, $\phi^2\partial_\rho\phi\partial_\sigma^2\phi$, $\phi^2\partial_\sigma\phi\partial_\rho\partial_\sigma\phi$, $\phi\partial_\rho\phi\partial_\sigma\phi\partial_\sigma\phi$
	$\partial^4\phi^2$	$\phi\partial_\rho^4\phi$, $\partial_\rho\phi\partial_\rho^3\phi$, $\partial_\rho^2\phi\partial_\rho^2\phi$
		$\phi\partial_\rho^2\partial_\sigma^2\phi$, $\partial_\rho\phi\partial_\rho\partial_\sigma^2\phi$, $\partial_\sigma\phi\partial_\rho^2\partial_\sigma\phi$, $\partial_\rho^2\phi\partial_\sigma^2\phi$, $\partial_\rho\partial_\sigma\phi\partial_\rho\partial_\sigma\phi$

Table 5.10 *All vectorial probes up to dimension $d_O = 5$. The index σ is summed over, the index ρ is not.*

Parameters

Our goal is to compute the expectation values in eq. (5.38) along the lines of constant physics determined in sec. 5.3. The analysis has been carried out to date for $\rho = 5$, for lattice sizes $L = 16, 18, 24, 32$, see tab. 5.7, and distances $|x - y| = 0, 1, 1.41$.

We define the ratio of the smearing radius and L,

$$c(t) = \frac{\sqrt{6t}}{L}. \tag{5.41}$$

For the analysis we choose twenty-one equidistant flow times t such that $c(t) \in [0, 0.7]$ and such that the $c(t)$ are the same for every lattice size. Considering larger values of $c(t)$ is unnecessary as the fundamental field is smeared over almost all of the lattice and the dying signal is distorted by fluctuations. Data of small values of $c(t)$ are governed by lattice artefacts and remnant effects of divergencies from contact terms where applicable.

As explained before we could potentially combine equations with different probes, distances and flow times. However, the combinatorics gives a huge number of possible combinations, plus, one has to be careful as the same probes at different flow times are correlated. But even when combining only the eleven probes in

tab. 5.9 and three distances we have to solve $\binom{33}{4} = 40920$ LSE. Hence, we decide to keep the flow time as well as the distance per LSE fixed and to distinguish the four equations just by choosing different probes. This still gives $\binom{11}{4} = 330$ LSE that have to be solved for every one of the four lattices, the three distances, and the twenty-one flow times.

To compute eq. (5.38) in practice, we used translation invariance to rewrite the left-hand side such that the derivative acts on the probe rather than on the EMT,

$$\sum_{\mu\rho} \bar{\partial}_\mu \langle T^{(i)}_{\mu\rho} P^{(j)}_{T\rho} \rangle = -\sum_{\mu\rho} \langle T^{(i)}_{\mu\rho} \bar{\partial}_\mu P^{(j)}_{T\rho} \rangle. \tag{5.42}$$

Furthermore, we sum over all directions ρ, and average over the whole volume keeping the distance constant to improve the signal.

To estimate which combinations of probes give a sensible solution to the LSE (5.40) one can first solve the LSE using the mean value of the data instead of bootstrapping. The practice is simple. We build the LSE by choosing four probes, a lattice size, a distance and a flow time, compute the mean of the measurements for each entry in $M^{(j,i)}$ and $V^{(j)}$, and solve for the c_i:

1. Choose four probes, a lattice size, a distance and a flow time
2. Take the mean of the corresponding measurements
3. Build the LSE (5.40) from these mean values
4. Solve for c_i

It has to be checked if this approach is justified. We have between 4000 to 40000 measurements for the expectation values in eq. (5.38) for every combination of probes, lattice sizes, distances and flow times which should give large enough statistics. Further, the data are normally distributed with a sufficiently small relative standard deviation for most expectation values. As an example, fig. 5.8 shows the histograms and the fit for the normal distribution of the expectation values in eq. (5.38) for $i = 2$, $j = 10$, $c(t) = 0.4157$, $L = 16, 18$, and $|x - y| = 0, 1$. We abbreviate the left-hand side and right-hand side of eq. (5.38) by $M^{(j,i)}$ and $V^{(j)}$, using the nomenclature of eq. (5.40).

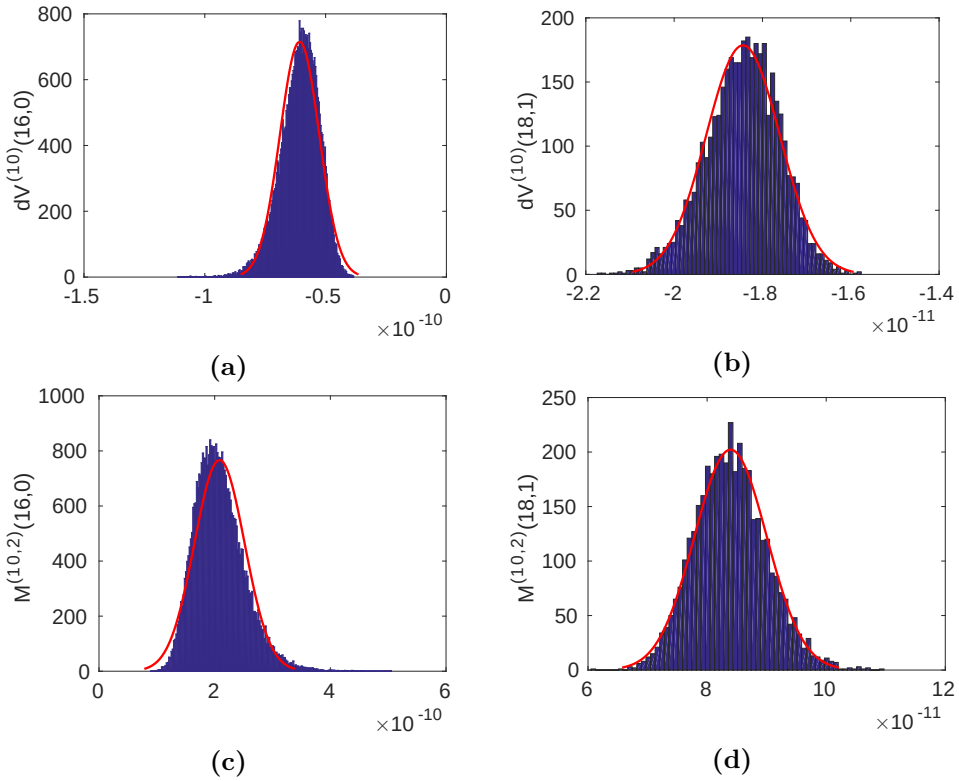

Figure 5.8 *Histograms for the expectation values in eq. (5.38) for $i = 2$, $j = 10$, $c(t) = 0.4157$ and (a) $V^{(j)}$, $L = 16$, $|x - y| = 0$, (b) $V^{(j)}$, $L = 18$, $|x - y| = 1$, (c) $M^{(j,i)}$, $L = 16$, $|x - y| = 0$, (d) $M^{(j,i)}$, $L = 18$, $|x - y| = 1$. The red curve is the fitted normal distribution.*

Further, we plotted the mean μ of all expectation values as well as the standard deviation σ. An example for $L = 16$ and $|x - y| = 0$ is shown in fig. 5.9. Both quantities trend towards zero with increasing flow time.

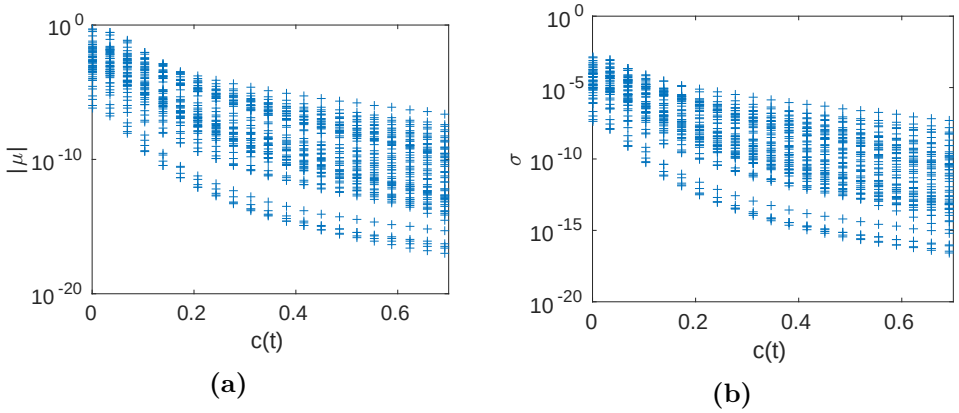

Figure 5.9 *(a) Absolute value of the mean and (b) standard deviation of the expectation values in eq. (5.38) for all probes, $L = 16$, $|x - y| = 0$.*

We then examined the relative standard deviation of all expectation values in eq. (5.38) for all probes. The highest values of σ/μ, up to 400%, occur for $L = 16$, $|x - y| = 0$ and are displayed in fig. 5.10. Sensible values for the c_i are obtained for $c(t) < 0.6$. A more detailed discussion looking at specific expectation values following shortly confirms that upper bound, see fig. 5.12 and the corresponding section. Hence, evaluating the LSE using the mean of the data is a valid first approach given that $c(t) < 0.6$.

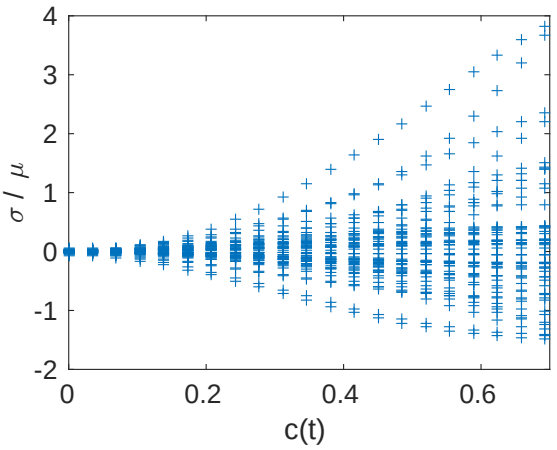

Figure 5.10 *Relative standard deviation of the expectation values in eq. (5.38) for all probes, $L = 16$, $|x - y| = 0$.*

Condition number

The next step to rate sensible combinations of probes is to compute the condition number of the matrix $M^{(j,i)}$. The condition number κ of a non-singular square matrix A is defined as

$$\kappa(A) = \|A\| \, \|A^{-1}\|. \tag{5.43}$$

While $\|\cdot\|$ in the equation above can be any matrix norm let us pick the two-norm. The two-norm of a vector $x \in \mathbb{R}^m$ is defined as

$$\|x\|_2 = \left(\sum_{i=1}^{m} |x_i|^2 \right)^{1/2}. \tag{5.44}$$

Matrix norms can be defined as being induced by vector norms so that the two-norm of a matrix $A \in \mathbb{R}^{m \times n}$ is

$$\|A\|_2 = \sup_{x \neq 0} \frac{\|Ax\|_2}{\|x\|_2}. \tag{5.45}$$

If the condition number $\kappa(A)$ is small, A is well-conditioned, otherwise, if $\kappa(A)$ is large, A is ill-conditioned. A very large condition number $\kappa(A) \to \infty$ indicates that the matrix is singular. The definitions of the norms and the condition number, as well as the statements about the condition number of a matrix can be found in [55].

The condition number of the matrix A of a LSE $Ax = b$ can be used to estimate how much the statistical errors in the vector b and the matrix A are amplified when computing the vector x. The rule of thumb is that if A is ill-conditioned one may lose $\log_{10} \kappa(A)$ digits in precision of the solution x compared to the precision of the entries in A and b [55, 56]. Hence, it is advisable to pick the LSE with the lowest condition number. This shall be our criterion for selecting the probes.

It is difficult to choose a set of probes such that the matrix $M^{(j,i)}$ is somewhat well conditioned over a wide range of flow times. This can be seen in fig. 5.11 where the condition number is plotted for different sets of probes as a function of the flow time for $L = 16, 32$ and $|x - y| = 0, 1.41$. In particular, these sets of probes are the ones that give the lowest and the highest condition numbers of all 330 combinations at some flow time. The lowest condition numbers are achieved for sets (8,9,10,11), (3,9,10,11), (2,8,9,10) and (2,9,10,11). The highest condition numbers are achieved for sets (1,2,3,7), (1,3,4,7) and (1,3,7,11). The condition number depends strongly on the flow time and on the set of probes. It can increase, decrease or jump orders of magnitude when increasing the flow time or when swapping a single probe for another one. Notably striking is the difference between lowest and highest values for the condition number which is almost twelve orders of magnitude. A very large condition number of the matrix also indicates that the matrix itself is singular which implies that the probes chosen are not independent enough.

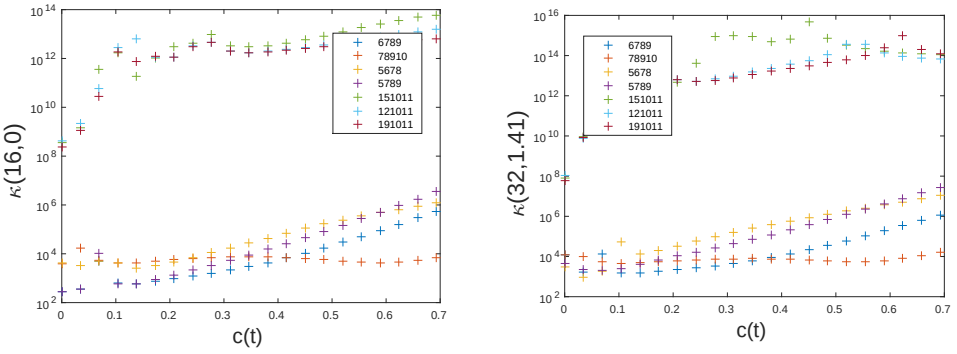

(a) **(b)**

Figure 5.11 *Condition numbers for the combinations of probes that give the smallest and largest condition numbers. The probe numbers correspond to the operators in tab. (5.9). (a) $L = 16$, $|x - y| = 0$, (b) $L = 32$, $|x - y| = 1.41$.*

From fig. 5.11 and all other combinations of lattice sizes and distances not shown here we can conclude that the most sensible combinations of probes are sets (8,9,10,11) and (3,9,10,11). These are the two sets we will concentrate on in the following analysis using the bootstrap method.

Parameters continued

Before moving on we can use our new knowledge of which combinations of probes give the lowest condition number to specify the relative standard deviation in fig. 5.10 for these probes. Fig. 5.12 displays four examples of the relative standard deviation for probes 3, 8, 9, 10, 11, $L = 16, 18$, $|x - y| = 0, 1$ of $V^{(j)}$ and $M^{(j,i)}$. Most of the measurements follow a normal distribution with a relative standard deviation well below 100%, see e.g. fig. 5.12a,b,d. Fig. 5.12c on the other hand shows one case where the relative standard deviation exceeds 100% at some flow time. In particular, measurements for $M^{(3,1)}$ and $M^{(3,4)}$ are the most widely spread. Taking 100% as the upper bound for the largest tolerated relative standard deviation, we find that we should discard results for $c(t) > 0.6$ for the set of probes (8,9,10,11), and for $c(t) > 0.5$ for the set of probes (3,9,10,11). Fig. 5.12c is one in three cases where a few points fall outside the chosen boundary. In total, there are only about 10 points above 100% for $c(t) < 0.5/0.6$.

For the sake of completeness we also show the absolute value of the mean and the standard deviation separately in fig. 5.13.

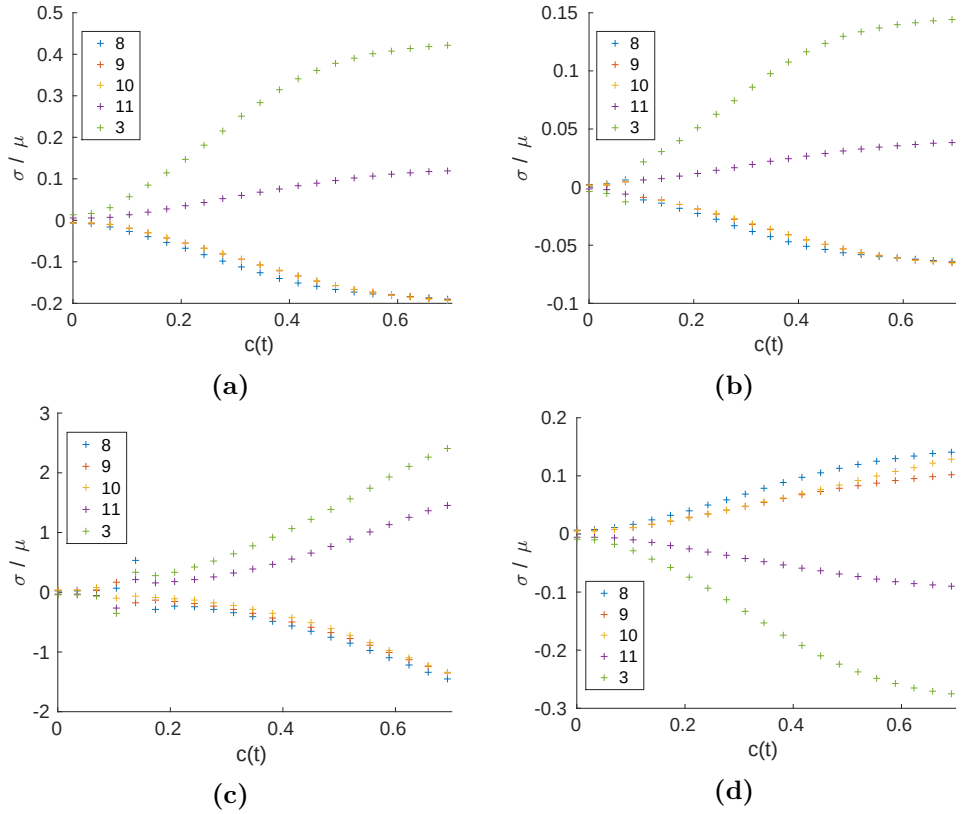

Figure 5.12 *Relative standard deviation for probes 3,8,9,10,11. (a)* $V^{(j)}$, $L = 16$, $|x-y| = 0$, *(b)* $V^{(j)}$, $L = 18$, $|x-y| = 1$, *(c)* $M^{(j,4)}$, $L = 16$, $|x-y| = 1$, *(d)* $M^{(j,2)}$, $L = 18$, $|x-y| = 0$.

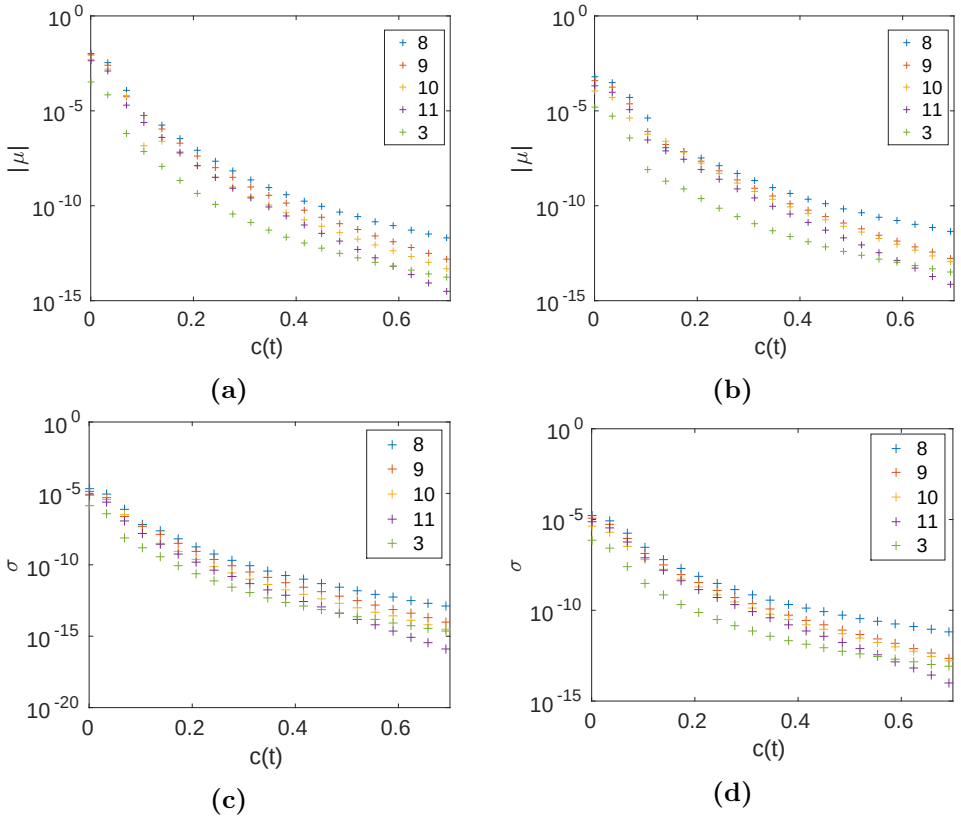

Figure 5.13 *Absolute value of the mean (a,b) and standard deviation (c,d) for probes 3,8,9,10,11. (a,c)* $V^{(j)}$, $L = 18$, $|x - y| = 1$, *(b,d)* $M^{(j,4)}$, $L = 16$, $|x - y| = 1$.

Condition number bootstrap

The condition number can also be used to pre-estimate the precision of the results of the renormalisation constants. It is possible to find a relation between the relative error of x and the relative errors of A and b, and the condition number. This task is complicated in our case by the use of the bootstrap method utilised to calculate the error in the solution vector. Working with the sum of the variances of $\langle x_i \rangle$ one can find an upper bound for the squared norm of the variance vector,

$$\begin{aligned}
\|\sigma_{\langle x \rangle}\|^2 &= \textstyle\sum_i \sigma^2_{\langle x_i \rangle} && (5.46)\\
&\leq \|A^{-1}\|^2_{max} \langle \|b - b'\|^2 \rangle && (5.47)\\
&\leq \|A^{-1}\|^2_{max} \langle \|b - \langle b \rangle\|^2 + \|b' - \langle b \rangle\|^2 + 2\|b - \langle b \rangle\| \|b' - \langle b \rangle\| \rangle && (5.48)\\
&\leq \|A^{-1}\|^2_{max} \left(\|\sigma_{\langle b \rangle}\|^2 + \|\sigma_{\langle A \rangle}\|^2 \|\langle x \rangle\|^2 + 2\|\sigma_{\langle b \rangle}\| \|\sigma_{\langle A \rangle}\| \|\langle x \rangle\| \right), && (5.49)
\end{aligned}$$

where we used brackets instead of bars to represent the bootstrap average compared to eqs. (5.27, 5.28) for better readability. $\|A^{-1}\|_{max}$ in the second line is the largest norm of all bootstrap samples, and $b'_j = A_{jk} \langle x_k \rangle$. In order to be able to make any statement we assumed that A and x as well as the fluctuations about the bootstrap average of A and b are uncorrelated. Dividing by the squared norm of the bootstrap average of x, inserting the definition of the condition number (5.43) and estimating the two-norm of A with the infinity-norm, we arrive at the desired expression

$$\frac{\|\sigma_{\langle x \rangle}\|^2}{\|\langle x \rangle\|^2} \leq \kappa(A)^2_{max} \left(\frac{\|\sigma_{\langle b \rangle}\|^2}{\|\langle b \rangle\|^2} + n \frac{\|\sigma_{\langle A \rangle}\|^2}{\|\langle A \rangle\|^2_\infty} + 2\sqrt{n} \frac{\|\sigma_{\langle b \rangle}\| \|\sigma_{\langle A \rangle}\|}{\|\langle b \rangle\| \|\langle A \rangle\|_\infty} \right). \tag{5.50}$$

Note that $\|\langle b \rangle\| \leq \|\langle A \rangle\| \|\langle x \rangle\|$ and $\|\langle A \rangle\|_2 \geq \frac{1}{\sqrt{n}} \|\langle A \rangle\|_\infty$. The detailed calculation can be found in appendix E.

Eq. (5.50) indicates that very small fluctuations about the bootstrap average of A and b can potentially compensate for a large condition number so that the relative errors of the solution vector x stay small. We compute the right-hand side of eq. (5.50) to see if it is possible to find a sensible upper bound on the relative errors in the renormalisation constants. Unfortunately, the upper bound found is very large, up to order $\mathcal{O}(10^8)$, and is not feasible to make any statements about the accuracy of the c_i. In particular, when calculating and comparing the left-hand side and right-hand side of eq. (5.50) explicitly after computing the c_i

it becomes very clear that our estimate of the upper bound is far off the actual value of the left-hand side of eq. (5.50). Fig. 5.14 shows the maximum difference in the order of magnitude of the left-hand side and right-hand side of eq. (5.50) at all flow times for the combinations of probes (8,9,10,11) or (3,9,10,11), lattice sizes (16,18,24,32) and distances (0,1,1.41). It ranges from $\mathcal{O}(10^6)$ to $\mathcal{O}(10^{10})$. The x-axis encodes the combinations of probes, lattice size and distance used which are decoded in tab. 5.11.

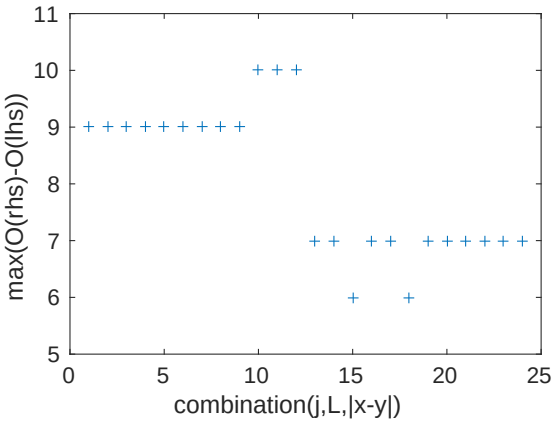

Figure 5.14 *Maximum difference in the order of magnitude of the left-hand side and right-hand side of eq. (5.50) for the two combinations of probes, all lattice sizes and distances.*

x	1	2	3	4	5	6	7	8	9	10	11	12
combi	111	112	113	121	122	123	131	132	133	141	142	143
x	13	14	15	16	17	18	19	20	21	22	23	24
combi	211	212	213	221	222	223	231	232	233	241	242	243

Table 5.11 *Decoding of the x-axis values in figs. 5.14, 5.15b. The first number in line 'combi' represents which probes were used, 1: 8,9,10,11 2: 3,9,10,11. The second number represents the lattice size, 1: 16, 2: 18, 3: 24, 4: 32. The third number stands for the distance, 1: 0, 2: 1, 3: 1.41.*

As an example fig. 5.15a displays the left-hand side and right-hand side of eq. (5.50) for probes (8,9,10,11), $L = 32$ and distance 1.41, while fig. 5.15b shows the maximum difference of the left-hand side and right-hand side of eq. (5.50) of all flow times. The x-axis encodes again the combinations of probes, lattice sizes and distances, see tab. 5.11.

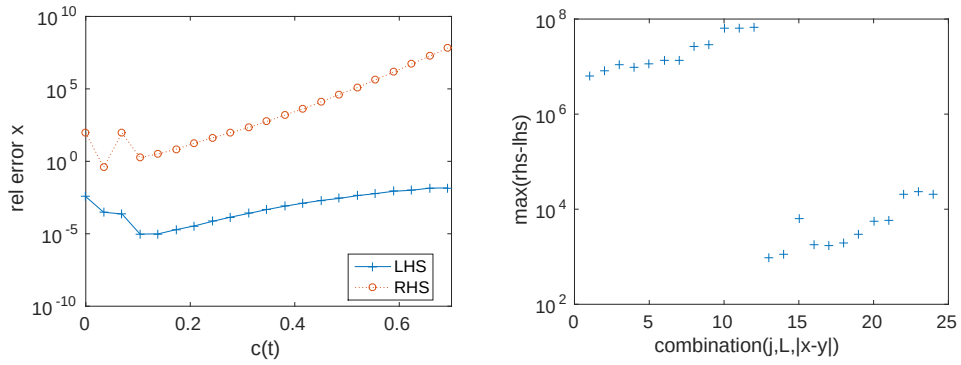

(a) (b)

Figure 5.15 *(a) Left-hand side and right-hand side of eq. (5.50) for probes (8,9,10,11), $L = 32$, $|x - y| = 1.41$. (b) Maximum difference of the left-hand side and right-hand side of eq. (5.50) for the two combinations of probes, all lattice sizes and distances.*

5.4.2 Computing the results

Having decided on the two best sets of probes with regard to the condition number we are finally in the position to perform the full analysis for the problem for these two sets of probes, namely using the bootstrap method. The bootstrap method applied to solving the LSE (5.40) proceeds as follows

1. Choose one of the two sets of probes, a lattice size, distance and flow time
2. Create s bootstrap samples for one of the corresponding data sets
3. Calculate the mean for each of the resampled samples
4. Calculate the best estimate and the variance according to eqs. (5.27, 5.28)
5. Repeat 2.–4. for all data sets corresponding to the choice made in 1.
6. Build the LSE (5.40) from these values
7. Solve for c_i

We resampled all data sets $s = 1000$ times. The solution to the LSE is found using LU factorisation with partial pivoting [55]. The results are shown in tabs. 5.13–5.16 and figs. 5.17–5.24 and will be discussed shortly. Before doing so let us have a brief look at the condition number again. Fig. 5.16 displays two examples of the fluctuations of the condition number about its bootstrap average and the mean.

The bootstrap error is indicated as well. It is evident that the fluctuations are twice as large for the high condition number as for the low one. This suggests that higher statistics of the measurements could improve the value of the condition number.

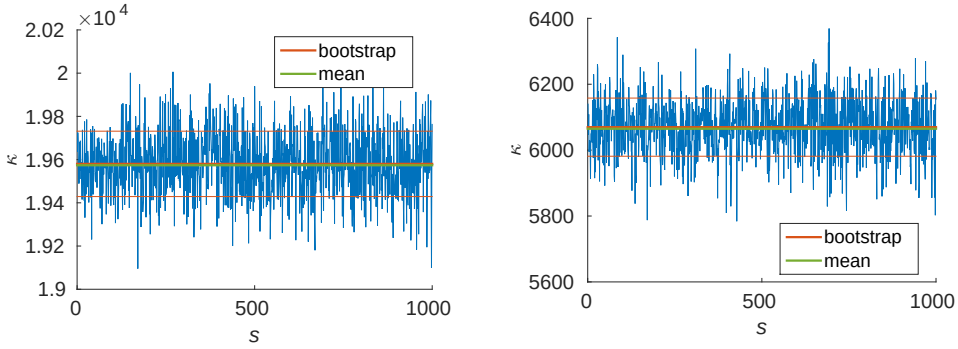

(a) **(b)**

Figure 5.16 *Fluctuations of the condition number for 1000 bootstrap samples about the bootstrap sample average and the mean for* $c(t) = 0.485$. *(a) probes (8,9,10,11),* $L = 18$, $|x - y| = 0$, *(b) probes (3,9,10,11),* $L = 32$, $|x - y| = 1$.

To extract results for the renormalisation constants, we plotted c_i as a function of $c(t)$ for both sets of probes, all lattice sizes and distances as shown in figs. 5.21–5.24 at the end of the chapter. A plateau was located for each plot by eye where there was an overlap of neighbouring error bars. The location of the plateau is roughly the same for every combination of set of probes and lattice size, and independent of the distance. The range of the plateau for every combination can be found in tab. 5.12.

set	L	$c(t)_{min}$	$c(t)_{max}$	n
(8,9,10,11)	16	0.450	0.589	4
	18	0.416		5
	24	0.381		6
	32	0.346		7
(3,9,10,11)	16,18,24	0.416	0.485	2
	32	0.346		4

Table 5.12 *Location of the plateau for the two sets of probes depending on the lattice size. The last column is the number of degrees of freedom needed to compute the chi-square and p-value of the fits.*

We computed the weighted arithmetic mean and its standard deviation for the chosen plateaus,

$$\begin{aligned} \bar{x} &= \frac{\sum_i \frac{x_i}{\sigma_i^2}}{\sum_i \frac{1}{\sigma_i^2}} \\ \sigma_{\bar{x}} &= \sqrt{\frac{1}{\sum_i \frac{1}{\sigma_i^2}}}. \end{aligned} \tag{5.51}$$

A quick calculation reveals that this is equivalent to performing a fit to a constant c which would mean to minimise eq. (5.30) for $f(x_i) = c$. Hence, chi-square and the p-value can be calculated according to eqs. (5.30) and (5.31). The number of degrees of freedom needed is in tab. 5.12. The results for the c_i for both sets of probes and every lattice size and distance are collected in tabs. 5.13–5.16, as well as the chi-square and p-value. The results that correspond to a p-value greater than or equal to 0.05 are marked bold.

In figs. 5.17–5.20 we plotted all bold values corresponding to $p \geq 0.05$ in tabs. 5.13–5.16. The orange horizontal line is the weighted mean of the plotted data, see eqs. (5.51). It can be seen in all plots that the data are very scattered so that there is not much overlap. Hence, for the final result we quote the statistical error and the systematic error separately. The reason for the spread in the data is very likely finite volume effects. The finite volume limit has to be investigated and we expect the systematic error to vanish once the data agree within error bars. The statistical error can be reduced by increasing the number of measurements.

Figs. 5.21–5.24 at the end of the chapter display the results for the c_i as a function of $c(t)$ for both sets of probes, all lattice sizes and distances. The plateau is drawn if $p \geq 0.05$. A plateau only forms for $c(t) > 0.3$. The reason is lattice artefacts that are not erased by the smearing property of the flow at that value. Also, remnants of divergencies from contact terms can distort the data at small flow time, if applicable. Moreover, we have to ignore data from $c(t) > 0.5$ as the signal is depleted due to the now dominating smearing radius.

L	$\lvert x-y\rvert$	$c_1(8,9,10,11)$	χ^2	p	$c_1(3,9,10,11)$	χ^2	p
16	0	2.110(2)	6.37	0.00	2.151(2)	43.59	0.00
	1	2.114(3)	3.23	0.01	2.158(2)	32.03	0.00
	1.41	2.121(3)	2.58	0.04	2.153(3)	21.39	0.00
18	0	2.107(2)	4.33	0.00	2.128(3)	18.59	0.00
	1	2.086(3)	7.00	0.00	2.115(3)	15.82	0.00
	1.41	2.087(3)	4.91	0.00	2.116(3)	13.61	0.00
24	0	**2.069(2)**	1.82	0.09	2.073(3)	8.13	0.00
	1	**2.064(3)**	0.92	0.48	**2.069(4)**	2.36	0.09
	1.41	**2.045(3)**	1.85	0.09	**2.062(4)**	2.81	0.06
32	0	**2.036(3)**	0.07	1.00	2.050(4)	3.13	0.01
	1	**2.043(3)**	0.66	0.70	2.058(4)	2.55	0.04
	1.41	**2.040(4)**	0.09	1.00	2.051(4)	2.68	0.03

Table 5.13 *Result for c_1 for the two sets of probes (8,9,10,11) and (3,9,10,11), all lattice sizes and distances, including the chi-square and p-value of the fit. The values of c_1 for which $p \geq 0.05$ are marked bold.*

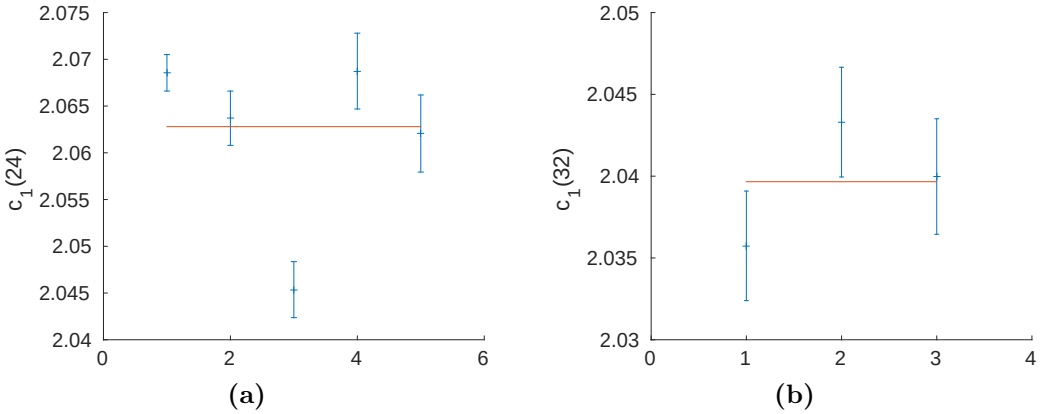

Figure 5.17 *Final result for c_1. In blue the bold values in tab. 5.13, in orange the weighted mean.*

L	$\lvert x-y\rvert$	$c_2(8,9,10,11)$	χ^2	p	$c_2(3,9,10,11)$	χ^2	p
16	0	**0.082(5)**	0.98	0.42	**0.068(4)**	0.15	0.86
	1	**0.085(6)**	1.73	0.14	**0.064(5)**	0.01	0.99
	1.41	**0.061(7)**	2.13	0.07	**0.060(6)**	0.20	0.82
18	0	0.064(4)	3.37	0.00	**0.054(4)**	0.02	0.98
	1	**0.091(5)**	0.33	0.90	**0.068(5)**	0.13	0.88
	1.41	**0.088(5)**	1.28	0.27	**0.067(5)**	0.00	1.00
24	0	0.052(2)	4.95	0.00	**0.043(3)**	0.00	1.00
	1	**0.061(4)**	1.12	0.35	**0.052(5)**	0.01	0.99
	1.41	**0.083(4)**	0.11	0.99	**0.064(5)**	0.07	0.93
32	0	**0.051(3)**	1.38	0.21	**0.045(3)**	0.09	0.99
	1	**0.045(3)**	1.04	0.40	**0.040(3)**	0.21	0.93
	1.41	0.048(4)	2.68	0.01	**0.045(3)**	0.21	0.93

Table 5.14 *Result for c_2 for the two sets of probes (8,9,10,11) and (3,9,10,11), all lattice sizes and distances, including the chi-square and p-value of the fit. The values of c_2 for which $p \geq 0.05$ are marked bold.*

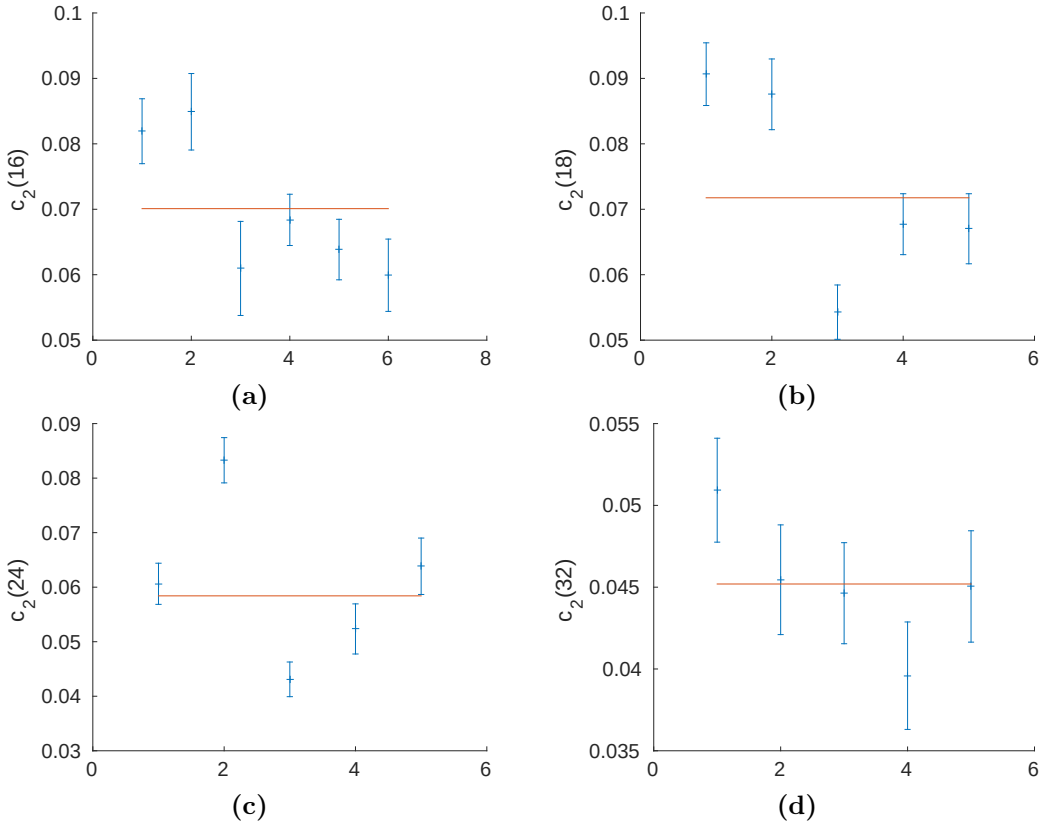

Figure 5.18 *Final result for c_2. In blue the bold values in tab. 5.14, in orange the weighted mean.*

L	$\lvert x-y\rvert$	$c_3(8,9,10,11)$	χ^2	p	$c_3(3,9,10,11)$	χ^2	p
16	0	**-1.35(4)**	1.10	0.35	**-1.23(3)**	0.17	0.84
	1	**-1.38(5)**	1.84	0.12	**-1.19(4)**	0.00	1.00
	1.41	**-1.17(6)**	2.23	0.06	**-1.16(5)**	0.18	0.83
18	0	-1.08(4)	3.54	0.00	**-0.99(4)**	0.02	0.98
	1	**-1.30(4)**	0.38	0.86	**-1.10(4)**	0.13	0.88
	1.41	**-1.28(5)**	1.39	0.22	**-1.09(5)**	0.00	1.00
24	0	-0.75(2)	5.11	0.00	**-0.68(3)**	0.00	1.00
	1	**-0.83(3)**	1.17	0.32	**-0.75(4)**	0.01	0.99
	1.41	**-1.02(4)**	0.12	0.99	**-0.85(4)**	0.08	0.93
32	0	**-0.63(3)**	1.41	0.20	**-0.58(3)**	0.07	0.99
	1	**-0.58(3)**	1.08	0.37	**-0.53(3)**	0.20	0.94
	1.41	-0.61(3)	2.70	0.01	**-0.58(3)**	0.20	0.94

Table 5.15 *Result for c_3 for the two sets of probes (8,9,10,11) and (3,9,10,11), all lattice sizes and distances, including the chi-square and p-value of the fit. The values of c_3 for which $p \geq 0.05$ are marked bold.*

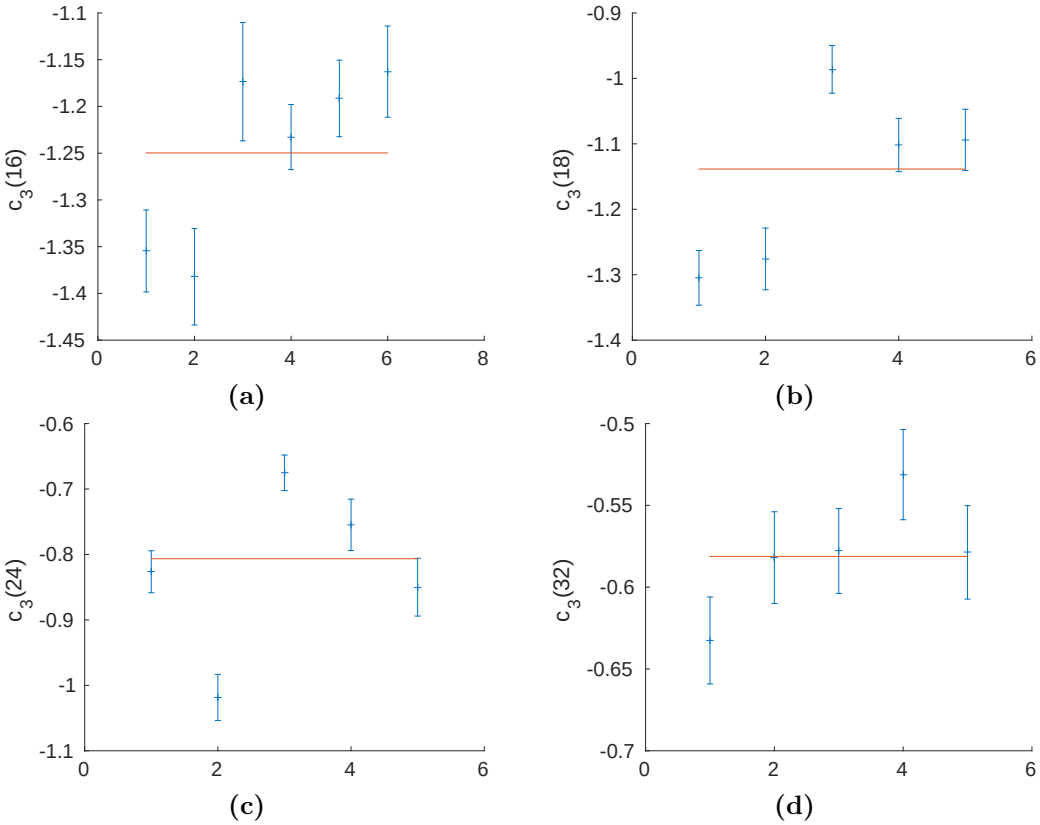

Figure 5.19 *Final result for c_3. In blue the bold values in tab. 5.15, in orange the weighted mean.*

L	$\|x-y\|$	$c_4(8,9,10,11)$	χ^2	p	$c_4(3,9,10,11)$	χ^2	p
16	0	-0.952(2)	10.70	0.00	-0.979(2)	24.72	0.00
	1	-0.958(2)	6.58	0.00	-0.987(2)	16.67	0.00
	1.41	-0.967(3)	4.65	0.00	-0.990(2)	10.93	0.00
18	0	-0.980(2)	5.49	0.00	-0.993(2)	9.32	0.00
	1	-0.963(2)	10.33	0.00	-0.982(2)	10.51	0.00
	1.41	-0.963(2)	7.93	0.00	-0.982(2)	9.71	0.00
24	0	**-0.999(2)**	1.49	0.18	-1.002(2)	3.47	0.03
	1	**-0.995(2)**	1.00	0.42	**-0.999(3)**	1.30	0.27
	1.41	**-0.982(3)**	0.61	0.73	**-0.991(3)**	0.93	0.40
32	0	**-1.000(3)**	0.11	1.00	**-1.009(3)**	0.85	0.49
	1	**-0.994(3)**	0.83	0.56	**-1.003(3)**	1.48	0.21
	1.41	**-0.994(3)**	0.01	1.00	**-1.000(3)**	0.94	0.44

Table 5.16 *Result for c_4 for the two sets of probes (8,9,10,11) and (3,9,10,11), all lattice sizes and distances, including the chi-square and p-value of the fit. The values of c_4 for which $p \geq 0.05$ are marked bold.*

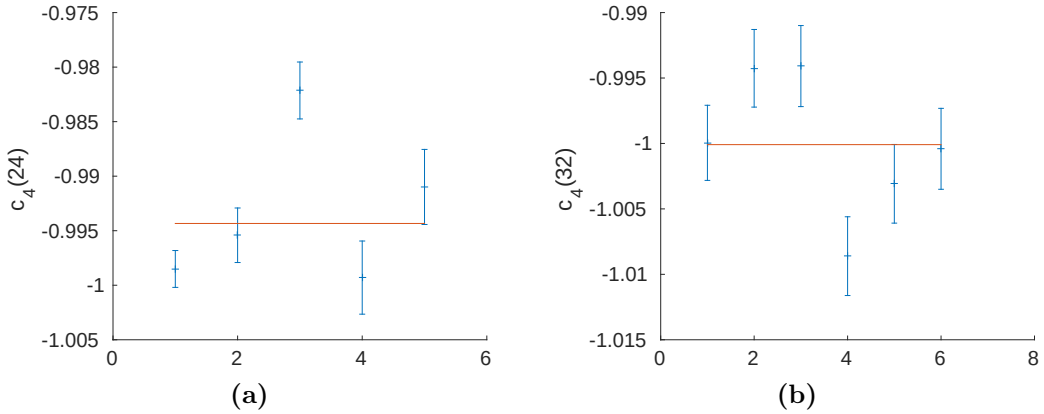

Figure 5.20 *Final result for c_4. In blue the bold values in tab. 5.16, in orange the weighted mean.*

5.4.3 Results

For the final result we quote the weighted mean, the largest statistical error per renormalisation constant and lattice size, and the systematic error as the largest difference between a central value and the weighted mean. These can be found in tab. 5.17.

	L	c_i
c_1	24	2.063(4)(20)
	32	2.040(4)(4)
c_2	16	0.070(7)(10)
	18	0.072(5)(20)
	24	0.058(5)(20)
	32	0.045(3)(6)
c_3	16	-1.25(6)(10)
	18	-1.14(5)(20)
	24	-0.81(4)(2)
	32	-0.58(3)(5)
c_4	24	-0.994(3)(10)
	32	-1.000(3)(9)

Table 5.17 *Final results for all c_i depending on the lattice size. The first bracket indicates the statistical error, the second one the systematic error.*

Tab. 5.18 compares the numerical results to the ones calculated perturbatively in sec. 4.3, eqs. (4.90). Note that we rescaled the coefficients by factors of 2 or 4! in eq. (5.35) compared to eq. (4.89).

The perturbative value for c_2/m^2 was found using eqs. (4.90, 4.4, 4.24), and expanding for small lattice spacing,

$$\frac{c_2}{m^2} = -1 - \frac{\lambda_R}{m^2}\frac{Z_1}{6} \tag{5.52}$$

$$= -1 + \frac{Z_1}{3Z_0} + \mathcal{O}(a) \tag{5.53}$$

$$\simeq -0.83. \tag{5.54}$$

	L	numerical	perturbative
c_1	24	2.063(4)(20)	2
	32	2.040(4)(4)	
$\frac{c_2}{m^2}$	16	-0.89(9)(13)	-0.83
	18	-0.95(7)(26)	
	24	-0.9(1)(3)	
	32	-0.82(5)(11)	
c_3	16	-1.25(6)(10)	-1
	18	-1.14(5)(20)	
	24	-0.81(4)(2)	
	32	-0.58(3)(5)	
$\frac{c_4}{\lambda}$	24	-1.325(4)(13)	-1
	32	-1.778(5)(16)	

Table 5.18 *Comparison of the results for the c_i obtained numerically and perturbatively.*

The values of c_1 and c_2/m^2 of the numerical and the perturbative analysis agree reasonably well. We expect the numerical values to approach the perturbative ones in the infinite volume limit, given that we are close enough to the GFP. In contrast, the numerical values of c_3 are scattered around the perturbative value and increase towards the GFP, and the numerical values of c_4/λ rather disagree with the perturbative one. This behaviour and deviation could as well be eliminated by studying the infinite volume limit of the EMT, and by simulating closer to the GFP since we might not be in the perturbative region in our simulations.

There are several possibilities to improve the numerical results. The first one that comes to mind is to enhance the statistics by multiplying the number of measurements of the correlators. Furthermore, we only tested a small subset of probes for the final analysis arguing that we need a small condition number. However, even the smallest condition number is of order 10^3 in the range of flow times we are interested in. One should explore either the full set of combinations of probes, or at least a larger subset in the future. We also mention in sec. 5.4.1 that we can combine equations with different distances and flow times as well. Since the analysis was carried out only for $\rho = 5$ we should explore other lines of constant physics, see sec. 5.3. In general, further studies require more simulations, larger lattices, and systems closer to the continuum limit.

Instead of evaluating a LSE with four equations one can approach the problem with a different strategy and extract the renormalisation constants by combining all sets of probes in a single overdetermined LSE. Another interesting point to investigate is if and how the probes depend on each other and why certain combinations give a relatively low and others a much larger condition number.

Having the data along lines of constant physics will ultimately enable us to perform the continuum limit of the EMT. This in turn provides a check of the accuracy of the entire strategy to compute the EMT using the Wilson flow. Before doing so we have to take the infinite volume limit of the EMT for every point on the lines of constant physics. Remember that the different lattice sizes in tab. 5.17 correspond to points on the line of constant physics since we keep the physical volume fixed.

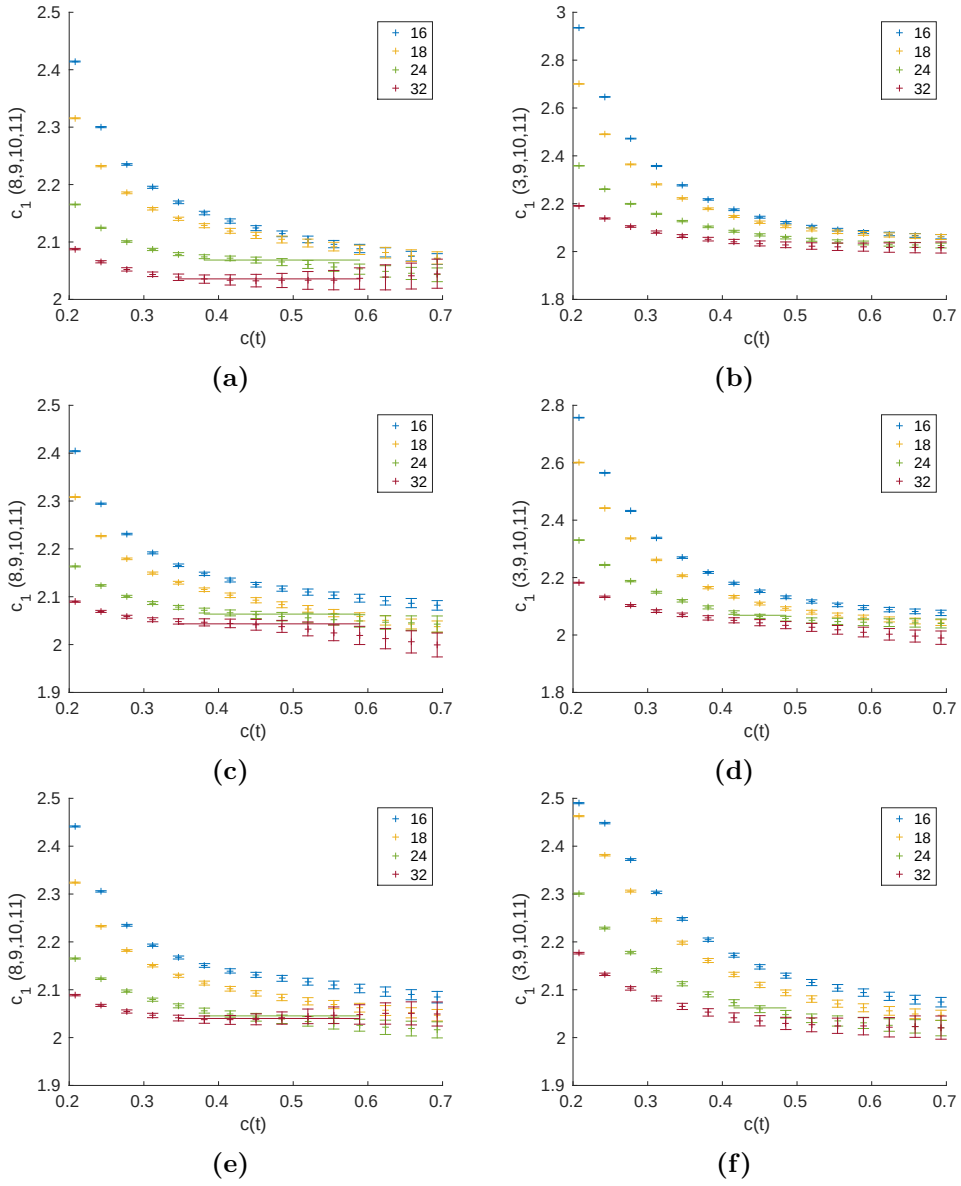

Figure 5.21 *Values of c_1 as a function of $c(t)$ and the fitted result. The left column displays the results received from probe set (8,9,10,11), the right column displays the results received from probe set (3,9,10,11). (a,b) $|x-y|=0$, (c,d) $|x-y|=1$, (e,f) $|x-y|=1.41$. The plateau value is only drawn for the lattice sizes where $p \geq 0.05$ over the range reported in tab. 5.12.*

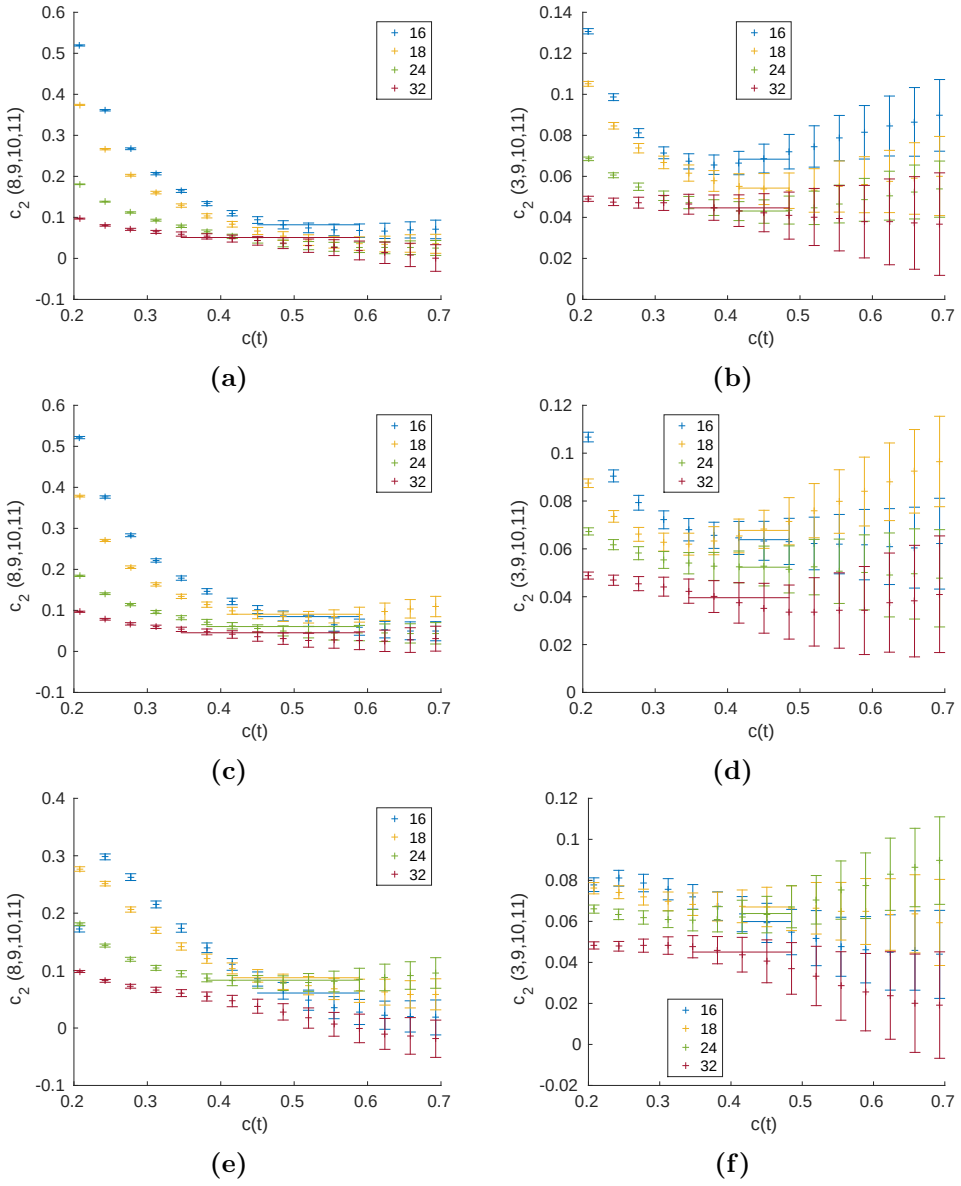

Figure 5.22 *Values of c_2 as a function of $c(t)$ and the fitted result. The left column displays the results received from probe set (8,9,10,11), the right column displays the results received from probe set (3,9,10,11). (a,b) $|x-y|=0$, (c,d) $|x-y|=1$, (e,f) $|x-y|=1.41$. The plateau value is only drawn for the lattice sizes where $p \geq 0.05$ over the range reported in tab. 5.12.*

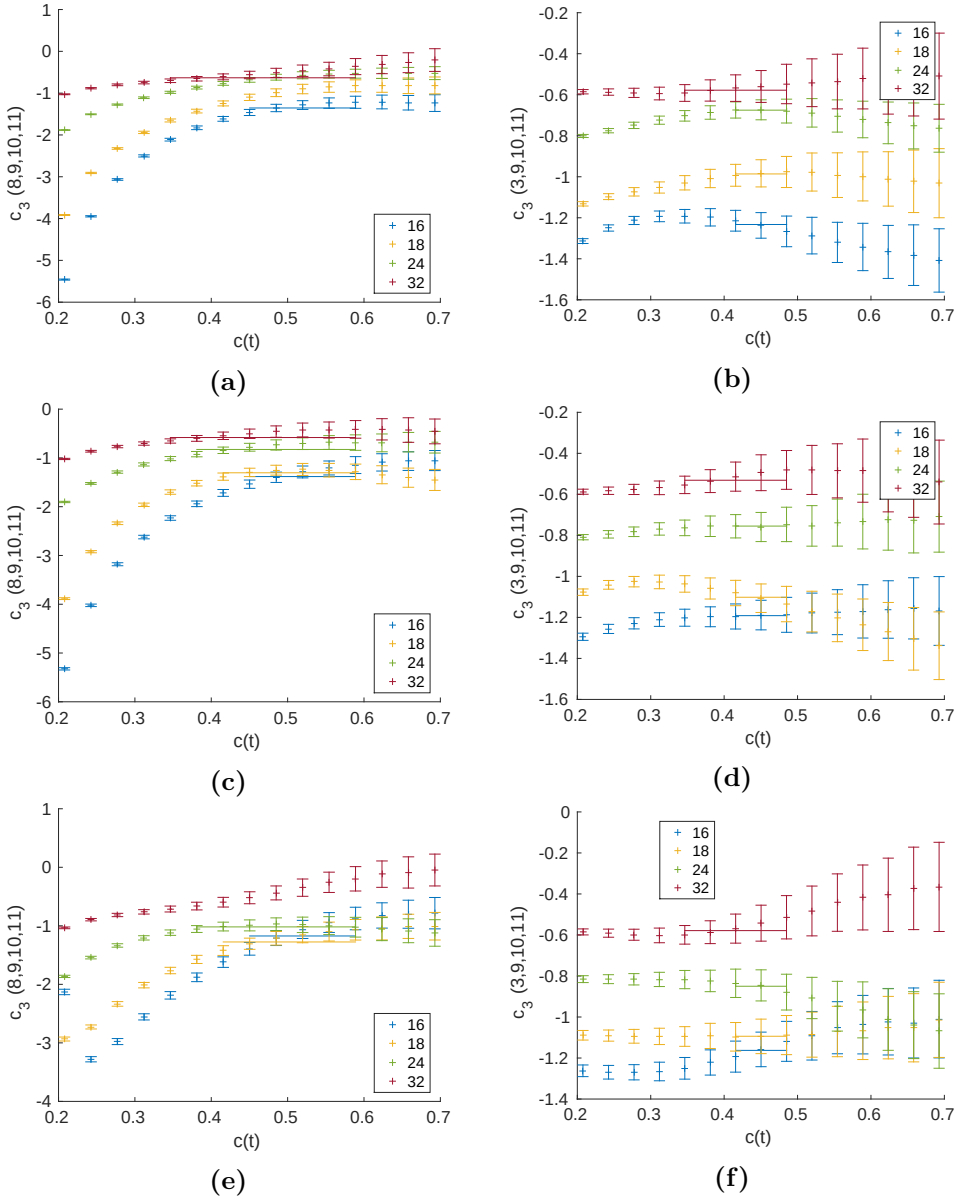

Figure 5.23 *Values of c_3 as a function of $c(t)$ and the fitted result. The left column displays the results received from probe set (8,9,10,11), the right column displays the results received from probe set (3,9,10,11). (a,b) $|x-y|=0$, (c,d) $|x-y|=1$, (e,f) $|x-y|=1.41$. The plateau value is only drawn for the lattice sizes where $p \geq 0.05$ over the range reported in tab. 5.12.*

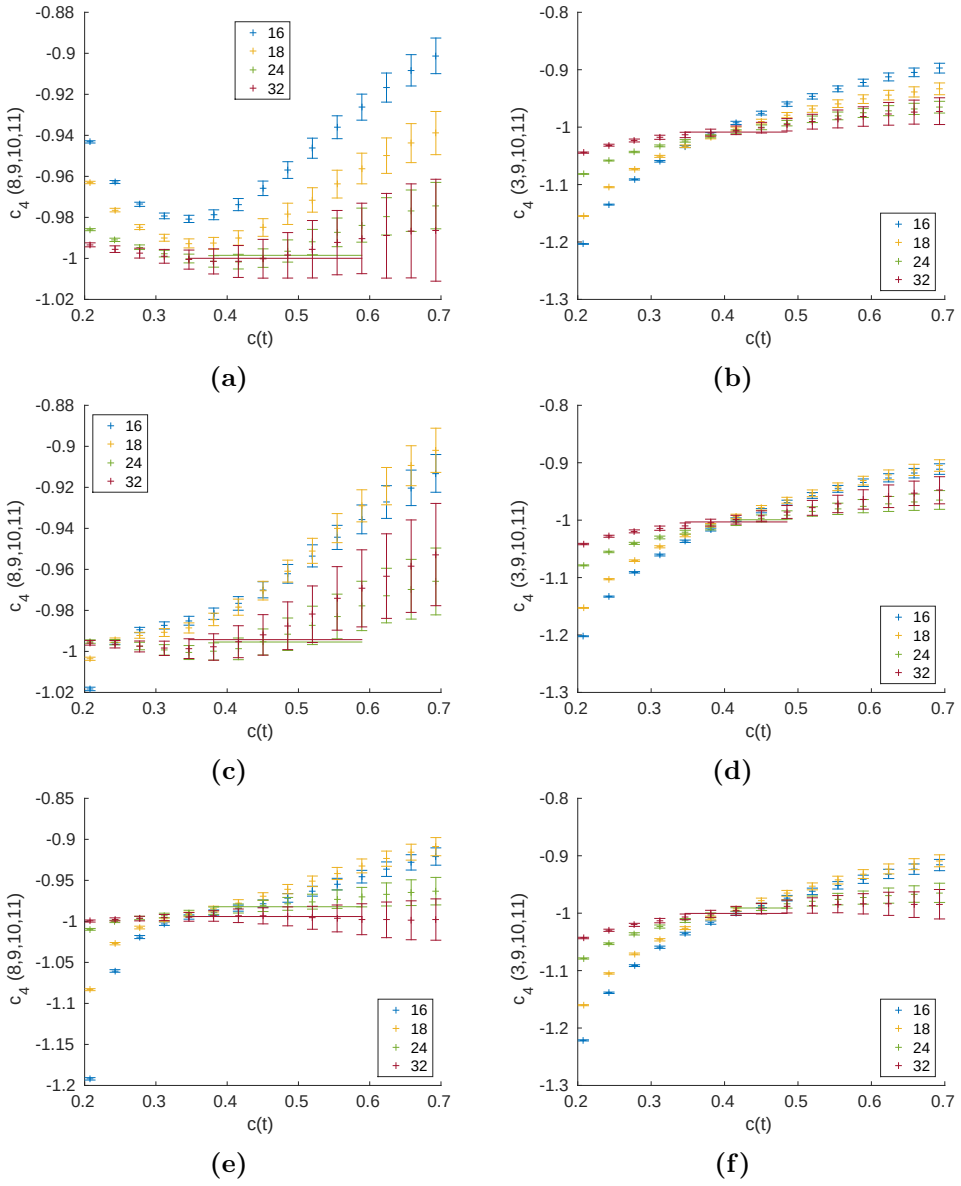

Figure 5.24 *Values of c_4 as a function of $c(t)$ and the fitted result. The left column displays the results received from probe set (8,9,10,11), the right column displays the results received from probe set (3,9,10,11). (a,b) $|x-y| = 0$, (c,d) $|x-y| = 1$, (e,f) $|x-y| = 1.41$. The plateau value is only drawn for the lattice sizes where $p \geq 0.05$ over the range reported in tab. 5.12.*

6

Conclusion

We set forth to find out whether combining numerical lattice computations with the gradient flow provides a feasible method for determining the renormalised EMT on the lattice. More precisely, we inspected the TWI using probes at positive flow time and calculated the coefficients of the renormalised EMT by inverting a LSE. In order to test the method we chose to study scalar ϕ^4-theory in three dimensions as it has a clear analytic structure and is computationally cheap. Furthermore, it exhibits an infrared fixed point so that theories beyond the standard model with such a fixed point can be tested.

This is the very first satisfactory determination of the coefficients of the EMT using this particular methodology. We were able to extract the coefficients of the renormalised EMT from a square LSE built from TWIs with different probes. This was done for one line of constant physics with $\rho = 5$ consisting of four points corresponding to different values of the lattice spacing. The results including errors are satisfying.

There are various possibilities to improve the results. For one, we only tested two combinations of probes arguing that they induce the smallest condition number of the matrix. However, the condition number is still very high so we should test other combinations of probes. It is also interesting to explore why certain combinations of probes lead to a relatively small, others to a very large condition number, as well as the dependence of the probes amongst each other. Furthermore, we only evaluated LSEs where all equations have the same distance

and flow time to reduce the number of possible combinations. Other combinations should be investigated. A slightly different method to compute the coefficients of the renormalised EMT is to use an overdetermined system of equations instead of a square one. A check for the validity of our approach is to take the continuum limit of the EMT. Lastly, one should do the analysis for the other three lines of constant physics we computed.

Generally, further studies require a larger number of simulations, both in the sense of increasing the number of measurements and in varying the type and number of probes. Larger lattices as well as simulations closer to the continuum limit are necessary.

The next step is to investigate the region close to the infrared fixed point. In the far future the insights gained can be applied to strongly coupled theories.

Appendix A

Continuum

A.1 Integrals

Abbreviation of the momentum integral in the continuum

$$\int_k = \int \frac{d^d k}{(2\pi)^d} \tag{A.1}$$

Volume integral of a function depending on radius r only

$$\int f(r)\, d^d x = \frac{d\, \pi^{d/2}}{\Gamma(1+\frac{d}{2})} \int_0^R r^{d-1} f(r)\, dr \tag{A.2}$$

Feynman parametrisation

$$\frac{1}{A_1 A_2} = \int_0^1 dx_1 \int_0^1 dx_2 \frac{\delta(1-x_1-x_2)}{(x_1 A_1 + x_2 A_2)^2} \tag{A.3}$$

$$\frac{1}{A_1^{\alpha_1} A_2^{\alpha_2} ... A_k^{\alpha_k}} = \frac{\Gamma(\alpha_1+\alpha_2+...\alpha_k)}{\Gamma(\alpha_1)\Gamma(\alpha_2)...\Gamma(\alpha_k)} \int_0^1 dx_1 x_1^{\alpha_1-1} \int_0^1 dx_2 x_2^{\alpha_2-1} ... \tag{A.4}$$

$$\times \int_0^1 dx_k x_k^{\alpha_k-1} \frac{\delta(1-x_1-x_2-...x_k)}{(x_1 A_1 + x_2 A_2 + ...x_k A_k)^{\alpha_1+\alpha_2+...\alpha_k}} \tag{A.5}$$

Integral over two momentum components

$$\int k_\mu k_\rho = \frac{\delta_{\mu\rho}}{d} \int k^2 \tag{A.6}$$

Momentum integrals

$$\int \frac{d^d k}{(2\pi)^d} \frac{1}{(k^2 + M^2)^\alpha} = \frac{1}{(4\pi)^{d/2}} \frac{\Gamma(\alpha - \frac{d}{2})}{\Gamma(\alpha)} (M^2)^{\frac{d}{2} - \alpha} \tag{A.7}$$

$$\int \frac{d^d k}{(2\pi)^d} \frac{k^2}{(k^2 + M^2)^\alpha} = \frac{1}{(4\pi)^{d/2}} \frac{d}{2} \frac{\Gamma(\alpha - \frac{d}{2} - 1)}{\Gamma(\alpha)} (M^2)^{\frac{d}{2} - \alpha + 1} \tag{A.8}$$

A.2 Derivation of the energy-momentum tensor

A.2.1 General Ward identity

Consider the expectation value of a generic probe

$$\langle \mathcal{P} \rangle = \frac{1}{\mathcal{Z}} \int D\phi \, \mathcal{P}(\phi, \partial_\tau \phi, ...) \, e^{-S(\phi, \partial_\tau \phi, ...)}, \tag{A.9}$$

where $\mathcal{P}$ and S are functions of the field and derivatives of the field ϕ. The representation of expectation values through a path integral is explained in detail in app. B in the context of lattice field theory. Changing the field with an infinitesimal transformation $\phi \to \phi + \delta\phi$ gives

$$\langle \mathcal{P} \rangle = \frac{1}{\mathcal{Z}} \int D\phi \, \mathcal{P}(\phi + \delta\phi, \partial_\tau(\phi + \delta\phi), ...) \, e^{-S(\phi + \delta\phi, \partial_\tau(\phi + \delta\phi), ...)}. \tag{A.10}$$

Using the Taylor expansion of a function F,

$$\begin{aligned} F(\phi + \delta\phi, \partial_\tau(\phi + \delta\phi), ...) = F(\phi, \partial_\tau \phi, ...) &+ \int d^d x \, \frac{\partial F}{\partial \phi} \, \delta\phi \\ &+ \int d^d x \sum_\tau \frac{\partial F}{\partial(\partial_\tau \phi)} \, \partial_\tau \delta\phi + ... \, , \end{aligned} \tag{A.11}$$

the left-hand side in eq. (A.10) cancels with the zeroth order summand on the right-hand side leaving us with the integrated Ward identity

$$\langle \mathcal{P}\ \delta S \rangle = \langle \delta \mathcal{P} \rangle, \tag{A.12}$$

where we defined

$$\delta F = \int d^d x \left(\frac{\partial F}{\partial \phi}\ \delta\phi + \sum_\tau \frac{\partial F}{\partial(\partial_\tau \phi)}\ \partial_\tau \delta\phi + ... \right). \tag{A.13}$$

Defining

$$\delta F = \int d^d x\ \delta_x F, \tag{A.14}$$

we can write down the local Ward identity,

$$\langle \mathcal{P}\ \delta_x S \rangle = \langle \delta_x \mathcal{P} \rangle. \tag{A.15}$$

A.2.2 Translation Ward identity

For a local translation in direction $\hat{\rho}$, $x_\mu \to x'_\mu = x_\mu + \delta_{\mu\rho}\alpha(x)$, the variation of the scalar field is

$$\delta\phi(x) = \delta_\rho \phi(x) = \alpha(x)\, \partial_\rho \phi(x). \tag{A.16}$$

The integrated TWI then reads

$$\langle \mathcal{P}\ \delta_\rho S \rangle = \langle \delta_\rho \mathcal{P} \rangle, \tag{A.17}$$

where we indicated the direction $\hat{\rho}$ of the transformation as a subscript,

$$\delta_\rho F = \int d^d x \left(\frac{\partial F}{\partial \phi}\ \alpha(x)\, \partial_\rho \phi(x) + \sum_\tau \frac{\partial F}{\partial(\partial_\tau \phi)}\ \partial_\tau(\alpha(x)\, \partial_\rho \phi(x)) + ... \right). \tag{A.18}$$

Defining

$$\delta_\rho F = \int d^d x\ \alpha(x)\ \delta_{x,\rho} F, \tag{A.19}$$

we find the local TWI,

$$\langle \mathcal{P}\ \delta_{x,\rho} S \rangle = \langle \delta_{x,\rho} \mathcal{P} \rangle. \tag{A.20}$$

Note the difference in the definition of δ_x and $\delta_{x,\rho}$ in eqs. (A.15,A.20),

$$\delta_x = \alpha(x)\delta_{x,\rho}. \tag{A.21}$$

A.2.3 Energy-momentum tensor

We define the EMT from the invariance of the theory under global translations by computing the local variation of the action in the TWI (A.20) explicitly. The action in scalar ϕ^4-theory reads

$$S = \int d^dx \left(\frac{1}{2} \sum_\sigma (\partial_\sigma \phi)^2 + \frac{m^2}{2}\phi^2 + \frac{\lambda}{4!}\phi^4 \right). \tag{A.22}$$

The local variation of the action is

$$\begin{aligned} \delta_{x,\rho} S &= \frac{\partial S}{\partial \phi(x)} \partial_\rho \phi(x) + \sum_\tau \frac{\partial S}{\partial(\partial_\tau \phi(x))} \frac{1}{\alpha(x)} \partial_\tau(\alpha(x)\partial_\rho \phi(x)) \qquad (A.23) \\ &= m^2 \phi(x)\partial_\rho \phi(x) + \frac{\lambda}{3!}\phi(x)^3 \partial_\rho \phi(x) + \sum_\tau (\partial_\tau \phi(x)) \frac{1}{\alpha(x)} \partial_\tau(\alpha(x)\partial_\rho \phi(x)). \end{aligned}$$

It is easy to see that the first and second term can be rewritten as

$$m^2 \phi \partial_\rho \phi = \sum_\mu \partial_\mu \delta_{\mu\rho} \frac{m^2}{2}\phi^2 \tag{A.24}$$

$$\frac{\lambda}{3!}\phi^3 \partial_\rho \phi = \sum_\mu \partial_\mu \delta_{\mu\rho} \frac{\lambda}{4!}\phi^4. \tag{A.25}$$

For the third term we have to remember that originally there is an integral over space-time in the integrated TWI enabling us to integrate by parts. We find

$$\sum_\tau (\partial_\tau \phi) \frac{1}{\alpha} \partial_\tau(\alpha \partial_\rho \phi) = \sum_\mu \partial_\mu \left(-\partial_\mu \phi \partial_\rho \phi + \delta_{\mu\rho} \frac{1}{2} \sum_\sigma (\partial_\sigma \phi)^2 \right). \tag{A.26}$$

Thus, the local variation of the action becomes

$$\delta_{x,\rho} S = -\sum_\mu \partial_\mu T_{\mu\rho}(x), \tag{A.27}$$

where we defined the EMT,

$$T_{\mu\rho} = \partial_\mu\phi\partial_\rho\phi - \delta_{\mu\rho}\left(\frac{1}{2}\sum_\sigma(\partial_\sigma\phi)^2 + \frac{m^2}{2}\phi^2 + \frac{\lambda}{4!}\phi^4\right). \tag{A.28}$$

Using eq. (A.27) in the local TWI (A.20) we find the local TWI expressed with the EMT,

$$\sum_\mu \partial_\mu\langle T_{\mu\rho}(x)\ \mathcal{P}\rangle = -\langle\delta_{x,\rho}\mathcal{P}\rangle. \tag{A.29}$$

A.2.4 Energy-momentum tensor – alternative way

In this section we shall derive the EMT again in a second way from the variation of the action in eq. (A.17) which is more commonly described in textbooks,

$$\begin{aligned}
\delta_\rho S &= S - S' \\
&= S - \int d^dx\ (1+\partial_\rho\alpha)\ \mathcal{L}\left[\phi, (\partial_\mu - (\partial_\mu\alpha)\,\partial_\rho)\,\phi\right] \\
&= S - \int d^dx \left(\mathcal{L}\left[\phi,\partial_\mu\phi\right] - \sum_\mu(\partial_\mu\alpha)\ \partial_\rho\phi\ \frac{\mathcal{L}\left[\phi,\partial_\mu\phi\right]}{\partial(\partial_\mu\phi)} + (\partial_\rho\alpha)\ \mathcal{L}\left[\phi,\partial_\mu\phi\right]\right) \\
&= \int d^dx\ \sum_\mu \partial_\mu\alpha\left(\partial_\rho\phi\ \frac{\partial\mathcal{L}\left[\phi,\partial_\mu\phi\right]}{\partial(\partial_\mu\phi)} - \delta_{\mu\rho}\,\mathcal{L}\left[\phi,\partial_\mu\phi\right]\right) \\
&= -\int d^dx\ \alpha\sum_\mu \partial_\mu T_{\mu\rho}.
\end{aligned} \tag{A.30}$$

We omitted writing the dependence on x of α and ϕ for readability. Note that the relative sign between S' and S as well as the sign of the Noether current are an arbitrary choice. Furthermore, we used the relations

$$\phi(x) = \phi'(x') \tag{A.31}$$

$$d^dx' = (1+\partial_\rho\alpha)\,d^dx + \mathcal{O}(\alpha^2) \tag{A.32}$$

$$\partial'_\mu = \partial_\mu - (\partial_\mu\alpha)\partial_\rho + \mathcal{O}(\alpha^2). \tag{A.33}$$

In the last line of eq. (A.30) we integrated by parts and defined the EMT as

$$T_{\mu\rho} = \partial_\rho \phi \, \frac{\partial \mathcal{L}}{\partial(\partial_\mu \phi)} - \delta_{\mu\rho} \, \mathcal{L}. \tag{A.34}$$

Calculating the EMT from the previous equation leads to the aforementioned result in eq. (A.28).

A.3 Energy-momentum tensor insertion at one loop

There are two potentially divergent insertions of the EMT (2.33)

$$T_{\mu\rho} = \partial_\mu \phi \partial_\rho \phi - \delta_{\mu\rho} \left(\frac{1}{2} \sum_\sigma \partial_\sigma \phi \partial_\sigma \phi + \frac{m^2}{2} \phi^2 + \frac{\lambda}{4!} \phi^4 \right) \tag{A.35}$$

at one loop order, both in two-point functions. The first one is

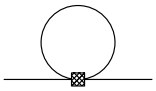

$$= -\frac{\lambda}{2} \int_k \frac{1}{k^2 + m^2}, \tag{A.36}$$

which is canceled by the mass renormalisation. For the second diagram we need the leading order insertion of the EMT,

$$= -p_{1\mu} p_{2\rho} - p_{1\rho} p_{2\mu} + \delta_{\mu\rho} \sum_\sigma p_{1\sigma} p_{2\sigma}, \tag{A.37}$$

where p_1, p_2 are the ingoing external momenta. Using the above result in the numerator of the loop integral and naming q the momentum of the EMT we find

for the second divergent diagram

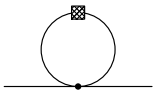

$$= -\frac{\lambda}{2}\int_k \frac{k_\mu(k+q)_\rho + k_\rho(k+q)_\mu - \delta_{\mu\rho}\sum_\sigma k_\sigma(k+q)_\sigma}{(k^2+m^2)((k+q)^2+m^2)} \tag{A.38}$$

$$= -\frac{\lambda}{2}\int_k \int_0^1 dx\, \frac{k_\mu(k+q)_\rho + k_\rho(k+q)_\mu - \delta_{\mu\rho}\sum_\sigma k_\sigma(k+q)_\sigma}{((1-x)(k^2+m^2)+x((k+q)^2+m^2))^2} \tag{A.39}$$

$$= -\lambda\int_0^1 dx \int_l \left(\frac{\delta_{\mu\rho}(\frac{1}{d}-\frac{1}{2})l^2}{(l^2+M^2)^2} + \frac{x(x-1)(q_\mu q_\rho - \frac{1}{2}\delta_{\mu\rho}q^2)}{(l^2+M^2)^2}\right). \tag{A.40}$$

We used Feynman parametrisation (A.3) in the second line. In the third line we changed variables, $l = k + xq$, used eq. (A.6), and defined $M^2 = m^2 + x(1-x)q^2$. The only divergent term is the one proportional to l^2 which is in turn proportional to the operator ϕ^2. As the derivative of the EMT has to vanish but $\partial_\mu\phi^2$ does not, this term cannot produce a divergence either. Thus, the EMT is finite at one-loop level in three dimensions.

Let us check the effect of the term (2.39)

$$\partial O = \alpha\left(\partial_\mu\partial_\rho - \delta_{\mu\rho}\sum_\sigma \partial_\sigma^2\right)\phi^2 \tag{A.41}$$

as well. The leading order reads

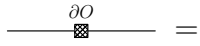

$$= 2\alpha\,(-p_{1\mu}p_{2\rho} - p_{1\rho}p_{2\mu} - p_{1\mu}p_{1\rho} - p_{2\mu}p_{2\rho} \tag{A.42}$$

$$+\delta_{\mu\rho}\sum_\sigma\left(p_{1\sigma}p_{2\sigma} + p_{1\sigma}^2 + p_{2\sigma}^2\right)\Bigg). \tag{A.43}$$

Performing a similar calculation as for the insertion of $T_{\mu\rho}$, we find

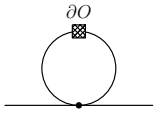

$$= -\lambda\alpha\int_0^1 dx\int_l \frac{-q_\mu q_\rho + \delta_{\mu\rho}\sum_\sigma q_\sigma^2}{(l^2+M^2)^2}, \tag{A.44}$$

which is convergent in three dimensions. Thus, adding ∂O to the EMT does neither change the TWI nor the EMT's divergent structure.

For a detailed derivation of eqs. (A.37,A.38) see app. (D). The calculation there is done on the lattice which is easily translated to the continuum. The other expressions are derived in a similar way.

A.4 Finiteness of the energy-momentum tensor to all orders

Another method to obtain the result from the previous section is to extract the divergencies by Taylor expanding the loop integral in small external momenta. For the one-loop insertion it is sufficient to examine the integral

$$I_{1\mu\rho} = \int_k \frac{k_\mu (k+q)_\rho}{(k^2+m^2)((k+q)^2+m^2)} \tag{A.45}$$

as the divergences of the other terms in eq. (A.38) will be of the same nature. We need the first and second derivative for the Taylor series,

$$\frac{\partial}{\partial q_\tau} I_{1\mu\rho} = \int_k \frac{k_\mu \delta_{\rho\tau}}{(k^2+m^2)((k+q)^2+m^2)} - \int_k \frac{2k_\mu (k+q)_\rho (k+q)_\tau}{(k^2+m^2)((k+q)^2+m^2)^2}, \tag{A.46}$$

$$\begin{aligned} \frac{\partial}{\partial q_\omega}\frac{\partial}{\partial q_\tau} I_{1\mu\rho} = &- \int_k \frac{k_\mu \delta_{\rho\tau} 2(k+q)_\omega}{(k^2+m^2)((k+q)^2+m^2)^2} \\ &- \int_k \frac{2k_\mu (k_\rho \delta_{\tau\omega} + k_\tau \delta_{\rho\omega} + q_\tau \delta_{\rho\omega} + q_\rho \delta_{\tau\omega})}{(k^2+m^2)((k+q)^2+m^2)^2} \\ &+ \int_k \frac{8k_\mu (k+q)_\rho (k+q)_\tau (k+q)_\omega}{(k^2+m^2)((k+q)^2+m^2)^3}. \end{aligned} \tag{A.47}$$

The Taylor expansion of $I_{1\mu\rho}$ to second order is

$$\begin{aligned} I_{1\mu\rho} = &\int_k \frac{k_\mu k_\rho}{(k^2+m^2)^2} - 2q_\omega q_\tau \int_k \frac{k_\mu k_\omega \delta_{\rho\tau} + k_\mu k_\rho \delta_{\tau\omega} + k_\mu k_\tau \delta_{\rho\omega}}{(k^2+m^2)^3} \\ &+ 8q_\omega q_\tau \int_k \frac{k_\mu k_\rho k_\tau k_\omega}{(k^2+m^2)^4} + \mathcal{O}(q^3). \end{aligned} \tag{A.48}$$

Only the first term is divergent in three dimensions and proportional to ϕ^2 so that we have confirmed our conclusion from the previous section.

There are two more potentially divergent diagrams in scalar ϕ^4-theory in three dimensions,

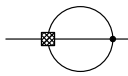

$$\propto I_{2\mu\rho} = \int_{k_1,k_2} \frac{1}{(k_1^2+m^2)(k_2^2+m^2)((k+q)^2+m^2)} \tag{A.49}$$

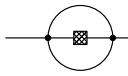

$$\sim I_{3\mu\rho} = \int_{k_1,k_2} \frac{(k+p)_\mu (k+p+q)_\rho}{(k_1^2+m^2)(k_2^2+m^2)((k+p)^2+m^2)((k+p+q)^2+m^2)}, \tag{A.50}$$

where q in $I_{2\mu\rho}$ is the sum of the external momenta from the propagator and the EMT. For $I_{3\mu\rho}$ it is sufficient to study the above integral as all other summands have the same divergent structure. The momentum p in $I_{3\mu\rho}$ is the momentum of the propagator and q the momentum of the EMT. We can set $p = 0$ for our purpose and define $k = k_1 + k_2$.

The derivatives of $I_{2\mu\rho}$ are

$$\frac{\partial}{\partial q_\tau} I_{2\mu\rho} = -\int_{k_1,k_2} \frac{2(k+q)_\tau}{(k_1^2+m^2)(k_2^2+m^2)((k+q)^2+m^2)^2} \tag{A.51}$$

$$\begin{aligned} \frac{\partial}{\partial q_\omega}\frac{\partial}{\partial q_\tau} I_{2\mu\rho} = &-\int_{k_1,k_2} \frac{2\delta_{\tau\omega}}{(k_1^2+m^2)(k_2^2+m^2)((k+q)^2+m^2)^2} \\ &+\int_{k_1,k_2} \frac{8(k+q)_\tau (k+q)_\omega}{(k_1^2+m^2)(k_2^2+m^2)((k+q)^2+m^2)^3}. \end{aligned} \tag{A.52}$$

The derivatives of $I_{3\mu\rho}$ are

$$\begin{aligned} \frac{\partial}{\partial q_\tau} I_{3\mu\rho} = &\int_{k_1,k_2} \frac{k_\mu \delta_{\rho\tau}}{(k_1^2+m^2)(k_2^2+m^2)(k^2+m^2)((k+q)^2+m^2)} \\ &-\int_{k_1,k_2} \frac{2k_\mu (k+q)_\rho (k+q)_\tau}{(k_1^2+m^2)(k_2^2+m^2)(k^2+m^2)((k+q)^2+m^2)^2} \end{aligned} \tag{A.53}$$

$$\begin{aligned} \frac{\partial}{\partial q_\omega}\frac{\partial}{\partial q_\tau} I_{3\mu\rho} = &-\int_{k_1,k_2} \frac{2k_\mu \delta_{\rho\tau}(k+q)_\omega}{(k_1^2+m^2)(k_2^2+m^2)(k^2+m^2)((k+q)^2+m^2)^2} \\ &-\int_{k_1,k_2} \frac{2k_\mu \delta_{\rho\omega}(k+q)_\tau + 2k_\mu (k+q)_\rho \delta_{\tau\omega}}{(k_1^2+m^2)(k_2^2+m^2)(k^2+m^2)((k+q)^2+m^2)^2} \\ &+\int_{k_1,k_2} \frac{8k_\mu (k+q)_\rho (k+q)_\tau (k+q)_\omega}{(k_1^2+m^2)(k_2^2+m^2)(k^2+m^2)((k+q)^2+m^2)^3}. \end{aligned} \tag{A.54}$$

The Taylor expansion of $I_{2\mu\rho}$ to second order is

$$\begin{aligned} I_{2\mu\rho} = &\int_{k_1,k_2} \frac{1}{(k_1^2+m^2)(k_2^2+m^2)(k^2+m^2)} \\ &- 2q_\tau q_\omega \delta_{\tau\omega} \int_{k_1,k_2} \frac{1}{(k_1^2+m^2)(k_2^2+m^2)(k^2+m^2)^2} \\ &+ 8q_\tau q_\omega \int_{k_1,k_2} \frac{k_\tau k_\omega}{(k_1^2+m^2)(k_2^2+m^2)(k^2+m^2)^3} + \mathcal{O}(q^3), \end{aligned} \tag{A.55}$$

where again only the first term is divergent in three dimensions and proportional to ϕ^2.

The Taylor expansion of $I_{3\mu\rho}$ to second order is

$$\begin{aligned} I_{3\mu\rho} = &\int_{k_1,k_2} \frac{k_\mu k_\rho}{(k_1^2+m^2)(k_2^2+m^2)(k^2+m^2)^2} \\ &- 2q_\tau q_\omega \int_{k_1,k_2} \frac{k_\mu \delta_{\rho\tau} k_\omega + k_\mu \delta_{\rho\omega} k_\tau + k_\mu k_\rho \delta_{\tau\omega}}{(k_1^2+m^2)(k_2^2+m^2)(k^2+m^2)^3} \\ &+ 8q_\tau q_\omega \int_{k_1,k_2} \frac{k_\mu k_\rho k_\tau k_\omega}{(k_1^2+m^2)(k_2^2+m^2)(k^2+m^2)^4} + \mathcal{O}(q^3), \end{aligned} \tag{A.56}$$

where yet again only the first term is divergent in three dimensions and proportional to ϕ^2.

Higher orders in the Taylor series will generate even more convergent terms as every derivative with respect to q increases the power of the loop momentum in the numerator by one or zero, and the in the denominator by at least two. Thus, the difference in the powers in the loop momentum decreases with every loop momentum.

From the above analysis follows that the EMT is finite to all orders in three dimensions since all diagrams beyond two loops are finite.

Appendix B

Lattice

B.1 Preliminaries

The Fourier transform of a function $f(x = na)$ and the inverse transform, a Fourier series, on a cubic space-time lattice $\Lambda = a\mathbb{Z}^4 = \{x \mid x_\mu/a \in \mathbb{Z}\}$ with lattice constant a in d dimensions are

$$f(na) = \int_{-\frac{\pi}{a}}^{\frac{\pi}{a}} \frac{d^d k}{(2\pi)^d}\, e^{ikna} \tilde{f}(k) \tag{B.1}$$

$$\tilde{f}(k) = a^d \sum_n e^{-ikna} f(na). \tag{B.2}$$

The Kronecker delta and the momentum space delta function read

$$\delta_{nm} = a^d \int_{-\frac{\pi}{a}}^{\frac{\pi}{a}} \frac{d^d k}{(2\pi)^d}\, e^{ik(n-m)a} \tag{B.3}$$

$$\delta^d(k) = \frac{a^d}{(2\pi)^d} \sum_n e^{-ikna}. \tag{B.4}$$

Further, we abbreviate the momentum integral on the lattice as

$$\int_k = \int_{-\frac{\pi}{a}}^{\frac{\pi}{a}} \frac{d^d k}{(2\pi)^d}. \tag{B.5}$$

Derivatives on the lattice turn into finite differences. We define forward, backward and symmetric derivative as follows:

$$\hat{\partial}_\mu \phi(x) = \frac{1}{a}\left(\phi(x + a\hat{\mu}) - \phi(x)\right) \tag{B.6}$$

$$\hat{\partial}^*_\mu \phi(x) = \frac{1}{a}\left(\phi(x) - \phi(x - a\hat{\mu})\right) \tag{B.7}$$

$$\bar{\partial}_\mu \phi(x) = \frac{1}{2a}\left(\phi(x + a\hat{\mu}) - \phi(x - a\hat{\mu})\right), \tag{B.8}$$

where $\hat{\mu}$ is the unit vector in direction μ.

It is advantageous to define the following lattice momenta:

$$\hat{k}_\mu = \frac{2}{a}\sin\frac{k_\mu a}{2}, \quad \hat{k}^2 = \frac{4}{a^2}\sum_\mu \sin^2\frac{k_\mu a}{2} \tag{B.9}$$

$$\bar{k}_\mu = \frac{1}{a}\sin k_\mu a, \quad \bar{k}^2 = \frac{1}{a^2}\sum_\mu \sin^2 k_\mu a. \tag{B.10}$$

We can also define the following discrete Laplacian operator,

$$\Delta = \sum_\mu \hat{\partial}^*_\mu \hat{\partial}_\mu. \tag{B.11}$$

B.2 Correlation functions

Correlation functions can be formulated using the path integral formalism,

$$\langle \phi(n_1)\phi(n_2)... \rangle = \mathcal{Z}^{-1} \int D\phi \; \phi(n_1)\phi(n_2)... \; e^{-S(\phi)}, \tag{B.12}$$

where

$$\mathcal{Z} = \int D\phi \; e^{-S(\phi)} \tag{B.13}$$

and the integration measure is defined by

$$D\phi = \prod_n d\phi(na). \tag{B.14}$$

It is useful to define the generating functional

$$Z(J) = \int D\phi \, e^{-S(J)} \tag{B.15}$$

with

$$S(J) = a^d \sum_n \left(\mathcal{L} + J\phi\right). \tag{B.16}$$

Fields can be expressed as derivatives with respect to the sources J,

$$\phi(n) = -\frac{1}{a^d}\frac{\delta}{\delta J(n)} \, e^{-a^d \sum J\phi}\Big|_{J=0}, \tag{B.17}$$

so that n-point functions can be written as

$$\langle \phi(n_1)\phi(n_2)... \rangle = \left(-\frac{1}{a^d}\frac{\delta}{\delta J(n_1)}\right)\left(-\frac{1}{a^d}\frac{\delta}{\delta J(n_2)}\right)... \, Z(J)\Big|_{J=0}. \tag{B.18}$$

To calculate correlation functions in perturbation theory we observe that one can replace the fields in the interaction part of the action, S_I, using eq. (B.17) and pull the exponential out of the integral,

$$Z(J) = \int D\phi \, e^{-S(J)} \tag{B.19}$$

$$= e^{-S_I(\delta/\delta J)} Z_0(J), \tag{B.20}$$

where Z_0 is the generating functional of the free theory containing only the free scalar action plus the source term, $S_0(J)$. The exponential in eq. (B.20) can then be expanded in orders of the coupling.

B.3 ϕ^4-theory

The Lagrangian in ϕ^4-theory with bare fields and couplings reads

$$\mathcal{L} = \frac{1}{2}\hat{\partial}_\mu\phi\hat{\partial}_\mu\phi + \frac{1}{2}m^2\phi^2 + \frac{\lambda}{4!}\phi^4. \tag{B.21}$$

Defining the renormalised field ϕ_R, renormalised mass m_R and renormalised coupling λ_R via

$$\phi = Z^{1/2}\phi_R, \qquad \delta_Z = Z - 1, \qquad \delta_m = m^2 Z - m_R^2, \qquad \delta_\lambda = \lambda Z^2 - \lambda_R, \quad \text{(B.22)}$$

yields

$$\mathcal{L} = \frac{1}{2}\hat{\partial}_\mu\phi_R\hat{\partial}_\mu\phi_R + \frac{1}{2}m_R^2\phi_R^2 + \frac{\lambda_R}{4!}\phi_R^4 + \frac{1}{2}\delta_Z\hat{\partial}_\mu\phi_R\hat{\partial}_\mu\phi_R + \frac{1}{2}\delta_m\phi_R^2 + \frac{1}{4!}\delta_\lambda\phi_R^4. \quad \text{(B.23)}$$

B.3.1 Feynman rules

From now on we work with the Lagrangian that contains only renormalised parameters and omit all indices R on the fields and couplings.

Propagator

The propagator is calculated from the generating functional of the free theory. Fourier transforming the fields in the free action,

$$S_0 = a^d \sum_x \frac{1}{2}\phi(x)\left(-\hat{\partial}_\mu\hat{\partial}^*_\mu + m^2\right)\phi(x) \quad \text{(B.24)}$$

$$= \frac{a^d}{2}\sum_x \int_{kk'} e^{i(k+k')x}\left(-\frac{1}{a^2}\sum_\mu\left(e^{ik'_\mu a} - 2 + e^{-ik'_\mu a}\right) + m^2\right)\tilde{\phi}(k)\tilde{\phi}(k') \quad \text{(B.25)}$$

$$= \frac{1}{2}\int_k \left(\hat{k} + m^2\right)\tilde{\phi}(k)\tilde{\phi}(-k), \quad \text{(B.26)}$$

where we used

$$\hat{\partial}_\mu\hat{\partial}^*_\mu\phi(x) = \frac{1}{a^2}\left(\phi(x + a\hat{\mu}) - 2\phi(x) + \phi(x - a\hat{\mu})\right) \quad \text{(B.27)}$$

in the second line, and $\cos 2x = 1 - 2\sin^2 x$ in the third line while also integrating out the delta function that arises from evaluating the sum. The lattice momentum $\hat{k}_\mu$ has been defined in eq. (B.9). The Fourier transform of the fields and sources

in $S_0(J)$ then reads

$$S_0(J) = a^d \sum_n \int_{pk} e^{i(p+k)na} \left(\frac{1}{2} \left(\hat{k}^2 + m^2 \right) \tilde{\phi}(p)\tilde{\phi}(k) + \tilde{J}(p)\tilde{\phi}(k) + \tilde{J}(k)\tilde{\phi}(p) \right). \tag{B.28}$$

Introducing the shift

$$\tilde{\eta} = \tilde{\phi} + \frac{1}{\hat{k}^2 + m^2} \tilde{J} \tag{B.29}$$

leads to

$$S_0(J) = a^d \sum_n \int_{pk} e^{i(p+k)na} \frac{1}{2} \left(\eta(\tilde{p})(\hat{k}^2 + m^2)\tilde{\eta}(k) - \tilde{J}(p) \frac{1}{\hat{k}^2 + m^2} \tilde{J}(k) \right). \tag{B.30}$$

The first term is a Gaussian and can be integrated out in $Z_0(J)$. Hence, after integrating over the delta function that we gain from evaluating the sum in $S_0(J)$ we receive the generating functional for both, the Fourier transform of the fields and sources, and for the fields and sources themselves:

$$Z_0(J) = \exp\left\{ \frac{1}{2} \int_k \tilde{J}(-k) \frac{1}{\hat{k}^2 + m^2} \tilde{J}(k) \right\} \tag{B.31}$$

$$= \exp\left\{ \frac{1}{2} a^d \sum_n a^d \sum_m J(n) D(n-m) J(m)) \right\}, \tag{B.32}$$

where

$$D(n-m) = \int_k e^{ik(n-m)a} \frac{1}{\hat{k}^2 + m^2}. \tag{B.33}$$

The expression for the propagator can now be achieved by calculating the two-point correlation function of the free theory, eq. (B.18),

$$\langle \phi(n)\phi(m) \rangle = \left(-\frac{1}{a^d} \frac{\delta}{\delta J(n)} \right) \left(-\frac{1}{a^d} \frac{\delta}{\delta J(m)} \right) Z_0(J) \Big|_{J=0} \tag{B.34}$$

$$= D(n-m). \tag{B.35}$$

The propagator in momentum space is

$$\langle \tilde{\phi}(p)\tilde{\phi}(q) \rangle = a^d \sum_n a^d \sum_m e^{-ipna} e^{-iqma} \langle \phi(n)\phi(m) \rangle \tag{B.36}$$

$$= (2\pi)^d \delta^d(p+q) \tilde{D}(\hat{p}^2) \tag{B.37}$$

where we defined

$$\tilde{D}(\hat{p}^2) = \frac{1}{\hat{p}^2 + m^2}. \tag{B.38}$$

Vertices

The vertices are obtained by following the description at the end of sec. B.2. To calculate the vertex of interest we pick the appropriate term in the interaction part of the action, replace the fields with derivatives with respect to the sources and expand the exponential in eq. (B.20). Doing so gives

- the four-point vertex in position and momentum space,

$$\langle \phi(n_1)\phi(n_2)\phi(n_3)\phi(n_4)\rangle_\lambda = \frac{1}{a^{4d}} \prod_j^4 \tfrac{\delta}{\delta J(n_j)} Z(J)_\lambda \Big|_{J=0} \tag{B.39}$$

$$= a^d \sum_m [-\lambda] \prod_j^4 D(n_j - m) \tag{B.40}$$

$$\langle \tilde{\phi}(p_1)\tilde{\phi}(p_2)\tilde{\phi}(p_3)\tilde{\phi}(p_4)\rangle_\lambda = (2\pi)^d \delta^d(\textstyle\sum_i^4 p_i)\,[-\lambda] \prod_j^4 \frac{1}{(\hat{p_j}^2 + m^2)^2} \tag{B.41}$$

- the two-point vertex counterterm in position and momentum space,

$$\langle \phi(n_1)\phi(n_2)\rangle_{counter} = \frac{1}{a^{2d}} \frac{\delta}{\delta J(n_1)} \frac{\delta}{\delta J(n_2)} Z(J)_{counter} \Big|_{J=0} \tag{B.42}$$

$$= \int_k e^{ik(n-m)a} \left[-\left(\delta_Z \hat{k}^2 + \delta_m \right) \right] \frac{1}{(\hat{k}^2 + m^2)^2} \tag{B.43}$$

$$\langle \tilde{\phi}(p)\tilde{\phi}(q)\rangle_{counter} = (2\pi)^d \delta^d(p+q) \left[-\left(\delta_Z \hat{p}^2 + \delta_m \right) \right] \frac{1}{(\hat{p}^2 + m^2)^2} \tag{B.44}$$

- and the four-point counterterm in position and momentum space which is obtained exactly like the four-point vertex with $\lambda \to \delta_\lambda$.

$Z(J)_{counter}$ and $Z(J)_\lambda$ are

$$Z(J)_\lambda = -a^d \sum_n \frac{\lambda}{4!} \left(-\frac{1}{a^d} \frac{\delta}{\delta J(n)} \right)^4 Z_0(J) \tag{B.45}$$

$$Z(J)_{counter} = -\frac{a^{2d}}{2} \sum_{nm} \int_k e^{ik(n-m)a} \left(\delta_Z \hat{k}^2 + \delta_m \right) \frac{1}{a^{2d}} \frac{\delta}{\delta J(n)} \frac{\delta}{\delta J(m)} Z_0(J). \tag{B.46}$$

The Feynman rules in momentum space are presented in fig. B.1.

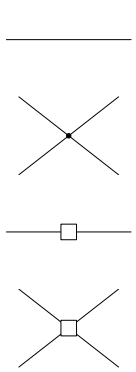

$$\tilde{D}(\hat{p}^2) = \frac{1}{\hat{p}^2 + m^2}$$

$$-\lambda_R$$

$$-\delta_Z \hat{p}^2 - \delta_m$$

$$-\delta_\lambda$$

Figure B.1 *Feynman rules for scalar ϕ^4-theory on the lattice.*

B.3.2 Self-energy tadpole at one loop

The self-energy in perturbation theory is the sum of all amputated, one-particle irreducible two-point diagrams. In ϕ^4-theory at one-loop level there is one diagram contributing besides the counterterms. We need two external fields and the λ-term in S_I:

$$\langle \phi(n)\phi(m) \rangle_\lambda = \left(-\frac{1}{a^d} \frac{\delta}{\delta J(n)} \right) \left(-\frac{1}{a^d} \frac{\delta}{\delta J(m)} \right) \times \tag{B.47}$$

$$\times \left(-\frac{\lambda}{4!} \right) a^d \sum_{n'} \left(-\frac{1}{a^d} \frac{\delta}{\delta J(n')} \right)^4 Z_0(J) \Big|_{J=0} \tag{B.48}$$

$$= -\frac{\lambda}{2} a^d \sum_{n'} D(0) D(n - n') D(m - n'). \tag{B.49}$$

The two-point function in momentum space is

$$\langle \tilde{\phi}(p)\tilde{\phi}(q) \rangle_\lambda = (2\pi)^d \delta^d(p + q) \left[-\frac{\lambda}{2} \int_k \frac{1}{\hat{k}^2 + m^2} \right] \frac{1}{(\hat{p}^2 + m^2)^2}, \tag{B.50}$$

where the term in square brackets is the one-loop self-energy tadpole. It can be shown that its divergence can be canceled by the two-point vertex counterterm.

B.3.3 Vertex function at one loop

The function $V(s)$ is defined by the loop integral

$$V(s) = \frac{1}{2}\int_k \frac{1}{\hat{k}^2 + m_R^2}\frac{1}{\hat{q}^2 + m_R^2}, \tag{B.51}$$

where $q_\mu = p_{1\mu} + p_{2\mu} + k_\mu$. Power counting reveals that the loop integral has a finite continuum limit. Therefore we can take $a \to 0$ so that up to cutoff effects

$$V(s) = \frac{1}{2}\int_k \frac{d^3k}{(2\pi)^3}\frac{1}{k^2 + m_R^2}\frac{1}{q^2 + m_R^2}. \tag{B.52}$$

Feynman parametrisation (A.3) yields

$$V(s) = \frac{1}{2}\int_k \frac{d^3k}{(2\pi)^3}\int_0^1 dx\ \frac{1}{((1-x)(k^2 + m_R^2)^2 + x(q^2 + m_R^2))^2} \tag{B.53}$$

$$= \frac{1}{2}\int_k \frac{d^3l}{(2\pi)^3}\int_0^1 dx\ \frac{1}{(l^2 + m_R^2 + x(1-x)s)^2}, \tag{B.54}$$

where in the second line we reshuffled the denominator and changed the integration variable to $l = k + x(p_1 + p_2)$. Now, using eq. (A.7) we get

$$V(s) = \frac{1}{16\pi}\int_0^1 \frac{dx}{\sqrt{m_R^2 + x(1-x)s}} \tag{B.55}$$

which can be reduced to

$$V(s) = \frac{1}{8\pi}\frac{1}{\sqrt{s}}\operatorname{arccot}\left(\frac{2m_R}{\sqrt{s}}\right). \tag{B.56}$$

Taking the limit $s \to 0$

$$V(0) = \frac{1}{16\pi m_R}, \tag{B.57}$$

where we used $\operatorname{arccot}\frac{1}{x} = \arctan x = x + \mathcal{O}(x^3)$.

Appendix C

Derivation of the lattice translation Ward identity

In this section we derive the lattice TWI in detail stating all the higher order terms omitted in sec. 4.2.2.

C.1 Derivative identities

Complementary to the definition of the forward, backward and symmetric derivative there is the identity

$$\hat{\partial}_\mu - \hat{\partial}^*_\mu = a\hat{\partial}_\mu\hat{\partial}^*_\mu. \tag{C.1}$$

The derivatives verify the following discrete versions of the Leibniz rule,

$$\hat{\partial}_\mu(fg) = (\hat{\partial}_\mu f)g + f(\hat{\partial}_\mu g) + a(\hat{\partial}_\mu f)(\hat{\partial}_\mu g), \tag{C.2}$$
$$\hat{\partial}^*_\mu(fg) = (\hat{\partial}^*_\mu f)g + f(\hat{\partial}^*_\mu g) - a(\hat{\partial}^*_\mu f)(\hat{\partial}^*_\mu g), \tag{C.3}$$
$$\bar{\partial}_\mu(fg) = (\bar{\partial}_\mu f)g + f(\bar{\partial}_\mu g) + \frac{a}{2}[(\hat{\partial}_\mu f)(\hat{\partial}_\mu g) - (\hat{\partial}^*_\mu f)(\hat{\partial}^*_\mu g)]. \tag{C.4}$$

Using eq. (C.1), one can rewrite eq. (C.4),

$$\bar{\partial}_\mu(fg) = (\bar{\partial}_\mu f)g + f(\bar{\partial}_\mu g) + \frac{a^2}{2}[(\hat{\partial}_\mu f)(\hat{\partial}_\mu\hat{\partial}^*_\mu g) + (\hat{\partial}_\mu\hat{\partial}^*_\mu f)(\hat{\partial}^*_\mu g)]. \tag{C.5}$$

This last expression is more useful than the original one because the violation of the Leibniz rule appears explicitly as an $\mathcal{O}(a^2)$ effect. Similarly, one can derive discrete versions of integration by parts,

$$a^d \sum_{x\in\Lambda} (\hat{\partial}_\mu f_x) g_x = -a^d \sum_{x\in\Lambda} f_x (\hat{\partial}^*_\mu g_x) \tag{C.6}$$

$$a^d \sum_{x\in\Lambda} (\bar{\partial}_\mu f_x) g_x = -a^d \sum_{x\in\Lambda} f_x (\bar{\partial}_\mu g_x). \tag{C.7}$$

From an operator point of view, these two equations mean that $-\hat{\partial}^*_\mu$ is the adjoint of $\hat{\partial}_\mu$ and that $\bar{\partial}_\mu$ is anti-hermitian.

C.2 Lattice translation Ward identity

In sec. 4.2.1 we found the most general form of a local Ward identity on the lattice, eq. (4.37),

$$\langle \mathcal{P}\ \hat{\delta}_x S \rangle = \langle \hat{\delta}_x \mathcal{P} \rangle. \tag{C.8}$$

The scalar action on the lattice was defined in eq. (4.2),

$$S(\phi) = a^3 \sum_x \left(\frac{1}{2} \sum_\mu \hat{\partial}_\mu \phi \hat{\partial}_\mu \phi + \frac{1}{2} m^2 \phi^2 + \frac{\lambda}{4!} \phi^4 \right). \tag{C.9}$$

We now compute the local variation of the action in eq. (C.8) relative to the transformation $\exp(\alpha \bar{\partial}_\rho)$, eq. (4.39). The local TWI reads

$$\langle \mathcal{P}\ \hat{\delta}_{x,\rho} S \rangle = \langle \hat{\delta}_{x,\rho} \mathcal{P} \rangle, \tag{C.10}$$

where

$$\hat{\delta}_{x,\rho} F = \frac{\partial F}{\partial \phi}\ \bar{\partial}_\rho \phi(x). \tag{C.11}$$

The local variations of a field and forward derivative are

$$\hat{\delta}_{x,\rho} \phi(y) = \delta_{y,x} \bar{\partial}_{\rho,x} \phi(x) \tag{C.12}$$

$$\hat{\delta}_{x,\rho} \hat{\partial}_\mu \phi(y) = (\hat{\partial}_{\mu,y} \delta_{y,x})(\bar{\partial}_{\rho,x} \phi(x)) \tag{C.13}$$

where the additional indices x, y on the derivatives explicitly state on which variable the derivatives act.

Starting with the kinetic term we find

$$\hat{\delta}_{x,\rho} S_{kin} = a^3 \sum_{y,\mu} (\hat{\partial}_{\mu,y}\phi(y))(\hat{\partial}_{\mu,y}\delta_{y,x})(\bar{\partial}_{\rho,x}\phi(x)) \tag{C.14}$$

$$= -\sum_{\mu} (\hat{\partial}_{\mu,x}\hat{\partial}^*_{\mu,x}\phi(x))(\bar{\partial}_{\rho,x}\phi(x)). \tag{C.15}$$

In order to formulate the EMT, we need to write the local variation of the action as a total derivative. To do so, we know that forward, backward and symmetric derivative are equal up to order a,

$$\hat{\partial}_\mu \phi = \bar{\partial}_\mu \phi + a D_\mu \tag{C.16}$$

$$\hat{\partial}^*_\mu \phi = \bar{\partial}_\mu \phi - a D_\mu, \tag{C.17}$$

where aD_μ is of order a,

$$aD_\mu = \frac{1}{2a}\phi(x + a\hat{\mu}) - \frac{1}{a}\phi(x) + \frac{1}{2a}\phi(x - a\hat{\mu}) \tag{C.18}$$

$$D_\mu = \frac{1}{2}\partial^2_\mu \phi(x) + \mathcal{O}(a). \tag{C.19}$$

Thus, we can rewrite eq. (C.15) using the symmetric derivative,

$$\hat{\delta}_{x,\rho} S_{kin} = -\sum_{\mu} (\bar{\partial}_\mu \bar{\partial}_\mu \phi(x))(\bar{\partial}_\rho \phi(x)) + a^2 D'_\rho, \tag{C.20}$$

where $a^2 D'_\rho$ is of order a^2,

$$\begin{aligned} a^2 D'_\rho = \sum_\mu \Bigg(& \frac{3}{2a^2}\phi(x) - \frac{1}{a^2}\left(\phi(x + a\hat{\mu}) + \phi(x - a\hat{\mu})\right) \\ & + \frac{1}{4a^2}\left(\phi(x + 2a\hat{\mu}) + \phi(x - 2a\hat{\mu})\right)\Bigg)(\bar{\partial}_\rho \phi) \end{aligned} \tag{C.21}$$

$$D'_\rho = \frac{1}{4}(\bar{\partial}_\rho \phi) \sum_\mu \partial^4_\mu \phi(x) + \mathcal{O}(a). \tag{C.22}$$

The Leibniz rule (C.5) gives

$$-\sum_{\mu}(\bar{\partial}_\mu\bar{\partial}_\mu\phi)(\bar{\partial}_\rho\phi) = -\sum_{\mu}\bar{\partial}_\mu\left((\bar{\partial}_\mu\phi)(\bar{\partial}_\rho\phi)\right)+\sum_{\mu}(\bar{\partial}_\mu\phi)(\bar{\partial}_\mu\bar{\partial}_\rho\phi)+a^2K_\rho^{(1)}. \quad \text{(C.23)}$$

Using it again, the second term on the right-hand side is

$$\sum_{\mu}(\bar{\partial}_\mu\phi)(\bar{\partial}_\mu\bar{\partial}_\rho\phi) = \frac{1}{2}\sum_{\mu}\bar{\partial}_\rho(\bar{\partial}_\mu\phi)^2+a^2K_\rho^{(2)}, \quad \text{(C.24)}$$

where $a^2K_\rho^{(1)}$ and $a^2K_\rho^{(2)}$ are of order a^2,

$$K_\rho^{(1)} = \frac{1}{2}\sum_{\mu}\left((\hat{\partial}_\mu\bar{\partial}_\mu\phi)(\hat{\partial}_\mu\hat{\partial}_\mu^*\bar{\partial}_\rho\phi)+(\hat{\partial}_\mu\hat{\partial}_\mu^*\bar{\partial}_\mu\phi)(\hat{\partial}_\mu^*\bar{\partial}_\rho\phi)\right) \quad \text{(C.25)}$$

$$K_\rho^{(2)} = -\frac{1}{2}\sum_{\mu}(\hat{\partial}_\mu\hat{\partial}_\mu^*\bar{\partial}_\mu\phi)(\bar{\partial}_\mu\bar{\partial}_\mu\phi). \quad \text{(C.26)}$$

Defining the kinetic part of the lattice EMT as

$$T_{\mu\rho,kin} = \bar{\partial}_\mu\phi\bar{\partial}_\rho\phi-\frac{1}{2}\delta_{\mu\rho}\sum_{\sigma}(\bar{\partial}_\sigma\phi)^2, \quad \text{(C.27)}$$

the local variation of the kinetic part of the action reads

$$\hat{\delta}_{x,\rho}S_{kin} = -\sum_{\mu}\bar{\partial}_\mu T_{\mu\rho,kin}(x)+a^2D'_\rho(x)+a^2K_\rho^{(1)}(x)+a^2K_\rho^{(2)}(x). \quad \text{(C.28)}$$

We find for the mass term

$$\hat{\delta}_{x,\rho}S_m = m^2\phi(x)\bar{\partial}_{\rho,x}\phi(x) \quad \text{(C.29)}$$

$$= -\sum_{\mu}\bar{\partial}_\mu T_{\mu\rho,m}(x)+a^2M_\rho(x), \quad \text{(C.30)}$$

where we defined the mass term of the EMT,

$$T_{\mu\rho,m} = -\frac{1}{2}m^2\delta_{\mu\rho}\phi^2. \quad \text{(C.31)}$$

a^2M_ρ is of order a^2,

$$M_\rho = -\frac{m^2}{2}(\hat{\partial}_\rho\hat{\partial}_\rho^*\phi)(\bar{\partial}_\rho\phi). \quad \text{(C.32)}$$

We find for the interaction term

$$\hat{\delta}_{x,\rho} S_\lambda = \frac{\lambda}{3!}\phi^3(x)\bar{\partial}_{\rho,x}\phi(x) \tag{C.33}$$

$$= -\sum_\mu \bar{\partial}_\mu T_{\mu\rho,\lambda}(x) + a^2\Lambda_\rho(x), \tag{C.34}$$

where we defined the interaction term of the EMT,

$$T_{\mu\rho,\lambda} = -\frac{\lambda}{4!}\delta_{\mu\rho}\phi^4. \tag{C.35}$$

$a^2\Lambda_\rho$ is of order a^2,

$$\Lambda_\rho = -\frac{\lambda}{4!}\left((\bar{\partial}_\rho\phi)(\hat{\partial}_\rho\hat{\partial}^*_\rho\phi) + (\bar{\partial}_\rho\phi^2)(\hat{\partial}_\rho\hat{\partial}^*_\rho\phi^2)\right). \tag{C.36}$$

So finally, the total TWI reads

$$\sum_\mu \bar{\partial}_\mu\langle T_{\mu\rho}\mathcal{P}\rangle = -\langle\delta_{x,\rho}\mathcal{P}\rangle + a^2\langle X_\rho\mathcal{P}\rangle, \tag{C.37}$$

with

$$T_{\mu\rho} = \bar{\partial}_\mu\phi\bar{\partial}_\rho\phi - \delta_{\mu\rho}\left(\frac{1}{2}\sum_\sigma(\bar{\partial}_\sigma\phi)^2 + \frac{1}{2}m^2\phi^2 + \frac{\lambda}{4!}\phi^4\right), \tag{C.38}$$

$$X_\rho = D'_\rho + K^{(1)}_\rho + K^{(2)}_\rho + M_\rho + \Lambda_\rho. \tag{C.39}$$

Appendix D

Divergent energy-momentum tensor insertions

Inserting the EMT into n-point functions produces only overall divergencies in a few cases, namely for the insertion of the EMT into the diagrams b-d shown in fig. 4.9. In this appendix we derive the explicit expressions of the leading order and first order insertions of the appropriate terms in the EMT. These are the two terms containing derivatives. We define

$$T_{\mu\rho\partial^2} = \bar{\partial}_\mu\phi\bar{\partial}_\rho\phi - \delta_{\mu\rho}\frac{1}{2}\sum_\sigma \bar{\partial}_\sigma\phi\bar{\partial}_\sigma\phi. \tag{D.1}$$

D.1 Divergent insertion of the energy-momentum tensor to leading order

Position space

$$\bar{\partial}_\mu\phi\bar{\partial}_\rho\phi(z) = -\int_{k_1,k_2} e^{i(k_1+k_2)z}\ \bar{k}_{1\mu}\ \bar{k}_{2\rho}\ a^{2d}\sum_{m_1,m_2} e^{-ik_1m_1a}e^{-ik_2m_2a}\phi(m_1)\phi(m_2) \tag{D.2}$$

$$
\begin{aligned}
&\langle\phi(x)\phi(y)T_{\mu\rho\partial^2}(z)\rangle_0 = \\
&= -\frac{1}{a^d}\frac{\delta}{\delta J(x)}\frac{1}{a^d}\frac{\delta}{\delta J(y)}\int_{k_1,k_2} e^{i(k_1+k_2)z}\left(\bar{k}_{1\mu}\bar{k}_{2\rho} - \frac{1}{2}\delta_{\mu\rho}\sum_\sigma \bar{k}_{1\sigma}\bar{k}_{2\sigma}\right)\times \\
&\quad\times a^{2d}\sum_{m_1,m_2} e^{-ik_1m_1a}e^{-ik_2m_2a}\,\frac{1}{a^d}\frac{\delta}{\delta J(am_1)}\frac{1}{a^d}\frac{\delta}{\delta J(am_2)}Z_0(J)\Big|_{J=0}
\end{aligned}
\tag{D.3}
$$

$$
\begin{aligned}
&= -\int_{k_1,k_2} e^{i(k_1+k_2)z}\left(\bar{k}_{1\mu}\bar{k}_{2\rho} - \frac{1}{2}\delta_{\mu\rho}\sum_\sigma \bar{k}_{1\sigma}\bar{k}_{2\sigma}\right)\times \\
&\quad\times a^{2d}\sum_{m_1,m_2} e^{-ik_1m_1a}e^{-ik_2m_2a}\left(D(x-am_1)D(y-am_2) + D(x-am_2)D(y-am_1)\right)
\end{aligned}
\tag{D.4}
$$

Momentum space

$$
\begin{aligned}
&\langle\tilde{\phi}(p_1)\tilde{\phi}(p_2)\tilde{T}_{\mu\rho\partial^2}(p_3)\rangle_0 = \\
&= a^{3d}\sum_{n_1,n_2,n_3} e^{-i\sum_i^3 p_i n_i a}\langle\phi(an_1)\phi(an_2)T_{\mu\rho\partial^2}(an_3)\rangle_0
\end{aligned}
\tag{D.5}
$$

$$
= (2\pi)^d\delta^d(\textstyle\sum_i^3 p_i)\dfrac{1}{\hat{p}_1^2+m^2}\dfrac{1}{\hat{p}_2^2+m^2}\left[-\overline{p}_{1\mu}\overline{p}_{2\rho} - \overline{p}_{2\mu}\overline{p}_{1\rho} + \delta_{\mu\rho}\sum_\sigma \overline{p}_{1\sigma}\overline{p}_{2\sigma}\right] \tag{D.6}
$$

D.2 Divergent insertion of the energy-momentum tensor to order λ_R

Position space

$$
\begin{aligned}
&\langle\phi(x)\phi(y)T_{\mu\rho\partial^2}(z)\rangle_1 = \\
&= -\frac{1}{a^d}\frac{\delta}{\delta J(x)}\frac{1}{a^d}\frac{\delta}{\delta J(y)}\int_{k_1,k_2} e^{i(k_1+k_2)z}\left(\bar{k}_{1\mu}\bar{k}_{2\rho} - \frac{1}{2}\delta_{\mu\rho}\sum_\sigma \bar{k}_{1\sigma}\bar{k}_{2\sigma}\right)\times \\
&\quad\times a^{2d}\sum_{m_1,m_2} e^{-ik_1m_1a}e^{-ik_2m_2a}\,\frac{1}{a^d}\frac{\delta}{\delta J(am_1)}\frac{1}{a^d}\frac{\delta}{\delta J(am_2)}Z_\times(J)\Big|_{J=0}
\end{aligned}
\tag{D.7}
$$

$$\begin{aligned} Z_\times(J) &= -\frac{\lambda}{4!}a^d \sum_n \left(-\frac{1}{a^d}\frac{\delta}{\delta J(an)}\right)^4 Z_0(J) \\ &= -\frac{\lambda}{4!}a^d \sum_n \left(a^d \sum_m D(an-am)J(am)\right)^4 \end{aligned} \tag{D.8}$$

$$\langle\phi(x)\phi(y)T_{\mu\rho\partial^2}(z)\rangle_1 =$$

$$\begin{aligned} &= \lambda \int_{k_1,k_2} e^{i(k_1+k_2)z}\left(\bar{k}_{1\mu}\bar{k}_{2\rho} - \frac{1}{2}\delta_{\mu\rho}\sum_\sigma \bar{k}_{1\sigma}\bar{k}_{2\sigma}\right)\times \\ &\quad \times a^{2d}\sum_{m_1,m_2} e^{-ik_1m_1a}e^{-ik_2m_2a}a^d\sum_n D(an-am_1)D(an-am_2)D(an-x)D(an-y) \end{aligned} \tag{D.9}$$

Momentum space

$$\langle\tilde{\phi}(p_1)\tilde{\phi}(p_2)\tilde{T}_{\mu\rho\partial^2}(p_3)\rangle_1 =$$

$$= a^{3d}\sum_{n_1,n_2,n_3} e^{-i\sum_i^3 p_i n_i a}\langle\phi(an_1)\phi(an_2)T_{\mu\rho\partial^2}(an_3)\rangle_1 \tag{D.10}$$

$$= (2\pi)^d\delta^d(\textstyle\sum_i^3 p_i)\dfrac{1}{\hat{p}_1^2+m^2}\dfrac{1}{\hat{p}_2^2+m^2}(-\lambda)\displaystyle\int_k \frac{\overline{k}_\mu(\overline{k+p_3})_\rho - \frac{1}{2}\delta_{\mu\rho}\sum_\sigma \overline{k}_\sigma(\overline{k+p_3})_\sigma}{(\hat{k}^2+m^2)(\widehat{(k+p_3)}^2+m^2)} \tag{D.11}$$

Appendix E

Estimate of the relative error of the solution of a linear system of equations in connection with the bootstrap method

We want to estimate the error of the solution x of the linear system

$$Ax = b, \tag{E.1}$$

where A is a matrix and x and b are vectors. This task is complicated by the use of the bootstrap method utilised to calculate the error of the solution. According to eqs. (5.27,5.28) the best estimate of one component of the solution vector and its variance are given by

$$\langle x_i \rangle = \frac{1}{s} \sum_{\beta=1}^{s} (x_i)_\beta \tag{E.2}$$

$$\sigma^2_{\langle x_i \rangle} = \langle x_i^2 \rangle - \langle x_i \rangle^2, \tag{E.3}$$

where we expressed the bootstrap averages with brackets instead of bars for better readability. In particular, we are looking for the relation of the relative error in x to the relative errors in A and b, and the condition number. Hence, we are

interested in the relationship between the quantities

$$\frac{\|\sigma_{\langle x\rangle}\|}{\|\langle x\rangle\|}, \quad \frac{\|\sigma_{\langle A\rangle}\|}{\|\langle A\rangle\|}, \quad \frac{\|\sigma_{\langle b\rangle}\|}{\|\langle b\rangle\|}, \quad \kappa(A) = \|A\|\|A^{-1}\|, \tag{E.4}$$

where the norms are chosen to be two-norms. The two-norms of a vector $x \in \mathbb{R}^n$ and a matrix $A \in \mathbb{R}^{m\times n}$ are defined as

$$\|x\|_2 = \left(\sum_{i=1}^{m} |x_i|^2\right)^{1/2} \tag{E.5}$$

$$\|A\|_2 = \sup_{x\neq 0} \frac{\|Ax\|_2}{\|x\|_2}. \tag{E.6}$$

We will work with the square of the two-norm as it is easily connected to the bootstrap variance,

$$\|\sigma_{\langle x\rangle}\|^2 = \textstyle\sum_i \sigma^2_{\langle x_i\rangle}. \tag{E.7}$$

Another useful identity is

$$\|\sigma_{\langle x\rangle}\|^2 = \langle \textstyle\sum_i (x_i - \langle x_i\rangle)^2\rangle \tag{E.8}$$

$$= \langle \|x - \langle x\rangle\|^2\rangle. \tag{E.9}$$

We define the square of the two-norm of the variance of $\langle A\rangle$ in accordance with eq. (E.8) because the variance of the entries in A calculated with the bootstrap method is

$$\sigma^2_{\langle A_{ij}\rangle} = \langle (A_{ij} - \langle A_{ij}\rangle)^2\rangle. \tag{E.10}$$

Hence,

$$\|\sigma_{\langle A\rangle}\|^2 = \langle \textstyle\sum_{ij} (A_{ij} - \langle A_{ij}\rangle)^2\rangle \tag{E.11}$$

$$= \langle \|A - \langle A\rangle\|_{\mathrm{F}}^2\rangle \tag{E.12}$$

$$\geq \langle \|A - \langle A\rangle\|_2^2\rangle. \tag{E.13}$$

In the second line we used the definition of the Frobenius norm,

$$\|A\|_F = \left(\sum_{ij} |A_{ij}|^2\right)^{1/2}, \tag{E.14}$$

and in the third line its relation to the two-norm $\|A\|_F \geq \|A\|_2$.

Starting from eq. (E.8) we can find the upper bound for the squared norm of the variance vector:

$$\|\sigma_{\langle x\rangle}\|^2 = \langle \textstyle\sum_i (A^{-1}_{ij}(b_j - b'_j))^2 \rangle \tag{E.15}$$
$$= \langle \|A^{-1}(b - b')\|^2 \rangle \tag{E.16}$$
$$\leq \langle \|A^{-1}\|^2 \|b - b'\|^2 \rangle \tag{E.17}$$
$$\leq \|A^{-1}\|^2_{max} \langle \|b - b'\|^2 \rangle, \tag{E.18}$$

where in the first line b'_j is defined through eq. (E.8) as

$$b'_j = A_{jk}\langle x_k \rangle. \tag{E.19}$$

In the third line we used $\|Av\| \leq \|A\|\|v\|$, and $\|A^{-1}\|_{max}$ in the last line is the largest norm of all bootstrap samples. The bootstrap average of the squared norm of $b - b'$ can be rewritten as

$$\langle \|b - b'\|^2 \rangle = \langle \|b - \langle b\rangle + \langle b\rangle - b'\|^2 \rangle \tag{E.20}$$
$$\leq \langle \|b - \langle b\rangle\|^2 + \|b' - \langle b\rangle\|^2 + 2\|b - \langle b\rangle\|\|b' - \langle b\rangle\| \rangle. \tag{E.21}$$

The first term in eq. (E.21) is simply

$$\langle \|b - \langle b\rangle\|^2 \rangle = \|\sigma_{\langle b\rangle}\|^2. \tag{E.22}$$

The second term in eq. (E.21) can be bounded,

$$\langle \|b' - \langle b\rangle\|^2 \rangle = \langle \textstyle\sum_i \left(A_{ij}\langle x_j\rangle - \langle A_{ij}x_j\rangle\right)^2 \rangle \tag{E.23}$$
$$= \langle \textstyle\sum_i \left((A_{ij} - \langle A_{ij}\rangle)\langle x_j\rangle\right)^2 \rangle \tag{E.24}$$
$$= \langle \|(A - \langle A\rangle)\langle x\rangle\|^2 \rangle \tag{E.25}$$
$$\leq \langle \|(A - \langle A\rangle)\|^2 \|\langle x\rangle\|^2 \rangle \tag{E.26}$$
$$\leq \|\sigma_{\langle A\rangle}\|^2 \|\langle x\rangle\|^2, \tag{E.27}$$

where we assumed in the second line that A and x are uncorrelated. This assumption is necessary to be able to move on with the analytic calculation. In the last line we used eq. (E.13).

The third term in eq. (E.21) can be bounded as well,

$$\begin{aligned}
\langle \|b - \langle b\rangle\| \|b' - \langle b\rangle\| \rangle &= \langle \|b - \langle b\rangle\| \|(A - \langle A\rangle)\langle x\rangle\| \rangle && \text{(E.28)}\\
&\leq \langle \|b - \langle b\rangle\| \rangle \langle \|A - \langle A\rangle\| \rangle \|\langle x\rangle\| && \text{(E.29)}\\
&\leq \langle \|b - \langle b\rangle\|^2 \rangle^{\frac{1}{2}} \langle \|A - \langle A\rangle\|^2 \rangle^{\frac{1}{2}} \|\langle x\rangle\| && \text{(E.30)}\\
&\leq \|\sigma_{\langle b\rangle}\| \|\sigma_{\langle A\rangle}\| \|\langle x\rangle\|. && \text{(E.31)}
\end{aligned}$$

In the first line we again assumed that A and x are uncorrelated, in addition, in line two we also assumed that the fluctuations about the bootstrap average of A and b are uncorrelated. In the third line we used $\langle v\rangle^2 \leq \langle v^2\rangle$.

Putting it all together and dividing by the squared norm of the bootstrap average of x we arrive at

$$\frac{\|\sigma_{\langle x\rangle}\|^2}{\|\langle x\rangle\|^2} \leq \kappa(A)^2_{max} \left(\frac{\|\sigma_{\langle b\rangle}\|^2}{\|\langle b\rangle\|^2} + \frac{\|\sigma_{\langle A\rangle}\|^2}{\|\langle A\rangle\|^2} + 2\frac{\|\sigma_{\langle b\rangle}\| \|\sigma_{\langle A\rangle}\|}{\|\langle b\rangle\| \|\langle A\rangle\|} \right). \tag{E.32}$$

Here, we used the definition of the condition number, eq. (E.4), and $\|\langle A\rangle\| \leq \|A\|_{max}$. Further, note that $\|\langle b\rangle\| \leq \|\langle A\rangle\| \|\langle x\rangle\|$. To be able to calculate the right-hand side explicitly the two-norm of the matrix can be estimated by

$$\|\langle A\rangle\| \geq \frac{1}{\sqrt{n}} \|\langle A\rangle\|_\infty, \tag{E.33}$$

where the infinity-norm is defined as the maximum row sum,

$$\|\langle A\rangle\|_\infty = \max_{1\leq i\leq m} \sum_{j=1}^{n} |\langle A_{ij}\rangle|. \tag{E.34}$$

Finally, the desired expression is

$$\frac{\|\sigma_{\langle x\rangle}\|^2}{\|\langle x\rangle\|^2} \leq \kappa(A)^2_{max} \left(\frac{\|\sigma_{\langle b\rangle}\|^2}{\|\langle b\rangle\|^2} + n\frac{\|\sigma_{\langle A\rangle}\|^2}{\|\langle A\rangle\|^2_\infty} + 2\sqrt{n}\frac{\|\sigma_{\langle b\rangle}\| \|\sigma_{\langle A\rangle}\|}{\|\langle b\rangle\| \|\langle A\rangle\|_\infty} \right). \tag{E.35}$$

All definitions, identities and inequalities in this chapter can be found in [55].

Bibliography

[1] F. Capponi, A. Rago, L. Del Debbio, S. Ehret, and R. Pellegrini. Renormalisation of the energy-momentum tensor in scalar field theory using the Wilson flow. *PoS*, LATTICE2015:306, 2016.

[2] F. Capponi, L. Del Debbio, S. Ehret, R. Pellegrini, A. Portelli, and A. Rago. Renormalisation of the scalar energy-momentum tensor with the Wilson flow. *PoS*, LATTICE2016:341, 2016.

[3] M. E. Peskin and D. V. Schroeder. *An Introduction To Quantum Field Theory (Frontiers in Physics)*. Westview Press, 1995.

[4] M. Srednicki. *Quantum Field Theory*. Cambridge University Press, 2007.

[5] T. Muta. *Foundations of Quantum Chromodynamics: An Introduction to Perturbative Methods in Gauge Theories*. World Scientific Lecture Notes in Physics. World Scientific, 1987.

[6] D. J. Gross and F. Wilczek. Ultraviolet behavior of non-abelian gauge theories. *Phys. Rev. Lett.*, 30:1343–1346, 1973.

[7] H. D. Politzer. Reliable perturbative results for strong interactions? *Phys. Rev. Lett.*, 30:1346–1349, 1973.

[8] D. J. Gross and F. Wilczek. Asymptotically free gauge theories. i. *Phys. Rev. D*, 8:3633–3652, 1973.

[9] K. G. Wilson. Confinement of quarks. *Phys. Rev. D*, 10:2445–2459, 1974.

[10] C. Gattringer and C. B. Lang. *Quantum Chromodynamics on the Lattice: An Introductory Presentation*. Lecture Notes in Physics. Springer, 2009.

[11] H. J. Rothe. *Lattice Gauge Theories: An Introduction*, volume 74 of *World Scientific Lecture Notes in Physics*. World Scientific Publishing Company, Incorporated, 3rd edition, 2005.

[12] J. Beringer et. al. Review of particle physics. *Phys. Rev. D*, 86:010001, 2012.

[13] M. Luscher. Trivializing maps, the Wilson flow and the HMC algorithm. *Commun. Math. Phys.*, 293:899–919, 2010.

[14] M. Luscher. Properties and uses of the Wilson flow in lattice QCD. *JHEP*, 08:071, 2010. [Erratum: JHEP03,092(2014)].

[15] M. Luscher and P. Weisz. Perturbative analysis of the gradient flow in non-abelian gauge theories. *JHEP*, 02:051, 2011.

[16] M. Luscher. Chiral symmetry and the Yang-Mills gradient flow. *JHEP*, 04:123, 2013.

[17] M. Luscher. Step scaling and the Yang-Mills gradient flow. *JHEP*, 06:105, 2014.

[18] S. Coleman and R. Jackiw. Why dilatation generators do not generate dilatations. *Annals Phys.*, 67:552–598, 1971.

[19] C. G. Callan Jr., S. Coleman, and R. Jackiw. A new improved energy-momentum tensor. *Annals of Physics*, 59(1):42 – 73, 1970.

[20] S. Caracciolo, G. Curci, P. Menotti, and A. Pelissetto. The Energy-Momentum Tensor on the Lattice: The Scalar Case. *Nucl. Phys.*, B309:612–624, 1988.

[21] S. Caracciolo, G. Curci, P. Menotti, and A. Pelissetto. The Energy-Momentum Tensor for Lattice Gauge Theories. *Annals Phys.*, 197:119, 1990.

[22] F. Capponi, L. Del Debbio, A. Patella, and A. Rago. Renormalization constants of the lattice energy-momentum tensor using the gradient flow. *PoS*, LATTICE2015:302, 2016.

[23] L. Del Debbio, B. Lucini, A. Patella, C. Pica, and A. Rago. Conformal versus confining scenario in SU(2) with adjoint fermions. *Phys. Rev.*, D80:074507, 2009.

[24] H. Suzuki. Energy-momentum tensor from the Yang-Mills gradient flow. *PTEP*, 2013:083B03, 2013. [Erratum: PTEP2015,079201(2015)].

[25] H. Makino and H. Suzuki. Lattice energy-momentum tensor from the Yang-Mills gradient flow – inclusion of fermion fields. *PTEP*, 2014:063B02, 2014. [Erratum: PTEP2015,079202(2015)].

[26] H. Makino and H. Suzuki. Lattice energy-momentum tensor from the Yang-Mills gradient flow – a simpler prescription. 2014.

[27] L. Giusti and M. Pepe. Energy-momentum tensor on the lattice: Non-perturbative renormalization in Yang-Mills theory. *Phys. Rev.*, D91:114504, 2015.

[28] L. Del Debbio, A. Patella, and A. Rago. Space-time symmetries and the Yang-Mills gradient flow. *JHEP*, 11:212, 2013.

[29] K. G. Wilson and John B. Kogut. The Renormalization group and the epsilon expansion. *Phys. Rept.*, 12:75–200, 1974.

[30] K. G. Wilson and M. E. Fisher. Critical exponents in 3.99 dimensions. *Phys. Rev. Lett.*, 28:240–243, 1972.

[31] A. Patella, L. Del Debbio, B. Lucini, C. Pica, and A. Rago. Confining vs. conformal scenario for SU(2) with adjoint fermions. Gluonic observables. *PoS*, LATTICE2010:068, 2010.

[32] C. Monahan and K. Orginos. Locally smeared operator product expansions in scalar field theory. *Phys. Rev.*, D91(7):074513, 2015.

[33] M. Bochicchio, L. Maiani, G. Martinelli, G. C. Rossi, and M. Testa. Chiral Symmetry on the Lattice with Wilson Fermions. *Nucl. Phys.*, B262:331, 1985.

[34] R. C. Brower and P. Tamayo. Embedded Dynamics for ϕ^4 Theory. *Phys. Rev. Lett.*, 62:1087–1090, 1989.

[35] U. Wolff. Monte Carlo errors with less errors. *Comput. Phys. Commun.*, 156:143–153, 2004. [Erratum: Comput. Phys. Commun.176,383(2007)].

[36] U. Wolff. Critical slowing down. *Nucl. Phys. Proc. Suppl.*, 17:93–102, 1990.

[37] N. Metropolis, A. W. Rosenbluth, M. N. Rosenbluth, A. H. Teller, and E. Teller. Equation of state calculations by fast computing machines. *J. Chem. Phys.*, 21:1087–1092, 1953.

[38] M. Luscher. A Portable high quality random number generator for lattice field theory simulations. *Comput. Phys. Commun.*, 79:100–110, 1994.

[39] R. H. Swendsen and J. Wang. Nonuniversal critical dynamics in Monte Carlo simulations. *Phys. Rev. Lett.*, 58:86–88, 1987.

[40] P. W. Kasteleyn and C. M. Fortuin. Phase transitions in lattice systems with random local properties. *J. Phys. Soc. Japan (Suppl.)*, 26:11, 1969.

[41] C. M. Fortuin and P. W. Kasteleyn. On the Random cluster model. 1. Introduction and relation to other models. *Physica*, 57:536–564, 1972.

[42] Ulli Wolff. Collective Monte Carlo Updating for Spin Systems. *Phys. Rev. Lett.*, 62:361, 1989.

[43] A. M. Ferrenberg and R. H. Swendsen. Optimized Monte Carlo analysis. *Phys. Rev. Lett.*, 63:1195–1198, 1989.

[44] M. E. J. Newman and G. T. Barkema. *Monte Carlo Methods in Statistical Physics*. Clarendon Press, Oxford, UK, 1999.

[45] B. Efron. Bootstrap methods: Another look at the jackknife. *Ann. Statist.*, 7(1):1–26, 1979.

[46] B. Efron. Computers and the theory of statistics: Thinking the unthinkable. *SIAM Review*, 21(4):460–480, 1979.

[47] C. Gattringer and C. B. Lang. Quantum chromodynamics on the lattice. *Lect. Notes Phys.*, 788:1–343, 2010.

[48] D. P. Landau and K. Binder. *A Guide to Monte Carlo Simulations in Statistical Physics*. Cambridge University Press, Cambridge, UK, 3rd edition, 2009.

[49] M. N. Barber. *Phase Transitions and Critical Phenomena*, volume 8, chapter Finite-size Scaling. Academic Press, London, UK, 1983.

[50] M. Hasenbusch, K. Pinn, and S. Vinti. Critical exponents of the three-dimensional Ising universality class from finite-size scaling with standard and improved actions. *Phys. Rev.*, B59:11471–11483, 1999.

[51] T. Williams, C. Kelley, and many others. Gnuplot version 5.0. `http://www.gnuplot.info/`, 2015.

[52] D. W. Marquardt. An algorithm for least-squares estimation of nonlinear parameters. *SIAM Journal on Applied Mathematics*, 11(2):431–441, 1963.

[53] K. Levenberg. A method for the solution of certain non-linear problems in least squares. *Quart. Appl. Math.*, 2:164–168, 1944.

[54] C. Patrignani et al. Review of Particle Physics. *Chin. Phys.*, C40(10):100001, 2016.

[55] L. N. Trefethen and III D. Bau. *Numerical linear algebra*. SIAM, Philadelphia, PA, USA, 1997.

[56] M. L. Overton. *Numerical Computing with IEEE Floating Point Arithmetic*. SIAM, Philadelphia, PA, USA, 2001.